

University of Windsor

Scholarship at UWindor

Electronic Theses and Dissertations

Theses, Dissertations, and Major Papers

1-1-2007

Bio-mechanically driven MEMS power generator for implantable medical devices.

Jose Martinez-Quijada
University of Windsor

Follow this and additional works at: <https://scholar.uwindsor.ca/etd>

Recommended Citation

Martinez-Quijada, Jose, "Bio-mechanically driven MEMS power generator for implantable medical devices." (2007). *Electronic Theses and Dissertations*. 7112.
<https://scholar.uwindsor.ca/etd/7112>

This online database contains the full-text of PhD dissertations and Masters' theses of University of Windsor students from 1954 forward. These documents are made available for personal study and research purposes only, in accordance with the Canadian Copyright Act and the Creative Commons license—CC BY-NC-ND (Attribution, Non-Commercial, No Derivative Works). Under this license, works must always be attributed to the copyright holder (original author), cannot be used for any commercial purposes, and may not be altered. Any other use would require the permission of the copyright holder. Students may inquire about withdrawing their dissertation and/or thesis from this database. For additional inquiries, please contact the repository administrator via email (scholarship@uwindsor.ca) or by telephone at 519-253-3000ext. 3208.

**BIO-MECHANICALLY DRIVEN MEMS POWER GENERATOR
FOR IMPLANTABLE MEDICAL DEVICES**

by

Jose Martinez-Quijada

A Thesis

Submitted to the Faculty of Graduate Studies
through the Department of Electrical and Computer Engineering
in Partial Fulfillment of the Requirements for
the Degree of Master of Applied Science at the
University of Windsor

Windsor, Ontario, Canada

2007

© 2007 Jose Martinez-Quijada



Library and
Archives Canada

Published Heritage
Branch

395 Wellington Street
Ottawa ON K1A 0N4
Canada

Bibliothèque et
Archives Canada

Direction du
Patrimoine de l'édition

395, rue Wellington
Ottawa ON K1A 0N4
Canada

Your file *Votre référence*
ISBN: 978-0-494-42279-3
Our file *Notre référence*
ISBN: 978-0-494-42279-3

NOTICE:

The author has granted a non-exclusive license allowing Library and Archives Canada to reproduce, publish, archive, preserve, conserve, communicate to the public by telecommunication or on the Internet, loan, distribute and sell theses worldwide, for commercial or non-commercial purposes, in microform, paper, electronic and/or any other formats.

The author retains copyright ownership and moral rights in this thesis. Neither the thesis nor substantial extracts from it may be printed or otherwise reproduced without the author's permission.

AVIS:

L'auteur a accordé une licence non exclusive permettant à la Bibliothèque et Archives Canada de reproduire, publier, archiver, sauvegarder, conserver, transmettre au public par télécommunication ou par l'Internet, prêter, distribuer et vendre des thèses partout dans le monde, à des fins commerciales ou autres, sur support microforme, papier, électronique et/ou autres formats.

L'auteur conserve la propriété du droit d'auteur et des droits moraux qui protègent cette thèse. Ni la thèse ni des extraits substantiels de celle-ci ne doivent être imprimés ou autrement reproduits sans son autorisation.

In compliance with the Canadian Privacy Act some supporting forms may have been removed from this thesis.

While these forms may be included in the document page count, their removal does not represent any loss of content from the thesis.

Conformément à la loi canadienne sur la protection de la vie privée, quelques formulaires secondaires ont été enlevés de cette thèse.

Bien que ces formulaires aient inclus dans la pagination, il n'y aura aucun contenu manquant.


Canada

Abstract

The design, fabrication, and mounting scheme of a novel bio-mechanically driven MEMS power generator for implantable medical devices is presented and optimized for use in cardiac pacemakers. In the system, an asymmetrical planar rotor embedded with microfabricated NdFeB alternate-polarity permanent magnets oscillates around a central shaft due to the thorax motion during breathing to induce a voltage in two microfabricated planar copper coils embedded in two stators. The microgenerator does not need any external supply of fluid, as necessary in some other types of microgenerators. Two different rotor geometries: a semicircular one and a circular one with a destabilizer have been investigated. With a $1 \times 1 \text{ mm}^2$ rotor footprint area the semicircular rotor microgenerator is capable of generating $397 \text{ }\mu\text{W}$ RMS power with 1.0 V open circuit RMS voltage per stator. The circular rotor microgenerator has a rotor footprint area of $3 \times 3 \text{ mm}^2$ and can generate 59.73 mW RMS power with 9.0 V open circuit RMS voltage per stator. The generated voltage and power are sufficient to meet the power requirements of a typical cardiac pacemaker. Scaled or stacked versions of the microgenerator can be used to satisfy power requirements of other medical devices exploiting other biomechanical actuation sources, e.g. head turning. The generator occupies a much smaller volume compared to existing cardiac pacemaker batteries and offers substantially longer life. This can aid in developing smaller pacemakers and in minimizing the frequency and associated risk and cost of invasive surgeries necessary for replacement of the implant once its battery has been exhausted.

Acknowledgements

I want to take this opportunity to acknowledge the people without whom this work would not have been possible. Firstly, I want to express my sincere gratitude to my thesis supervisor, Dr. Sazzadur Chowdhury, for giving me the opportunity to work in the MEMS field, for his expert guidance and financial support, as well as for accepting my topic of thesis, which became my greatest motivation from the moment I proposed him the core idea in a piece of paper to the completion of this thesis.

I want to deeply thank my beloved wife, Verónica Elizabeth Camacho Zúñiga for her immense love and patience in this great journey and for continuously encouraging me with an ample smile. She has been for me a model of braveness and strength everyday and especially when she brought our little son, Pepito, to life on May 15th, 2006. Now at the age of 18 months, he is an energetic baby that fills up of happiness our lives. Pepito and Eli did not know, when peacefully sleeping at night, that they were inspiring a research work that sooner or later will help improve the quality life of the human being.

Traducción (Translation) – Quiero agradecer profundamente a mi amada esposa, Verónica Elizabeth Camacho Zúñiga, su inmenso amor y paciencia en esta gran aventura y por impulsarme continuamente con una amplia sonrisa. Ella ha sido para mí un modelo de valentía y fortaleza cada día y especialmente cuando trajo a nuestro pequeño hijo, Pepito, a la vida el 15 de Mayo de 2006. Ahora a sus 18 meses de edad, él es un bebé lleno de energía, que colma de felicidad nuestras vidas. Pepito y Eli no sabían, mientras dormían tranquilamente en la noche, que inspiraban un trabajo de investigación que tarde o temprano ayudará a mejorar la calidad de vida del ser humano.

The greatest acknowledgement to my Mom, María del Carmen Quijada Cisneros, and to my Dad, José Martínez Pichardo, whose love has accompanied us in our way from Mexico, from where their efforts brought to reality our dream of living and studying in Canada, giving us the unconditional and generous support that allowed us to live without lacking anything, even with the privilege of knowing the world, and thanks to whom I have a past of delightful memories and a future ahead.

Traducción (Translation) – El mas grande reconocimiento a mi Mamá, María del Carmen Quijada Cisneros, y a mi Papá, José Martínez Pichardo, cuyo amor nos ha acompañado en nuestro camino desde México, desde donde sus esfuerzos hicieron realidad nuestro sueño de vivir y estudiar en Canadá, dándonos el incondicional y generoso apoyo que nos permitió vivir sin que nos faltara nada, aún con el privilegio de conocer el mundo, y gracias a quienes tengo un pasado de recuerdos gratos un futuro por adelante.

My special gratefulness to my friend and godmother of my son, Dr. Irma Araceli Flores Tapia, whose dedicated work kept my eyes open to the books, the snow and the sky. But also for her attention and curiosity to my ideas and for joining me in the fight to improve life conditions of the human being.

Traducción (Translation) – Mi especial gratitud a mi amiga y madrina de mi hijo, la Dra. Irma Araceli Flores Tapia, cuyo dedicado trabajo mantuvo mis ojos abiertos a los libros, a la nieve y al cielo. Pero también por haber puesto su atención y curiosidad en mis ideas y haberse unido a mi en la lucha por mejorar las condiciones de vida del ser humano.

And many thanks to Eli's family and the rest of my family, as well as to our friends, who shape the warm environment I have lived and worked in, who from distance pray for us, and whom I keep incessantly in my heart.

*“Imagina que ya estás ahí,
imagina que ya lo lograste,
imagina que ya lo tienes !
y dale gracias a Dios”*

(Translation)

*“Imagine that you are already there,
imagine that you already achieved it,
imagine that you already have it !
and thank God”*

–María del Carmen Quijada Cisncros

*“El reto del hombre no es vencer al adversario,
sino a la adversidad”*

(Translation)

*“The challenge of the mankind is not to defeat the adversary,
but the adversity”*

–José Martínez Pichardo

Table of Contents

Abstract	iii
Acknowledgements	iv
List of Tables	vii
List of Figures	viii
CHAPTER 1: Introduction	10
1.1 Problem Identification.....	10
1.2 Goals.....	11
1.3 Background.....	13
1.3.1 Energy Storage Alternatives for Biomedical Implants.....	13
1.3.2 State of the Art in Microscale Power Generation	14
1.3.3 Electromagnetic Induction Micropower Generators.....	16
1.3.4 In-body Micropower Generation.....	18
1.4 Principal Results.....	21
1.5 Organization of Thesis.....	22
CHAPTER 2: Device Concept.....	24
2.1 Fundamental Structure and Components.....	24
2.2 Operating Principle	26
2.3 Key Features	27
2.4 Target Application Areas	29
CHAPTER 3: Microgenerator Design.....	31
3.1 Function of a Pacemaker	31
3.2 Design Requirements	33
3.3 Mathematical Model of Axial Flux Brushless Power Generators.....	35
3.4 Rotor Geometry	36
3.5 Magnetic Material Selection.....	38
3.6 Magnetization of NdFeB Magnets.....	39
3.7 Lubrication System.....	43
3.8 Design Strategy and Final Device Specifications	47
CHAPTER 4: Microgenerator Fabrication.....	53
4.1 Fabrication Strategy	53
4.2 Rotor Fabrication	54
4.3 Stator Fabrication.....	63
4.4 Assembly / Encapsulation of the Microgenerator.....	71
CHAPTER 5: Microgenerator Mounting and Actuation System	74
5.1 Silicone Encapsulation Package	75
5.2 Driving Pressure	78
5.3 Mechanical Input to the Microgenerator.....	80
CONCLUSIONS	82
REFERENCES	87
VITA AUCTORIS	96

List of Tables

Table 1. Typical Cardiac Pacemaker Power Supply Specifications.	34
Table 2. Wear and Friction Coefficient of different Ni-P thin films [48].	46
Table 3. Final Design Specifications of the Microgenerator.	50

List of Figures

Figure 1. Three types of electromagnetic induction microgenerators [17].	17
Figure 2. A conceptual 3D model of the microgenerator.	25
Figure 3. Close-up view of the 3D model of the microgenerator.	25
Figure 4. Operating principle of the microgenerator.	26
Figure 5. Stacks and arrays of microgenerators for increased power generation.	28
Figure 6. Multiple-axes mounting system of the microgenerator.	28
Figure 7. Excitation and conduction system and major muscles in the human heart [1].	32
Figure 8. Typical electrocardiogram (ECG) and its characteristic waves [1].	33
Figure 9. Block diagram of a typical cardiac pacemaker.	34
Figure 10. Thickness parameters used to determine the shape factor β .	35
Figure 11. Semicircular rotor geometry.	37
Figure 12. Circular rotor geometry.	37
Figure 13. Capacitor discharge magnetization circuit used to implement MFSSM.	39
Figure 14. Stages of the MFSSM magnetization method.	40
Figure 15. 3D Model used for simulation of the MFSSM magnetization method.	41
Figure 16. Simulation results of magnetic flux density in the MFSSM method.	42
Figure 17. Magnetic flux density along a line crossing through the pole pieces.	42
Figure 18. Detail of the interface between a semicircular rotor and the shaft.	43
Figure 19. Detail of the interface between a circular rotor and the shaft.	44
Figure 20. Conceptual 3D Model of the Ni-P-(IF-WS ₂) solid lubricant film.	46
Figure 21. Maximum output voltage as a function of number of embedded pole pairs.	48
Figure 22. Output voltage waveform of a microgenerator with semicircular rotor.	49
Figure 23. Output voltage waveform of a microgenerator with circular rotor.	49
Figure 24. Cross-sectional view of the final microgenerator with a semicircular rotor.	51
Figure 25. Cross-sectional view of the final microgenerator with a circular rotor.	51
Figure 26. Key of materials used in the fabrication process.	54
Figure 27. Rotor fabrication step 1 – thermal growth of bottom SiO ₂ seed layer.	54
Figure 28. Rotor fabrication step 2 – growth of first epitaxial structural layer.	55
Figure 29. Rotor fabrication step 3 – patterning of openings for NdFeB pole pieces.	55
Figure 30. Rotor fabrication step 4 – deposition of NdFeB thick film using PLD.	56
Figure 31. Rotor fabrication step 5 – removal of excess NdFeB by polishing.	56
Figure 32. Rotor fabrication step 6 – deposition of SiO ₂ seed layer on top of the wafer.	57
Figure 33. Rotor fabrication step 7 – growth of second epitaxial structural layer.	57
Figure 34. Rotor fabrication step 8 – patterning of the rotor-stator gap.	58
Figure 35. Rotor fabrication step 9 – patterning of destabilizer shape and shaft holes.	58
Figure 36. Rotor fabrication step 10 – electroplating of gold for the destabilizer.	59
Figure 37. Rotor fabrication step 11 – electroless deposition of solid lubricant film.	59
Figure 38. Rotor fabrication step 12 – patterning of solid lubricant film in shaft holes.	60
Figure 39. Rotor fabrication step 13 – deposition of bottom sacrificial SU-8 layer.	60
Figure 40. Rotor fabrication step 14 – patterning of the rotor geometry.	61
Figure 41. Rotor fabrication step 15 – deposition of top sacrificial SU-8 layer.	61
Figure 42. Rotor fabrication step 16 – partial release of the rotor.	62
Figure 43. IntelliSuite™ simulation result of rotor process sequence (cross section).	62

Figure 44. IntelliSuite™ simulation result of rotor process sequence (full view).....	62
Figure 45. Stator fabrication step 1 – thermal growth of top SiO ₂ insulating layer.....	63
Figure 46. Stator fabrication step 2 – electroplating of Permalloy® layer.....	63
Figure 47. Stator fabrication step 3 – patterning of the back-iron piece.	64
Figure 48. Stator fabrication step 4 – growth of first epipoly structural layer.	64
Figure 49. Stator fabrication step 5 – patterning of planar coil tracks and terminals.	65
Figure 50. Stator fabrication step 6 – electroplating of back-copper layer.	65
Figure 51. Stator fabrication step 7 – patterning of vias to the planar coil terminals.	66
Figure 52. Stator fabrication step 8 – copper electroplating of planar coil and vias.....	66
Figure 53. Stator fabrication step 9 – polishing of excess copper.	67
Figure 54. Stator fabrication step 10 – growth of second epipoly structural layer.	67
Figure 55. Stator fabrication step 11 – patterning of the shaft.	68
Figure 56. Stator fabrication step 12 – electroless deposition of the solid lubricant film.	68
Figure 57. Stator fabrication step 13 – patterning of solid lubricant film around shaft. ...	69
Figure 58. Stator fabrication step 14 – patterning of rotor-release trenches.	69
Figure 59. IntelliSuite™ simulation result of stator process sequence (cross section 1) ..	70
Figure 60. IntelliSuite™ simulation result of stator process sequence (cross section 2) ..	70
Figure 61. IntelliSuite™ simulation result of stator process sequence (full view).....	71
Figure 62. Assembly & Encapsulation step 1 – alignment of rotor and stators.	71
Figure 63. Assembly & Encapsulation step 2 – Assembly and bonding	72
Figure 64. Assembly & Encapsulation step 3 – Solder pads patterning and rotor release..	72
Figure 65. Assembly & encapsulation step 4 – vacuum sealing.....	73
Figure 66. The microgenerator and actuation mechanism in a silicone rubber capsule. ...	75
Figure 67. Silicone encapsulation of the complete pacemaker system.	76
Figure 68. Attachment of the microgenerator to lateral hinges and driving rods.....	76
Figure 69. Operation of the breathing actuation mechanism.....	77
Figure 70. The human ventilatory system as shown in [55].....	79
Figure 71. Waveforms of the mechanical input to the microgenerator.....	80
Figure 72. The MEMS power generator as a power supply of a blood pressure sensor...83	
Figure 73. The MEMS power generator as a power supply of a drug delivery system....84	
Figure 74. The MEMS power generator as a power supply of a pressure controller.....85	
Figure 75. The MEMS power generator as a power supply of a hearing aid instrument..86	

CHAPTER 1

Introduction

“The finite supply of energy is the primary drawback to battery power. Moreover, there are many situations where replacement or recharging of batteries is inconvenient or impossible. Examples include devices implanted in the human body, e.g. pacemakers and cochlear implants, and devices intended for long duration.”

–David P. Arnold [17]

1.1 Problem Identification

Historically the service life of fully implantable autonomous therapeutic devices has been restricted to the energy content of their batteries, which have to be recharged periodically by means of an external electromagnetic induction device or have to be replaced through a surgical procedure [1]. The effective life of the lithium iodine batteries used in modern cardiac pacemakers has been estimated to be 5 to 7 years after implantation [2]. This effective life span is substantially shorter than the calculated 8 to 11 years lifetime [3–4] of typical pacemakers due to several factors, e.g. lifestyle, medical conditions, type of pacemaker, device settings like pacing rate, pulse amplitude/duration, and the self-discharge phenomenon present in all electrochemical cell batteries. Inevitably, after the battery has been exhausted, a new surgery must be carried out to replace the implant. Highly sophisticated microelectronic modules, such as a Demand Pulse Generator (DPG)

and a sensor subsystem are used in advanced pacemakers to monitor the operating conditions of the pacemaker and physical activity of the recipient and then change the shape and frequency of the output pulses accordingly, aiming to increase the therapeutic performance of the pacemaker and make more efficient utilization of the energy in the battery to extend its lifetime. Although the electronic modules of the pacemaker have been successfully miniaturized, the volume of a typical pacemaker battery ranges from 5 to 8 cm³, which is nearly half the volume of the entire pacemaker system [4]. The weight of pacemaker batteries ranges from 12.5 to 15.5 grams and their dimensions average 49 mm x 46 mm x 6 mm [4]. For a device that is to be implanted, a minimum size and weight are desirable in order to prevent excessive strain, irritation and swelling of surrounding tissues, conditions that, if not controlled properly, could lead to rejection of the implant. The risk, cost and mental and physical pain associated with recurring surgeries, the use of toxic substances in batteries, along with the need for less invasive smaller size longer life implantable medical devices, make it necessary to seek for alternative energy sources for cardiac pacemakers.

1.2 Goals

The human body can be conceived as a continuous source of energy that exists in the form of a complex combination of quasi-periodic mechanical vibrations and random movements due to voluntary and involuntary contraction of the muscles in outer body parts and internal organs. A few examples of this physiological mechanical activity are the overall skeletal muscle contractions, walking activity, wrist/forearm rotation, head turning, chewing/talking, eye turning, eyelids flickering, facial expression, the heartbeat, expansion-contraction of lungs and diaphragm, stomach motion, esophagus and intestine contractive waves, and the activity of several internal muscles in permanent motion, even during sleep. Exploiting the capabilities of today's MEMS and microfabrication technologies, a generator that utilizes the kinetic energy supplied by the body organs can be built to produce sufficient electrical power to drive a variety of electronic medical implants, like a cardiac pacemaker. Said generator can replace existing batteries used in biomedical implants and provide a maintenance-free, non-toxic, long lasting energy

source of higher power per unit volume at a lower cost, and substantially reduce the recurrence of implant replacement surgeries due to battery exhaust.

Motivated by this philosophical thinking, the main goal of this research work is to develop a micro-sized power generator capable of delivering continuous energy to implantable medical devices, cardiac pacemakers in particular, in order to overcome the problem of limited energy content of conventional batteries. The approach undertaken to achieve this goal is to actively convert the kinetic energy present in the human body in the form of physiological motion of the body organs, into electricity through the use of an electromagnetic induction micropower generator built with the MEMS technology.

The work of development in this thesis was fractioned into the following specific goals:

1. Definition of the fundamental structure and components of a microgenerator capable to generate electrical power from the movements present in the human body, clearly defining its operating principle and identifying key features over other types of microgenerators that could potentially make it more suitable for biomedical implant applications.
2. Identification of the possible application areas of the microgenerator and selection of a top-priority target device. Then Investigation of the power requirements of the selected target device.
3. Design of the microgenerator to meet the power requirements of the target device, by firstly identifying an analytical model that allows predicting the behavior of the microgenerator and optimizing the design parameters to achieve maximum performance within the microscale dimensions expected for the device and the constraints imposed by the available materials and fabrication technologies.
4. Identification of the possible variations in the geometry of the microgenerator or its parts as well as the materials and methods that can lead to overcome the main design challenges and to meet the power requirements of the target device.
5. Verification of the design by means of computer simulation. Then the establishment of the final design specifications that will guide the fabrication process.

6. On the base of the final design specifications, the elaboration of an industry standard fabrication process table for the physical construction of the device. Then verification of the process by means of computer simulation.
7. Definition of a mounting and actuation scheme, as well as a suitable packaging, that enable the integration of the device with the circuitry and functional modules of the target device into the target environment.

1.3 Background

1.3.1 Energy Storage Alternatives for Biomedical Implants

Two most prominent energy storage alternatives for biomedical implants are rechargeable batteries with extended number of charge-discharge cycles and miniature nuclear batteries [5–7]. Energy in rechargeable batteries is restored by means of an onboard antenna-rectifier-filter system that collects energy from the electromagnetic field of a nearby antenna placed outside the human body [4–5]. A recipient of an implant that uses such a power supply system will have to permanently carry a battery charger and be aware of the charge level of the battery, that sooner or later will have to be replaced via surgical procedure, since the battery has a finite ability to be recharged. In [6], a microfabricated solid state rechargeable battery has been reported that uses an amorphous vanadium pentoxide (aV_2O_5) cathode, an amorphous lithium phosphorus oxynitride (called *Lipon*) electrolyte, and a lithium anode. Though the fabrication of the battery is simple, the battery exhibits a low current density ($<100 \mu A/cm^2$) that is not sufficient to drive devices such as a cardiac pacemaker. Long-life nuclear batteries employ the emissions of charged particles from the natural decay process of a radioactive isotope to generate electricity by a variety of mechanisms, like thermal conversion, direct charging, optoelectric conversion, etc. In [7], a MEMS based nuclear battery has been reported. The peak output power of this device (with a 64 microcurie source ^{63}Ni in liquid form) is in the order of 0.069 nW, which corresponds to a device efficiency of approximately 1.0%, which falls very short of what is necessary for the operation of most implantable devices. However, further research is going on to improve the power rating of the device. Additionally, both the rechargeable and the nuclear batteries contain hazardous,

expensive or difficult-to-obtain materials. Other linked setbacks, like the risks of corrosion, leakage, production of hydrogen as a by-product or radioactive contamination have prevented these batteries from being widely used to power implantable medical devices, especially cardiac pacemakers.

1.3.2 State of the Art in Microscale Power Generation

The MEMS technology offers the advantage of realizing micro-sized devices such as sensors, actuators, resonators, microfluidic and micro-optic devices that can be batch fabricated. In recent years some design examples [8–11] have been published where miniature or micro-sized electromagnetic induction power generators have been created, some in MEMS technology, to enable microscale power generation. In [8], an internal-combustion tubular micro-engine has been presented where a piston reciprocates between two opposite combustion chambers due to the pressure generated by the expansion of gas produced by the ignition of a fuel-oxidant-catalyst mixture. The piston, containing a permanent magnet, induces a voltage across a coil that is wound around the tubular engine. With a stroke of 60 to 70 mm and 8 mm in diameter, the device is capable to generate 20 W RMS power. An axial flux permanent magnet (AFPM) brushless microgenerator has been reported in [9] where an external gas flow spins a microturbine, which in turn causes a permanent magnet embedded SU-8 polymer rotor to rotate between two silicon stators embedded with electroplated planar copper coils. To reduce friction, the generator employs 1 x 1 x 3 mm conventional ball bearings. With a diameter of 7.5 mm, the device is capable of producing 1.1 mW RMS power at 1.19 V_{pp} per stator when the rotor is driven at a rotational speed of 30,000 RPM.

A variant of the AFPM based power generation in microscale is reported in [10–11] where an external actuating force is mechanically transmitted to the rotor through a central shaft. The rotor consists of a 500 μm thick single-piece annular multi-pole permanent magnet and a *back-iron* piece that concentrates the magnetic flux in the rotor-stator airgap. The stator has a three-phase multilayer planar coil. In a housing of 11.5 mm diameter, the device is capable of generating 2.5 W RMS power with 1.0 V_{pp} open circuit voltage at a rotational speed of 120,000 RPM.

Electromagnetic induction and piezoelectric transduction have also been exploited to create microsized power generators that rely on the resonant characteristics of a mass-spring-damper system to generate electricity, as reported in [12–15]. These devices yield maximum power when externally vibrating forces match the resonant frequency of the system. In vibration-based electromagnetic induction generators, like those presented in [12–14], an external vibration causes a permanent magnet to oscillate through a conductor coil, thereby inducing a voltage across its terminals. In vibration-based piezoelectric generators, like that presented in [15], an external vibration causes a proof mass to oscillate and stress a flexible structure that has been coated with layers of piezoelectric material, thereby straining the piezoelectric film and causing an electric charge differential to appear on the film surface. A comprehensive review of vibration-powered microgenerators is available in [16].

Micropower generators that require injection of a driving fluid have necessarily a flow output. Miniature combustion engines require fuel and produce gaseous emissions, as well as excessive noise and heat. Hence, generators like these cannot be packaged in a sealed container, similarly to the generators that have their rotor mechanically coupled to an external source of torque. As sealing is not possible in these devices, they cannot be used to power implantable medical devices, where complete isolation between the implant's inner parts and the live tissue is mandatory to prevent rejection.

On the other hand, though vibration-powered generators can be encapsulated and yield enough power to energize most biomedical implants, including pacemakers, their lifespan is severely compromised due to the fatigue failure of their vibrational springs. The fatigue failure occurs due to cyclic strain that flexible structures suffer over an extended period of operation. Furthermore, vibration-powered generators must be exposed to sustained vibrations at their specific resonant frequency for them to output maximum power; however, such conditions do not naturally exist in the human body where only low frequency quasi-periodic and random mechanical movements are present. These limitations cancel out the possibility of using this kind of devices to replace conventional batteries in long-duration biomedical implants, such as cardiac pacemakers.

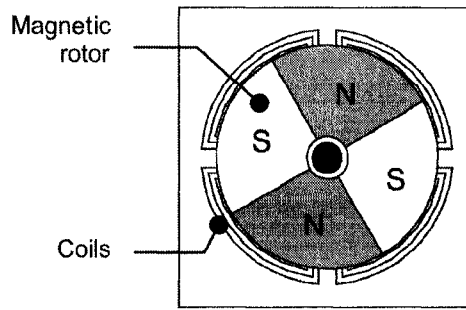
1.3.3 Electromagnetic Induction Micropower Generators

Electromagnetic induction permanent magnet microgenerators are of special interest due to their simple operation mode, their potentially high power density and efficiency [17]. Nowadays however, batch manufacturability, further miniaturization and enhancement of the total power output, power density and efficiency of these microgenerators face two major challenges: the implementation of physically small permanent magnets with strong magnetic properties, i.e. high remanence (B_r), high coercivity (H_c) and high energy product (BH_{max}); and the development of micro scale low-friction bearings. In [17], miniature and microscale permanent magnet power generators developed over the last decade are classified into three groups:

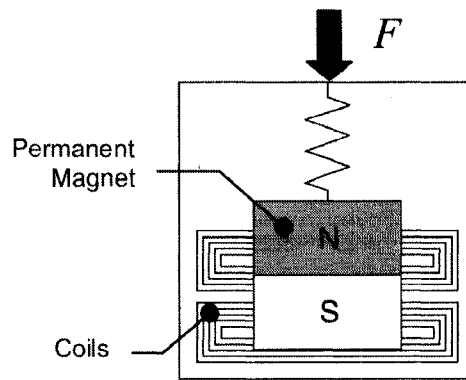
Rotational generators – Designed for continuous rotational motion under a steady driving torque provided by a fluid-powered microturbine or heat engine. A conceptual drawing of such generator is shown in figure 1a. They often operate at high rotational velocities, due to the small diameter of their rotor, thus enabling a high rate of change of magnetic flux per unit time. They can produce power in the order of tens of watts.

Oscillatory generators – A conceptual drawing of such generator is shown in figure 1b. They are driven by forced environmental vibrations in resonance mode and rely on small relative displacements between a permanent magnet and a coil. Operate at lower electrical frequencies and lower power densities than rotational generators. The basic design utilizes a mass-spring-damper system and maximum power is achieved at the mechanical resonant frequency. In the case of MEMS oscillatory generators said resonant frequency is well above the range of naturally occurring vibrations (1 Hz to 1 kHz).

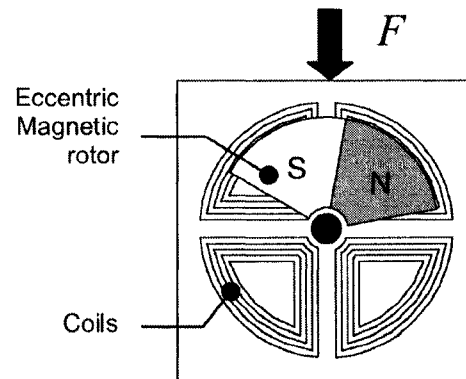
Hybrid generators – Shown in figure 1c this type of generators is intended to convert short oscillatory mechanical motion into rotational motion (from here the term “hybrid”) using an unbalanced or eccentric rotor that will rotate under forced acceleration of the pivot point. Depending on the operating conditions the rotation may be continuous, oscillatory or chaotic and the output power waveform will have a shape accordingly. These devices have been developed on the need for non-resonant generators that respond to linear vibrations in a broad spectrum of frequencies.



(a)



(b)



(c)

Figure 1. Three types of electromagnetic induction microgenerators [17].
 (a) Rotational generators, (b) Oscillatory generators, (c) Hybrid generators.

Though a few devices, like that in [8], do not belong to any of these categories, the above classification can be considered comprehensive. The author of [17] cites 14 small-scale electromagnetic induction power generation systems pertaining to the rotational category and 19 in the oscillatory category. Distinctive examples in these two categories are the devices of [9] and [14], respectively. In the category of hybrid generators four systems are cited: three of them are designed to power Automatic Generating System (AGS) wristwatches [18–23]. They have a non-magnetic oscillating weight that occupies the rear portion of the watch and oscillates due to the movements of the wearer’s wrist. The oscillating weight can either drive a gear train that increases rotational speed by hundred times and spins a small permanent magnet generator [18–21], or wind a circular spring that when reaches a maximum torque is released, starting a millimeter-scale generator through a gear train [22–23]. The fourth hybrid system [24] cited in [17], consists of a pendulum, formed by two permanent magnets in opposite polarities, that oscillates freely around a shaft across a set of six round-shape conductor coils accommodated in circumference beneath the rotation plane of the pendulum. In a computer simulation, this hybrid generator is placed in horizontal or vertical position and exposed to radial short-distance continuous vibration, seeking to cause a self-sustained rotational movement of the pendulum, thereby producing continuous output of electricity. The aim of the device is to convert small amplitude linear vibration into rotary motion, not stochastic movement, like the non-resonant generators used in watch industry. Results of simulation of millimeter-scale and microscale devices in [24] suggest the feasibility to produce a MEMS generator of this design with a pendulum of 440 μm length. In a 1.5 cm^3 prototype, built with conventional windings and two millimeter-size NdFeB magnets mounted on a pendulum, a vibration of 75 μm amplitude at 80 Hz is capable to induce synchronous rotation at 4800 RPM and generate 3 mW power.

1.3.4 In-body Micropower Generation

In an attempt to substitute batteries in medical implants for other more reliable long-term power sources, the physical or chemical conversion of different forms of energy present in the human body into electricity has been explored since the 1960’s [25].

The authors of [25] presented a macro scale handmade variable capacitance electrostatic power generator to be driven by the contraction of the heart ventricles during the heartbeat, aiming to produce power for a cardiac pacemaker. The feasibility of the generator was demonstrated in a vibrating table that emulated the motion of the left ventricular wall following in real-time the readings of an accelerometer attached to a live canine heart. The generated power was supplied to a cardiac pacemaker, which then stimulated the animal heart. A mean power of $36\mu\text{W}$ was generated, which was enough to power the cardiac pacemaker for continuous generation and pacing for more than two hours. A simple variable-frequency variable-width pulse oscillator circuit made with off-the-shelf CMOS inverters was used as a constant-rate pacing cardiac pacemaker for the experiment. The electrostatic generator consists of an enlarged surface area variable capacitor with one of its plates fixed and the other movable and attached to a mass-spring system to form a linear resonant mechanism tuned to a harmonic component of the heartbeat in the range of 1 to 2 Hz, such that the capacitance of the variable capacitor changes by an external vibrating force and maximum power is attained at resonance. The total spring constant of the system was calculated to be 1100 N/m, and the total mass suspended by the steel springs was estimated to be 780 grams for a resonant frequency of 6.0Hz. The generator also requires a starting power supply, i.e. a battery, to charge the variable capacitor with an initial DC voltage only once at the very beginning of power generation.

The authors of [25] envisioned the MEMS technology as a means to produce a variable capacitor from a microfabricated comb-drive to reduce the size of the electrostatic generator. However some technical challenges place difficulties to the miniaturization and practical implementation of this generator: due to the small masses and relatively high spring constants of MEMS components the lowest resonant frequencies that can be achieved with a MEMS resonator are well above the range of the heartbeat vibrations; the generator requires an initiating power supply, which entails the incorporation of a battery to the system; the mechanical durability of the variable capacitor, made for the experiment of a honeycomb aluminum-polyester structure, and the fatigue failure of the spring-like flexible structures needed in the resonator are the factors that would determine the life span of a microgenerator of this type made with the MEMS technology.

In spite of this, the experiment successfully certifies that the motion of the heart is capable to drive a generator to produce power for a cardiac pacemaker that in turn maintains the heart motion, in this way giving rise to a closed loop self-sustained permanent power generation-stimulation system.

A bio-thermo-electrical generator has been reported in [26–27] to recharge a battery in an implantable device. The design exploits the Seebeck effect in which a voltage is created in the presence of a temperature differential between two junctions of dissimilar metals or semiconductors. The bio-thermal generator is to be implanted directly under the skin in order to exploit the temperature difference between the patient's body and the outer environment at opposite faces of the device. The patient is responsible for providing a continuous temperature difference, either putting on or taking off clothing, moving to a warmer or colder environment, or topically applying an irritant substance or ice.

In this approach large contact area surfaces are needed in order to assure sufficient heat transfer through the device, fact that complicates its miniaturization. Medical conditions like fever or stress, or physical activity can negatively affect the temperature differential necessary for power generation. As implantation of the device is to be done under the skin, it cannot be integrated to medical devices targeting deep-body organs, like cardiac pacemakers. Moreover, as this generator is intended to recharge a battery, the limited number of charge-discharge cycles of such a battery will eventually result in an early end of life of the implant.

The authors of [28–30] have presented a micropower fuel cell that employs oxygen and glucose in the blood stream and other ambient body fluids to produce electricity. In its electrochemical process, the fuel cell outputs water and CO₂ as byproducts, which the human body later on disposes. Capable to generate 100 nW power and 400 mV, the fuel cell comprises of two reaction chambers: the anode chamber and the cathode chamber, made of a biocompatible polymer, separated by a proton exchange membrane (PEM) and electrically connected through an external circuit by thin film gold electrodes. The anode chamber contains a live culture of yeast microbes that serve as a biocatalyst for the glucose that they employ as a nutrient. As the microbes metabolize glucose, electrons and protons are released. Electrons are collected by the anode electrode and then travel through an external load to the cathode electrode. In the cathode chamber, potassium

ferricyanide is used as an oxidant that accepts the electrons, thereby closing the external electrical circuit. Simultaneously, electrostatic attraction causes protons in the anode chamber to diffuse across the PEM into the cathode chamber, where they recombine with oxygen and form water. A nanoporous polycarbonate membrane keeps the yeast microbes trapped in the anode chamber but allows circulation of glucose into the chamber and wastes out of it. With pore size of 10 nm, the membrane also prevents antibodies, which size ranges from 10 to 25 nm, from entering the anode chamber, isolating it from the immune system.

The power produced by this fuel cell still falls below the power requirements of most medical implants. In the device, the production of electricity will continue as long as the yeast microbes survive. However, the delicate habitat inside the anode chamber, in close relation to the human organism, may be interfered and endangered by agents such as viral infections or medication, that can easily penetrate the porous membrane. Also medical conditions like diabetes may take the fuel cell to an unpredictable situation. In case of failure to preserve the health of the anode chamber microbes, a violent rejection process would be rapidly initiated by the immune system.

1.4 Principal Results

The outcomes of this research work are the following:

1. A MEMS electromagnetic induction axial flux permanent magnet (AFPM) brushless power generator has been developed for use in a cardiac pacemaker to replace conventional batteries. In the system, an asymmetrical planar rotor embedded with microfabricated NdFeB alternate-polarity permanent magnets oscillates around a central shaft due to the thorax motion during breathing to induce a voltage in two microfabricated planar copper coils embedded in two stators. The microgenerator does not need any external supply of fluid, as necessary in some other types of microgenerators.
2. Two different rotor geometries: a semicircular one and a circular one with a destabilizer have been investigated. With a $1 \times 1 \text{ mm}^2$ rotor footprint area the semicircular rotor microgenerator is capable of generating $397 \mu\text{W}$ RMS power with

1.0 V open circuit RMS voltage per stator. The circular rotor microgenerator has a rotor footprint area of $3 \times 3 \text{ mm}^2$ and can generate 59.73 mW RMS power with 9.0 V open circuit RMS voltage per stator. The generated voltage and power are sufficient to meet the power requirements of a typical cardiac pacemaker.

3. A novel magnetization method to produce alternate polarity thin film micromagnets in close proximity was developed and verified through 3D finite element analysis simulation.
4. A nanoparticle based thin film solid lubrication system was identified as a suitable means to minimize wear and energy losses due to friction between the rotor and the shaft, thereby improving the efficiency and extending the lifetime of the microgenerator.
5. A detailed fabrication process sequence was developed to fabricate the device. The developed process sequence was verified by simulation using IntelliSuite, an industry standard MEMS design and fabrication tool.
6. A biocompatible mounting and actuation system that enables the thorax muscles to drive the proposed microgenerator from breathing was presented and designed to ensure power generation for the pacemaker even when the recipient is at rest.

1.5 Organization of Thesis

Chapter 2 of this thesis describes the basic components of the proposed microgenerator and their role in the system, as well as the underlying operating principle and the features that make the generator suitable to power medical implants. At the end of the chapter the medical devices that could benefit from using the microgenerator are mentioned. Chapter 3 explains function of a pacemaker as a therapeutic device and presents the requirements to be met by the microgenerator to supply power to a typical cardiac pacemaker. Then, the analytical model that allows estimation of the output voltage, output power and other relevant design parameters of the generator is detailed. The same chapter describes two possible rotor geometries that accomplish the operating principle of the microgenerator. The selection of magnetic material, deposition and micropatterning techniques necessary for the elaboration of the thin film permanent magnets in the rotor, as well as the magnetization procedure are also explained in this chapter. The features of the lubrication

system of choice are illustrated and finally the simulation results for the output voltage of the microgenerator are presented along with final specifications of two generator designs: one with a semicircular rotor and one with a circular rotor. Chapter 4 details the microfabrication process steps for the physical construction of the rotor and the two stators of the microgenerator and the procedure for assembly/encapsulation of these major parts into a single functional unit. Chapter 5 reveals a novel mounting and actuation scheme where the microgenerator is submerged in a liquid silicone ambient inside a soft silicone rubber capsule that provides biocompatibility between the microgenerator and the live tissue, at the same time offering a reliable way to maintain the oscillation of the rotor, hence power generation, when the recipient of the implant is at rest or sleeping, only relying on the contraction of the thorax muscles during breathing. The chapter begins with a description of the proposed mounting and actuation system, then introduces the pleural pressure in charge of driving the microgenerator and ends with a description of the forces that form the mechanical input to the microgenerator in the breathing actuation mechanism.

The conclusions section remarks fundamental observations and achievements of this research work and establishes its future direction in two senses: firstly, in the possibility of using the developed microgenerator as a power supply of medical implants other than pacemakers exploiting the motion of different organs in the human body; and secondly, in the suitability of integrating MEMS based supercapacitors to the microgenerator system as a means of energy storage in order to guarantee power availability for the target biomedical device during periods of inactivity.

CHAPTER 2

Device Concept

In this chapter the fundamental concept of the proposed bio-mechanically driven MEMS power generator is presented. Its fundamental components, their functions, and operating principle are explained. The chapter also covers the features that make the microgenerator suitable for medical implantable devices and points out the other possible target devices in which the microgenerator might be used as a power supply instead of a conventional battery.

2.1 Fundamental Structure and Components

A simplified single-stator conceptual model of the proposed MEMS power generator is shown in figure 2. The device comprises of a microfabricated planar asymmetrical rotor embedded with high coercivity permanent magnets in alternate polarities; a circular cross-section central shaft and a stator embedded with a microfabricated planar square cross-section copper coil. A pair of terminals provides connection of the planar coil to the external electrical load. A thin gap separates the free-to-move rotor from the underneath stator, as shown in figure 3.

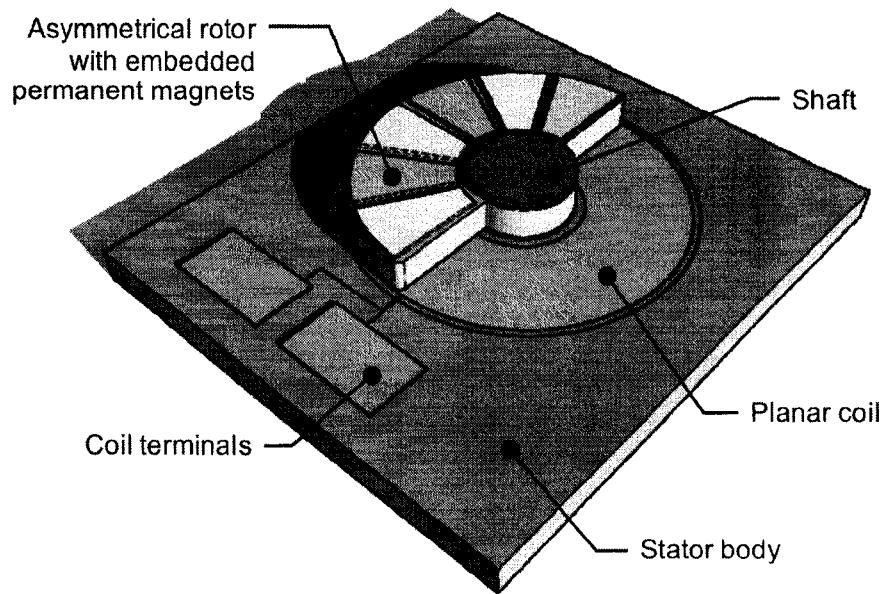


Figure 2. A conceptual 3D model of the microgenerator.

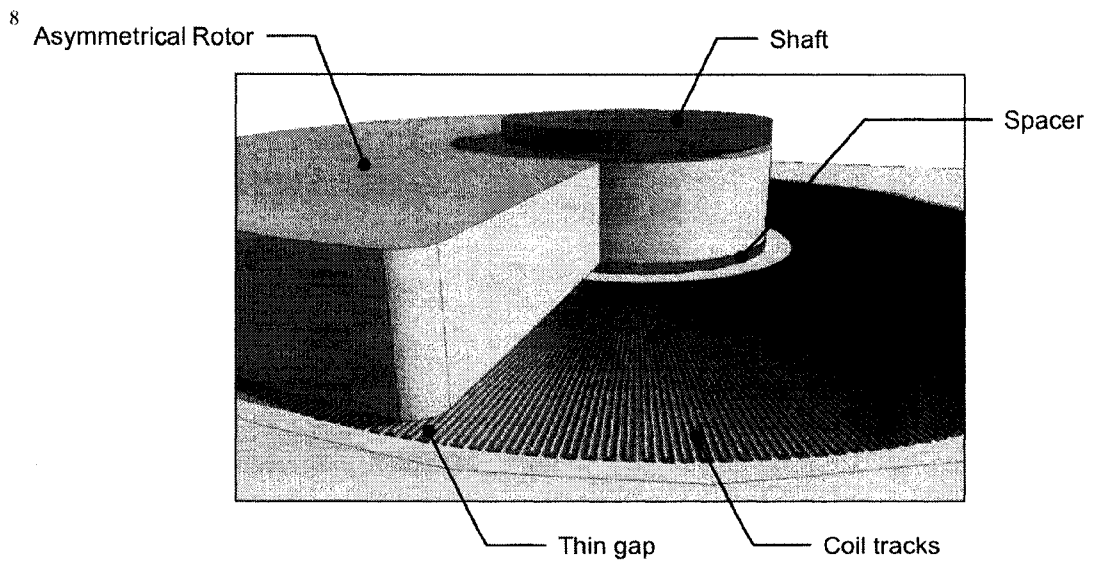


Figure 3. Close-up view of the 3D model of the microgenerator.

2.2 Operating Principle

The overall movements of the human body and the local movements of the region where the system is implanted provide driving force to the microgenerator. The motion of the thorax during breathing, head turning, mechanical activity of the extremities or even the movement of internal organs like the heart or stomach, cause the asymmetrical rotor to leave its initial stable position (figure 4a) and change its previous axis orientation (figure 4b), such that the Earth's gravitation alone can generate a torque that triggers oscillation of the rotor. The rotor oscillates for a certain time (figure 4c) and finally reaches a new stable position (figure 4d).

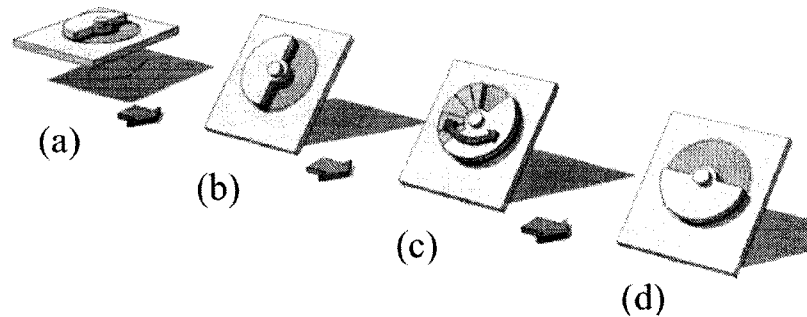


Figure 4. Operating principle of the microgenerator.

(a) Initial stable position of the rotor, (b) The rotor axis orientation changes on excitation, (c) The rotor oscillates after excitation, (d) New stable position of the rotor.

Due to the mechanical oscillation of the rotor, a changing magnetic axial flux cutting through the planar coil induces a voltage across its terminals following Faraday's Law of electromagnetic induction. The kinetic energy acquired by the rotor on excitation eventually dissipates and oscillation stops due to a couple of factors: (a) mechanical damping, caused by friction between the rotor and the shaft; (b) electromagnetic damping, caused by the induced current in the planar coil, that in turn causes a magnetic field that opposes the motion of the rotor. Once the kinetic energy of the rotor has been dissipated a new change in the orientation of the rotation plane is necessary to trigger a new energy generation cycle.

The voltage in the planar coil is generated in peaks, which are rectified, filtered, and stepped up to an appropriate DC level using microelectronic circuitry. Additionally, the

energy can be stored in a MEMS fabricated super capacitor to provide stable power to the target device even during certain periods of inactivity.

For its construction, according to the classification in [17], the microgenerator belongs to the category of hybrid generators. However is not intended to convert forced linear vibrations in the radial direction into continuous rotational motion, though it is capable to do this kind of conversion, but to convert changes in inclination angle (or axis orientation) and stochastic motion, which are the predominant situations in the human body, into rotational motion.

2.3 Key Features

The presented microgenerator does not carry potentially harmful liquid/gel agents and does not produce emissions/byproducts. Since no fluid injection or mechanical shaft coupling are necessary to drive its asymmetrical rotor, the microgenerator can be packaged as a self-contained unit in a sealed biocompatible encapsulation to eliminate the threat of leakage of body fluids towards the interior of the generator and escape of materials from it to the organism. Also, the microgenerator can be electromagnetically shielded to prevent electromagnetic interference (EMI) over the circuitry of the target device, as well as perturbations of strong external magnetic fields to the microgenerator system. The operation of the microgenerator is independent of the corporal temperature or the presence of any substance or live organism in the body ambient.

The microgenerator is much smaller than conventional pacemaker batteries and offers a much greater energy per unit volume. The smaller volume of the device also means a smaller amount of foreign material inside the body, therefore a better tolerance from the recipient and lower risk of rejection. Additionally, the generator does not produce noise or excessive heat, and differently from vibration-powered microgenerators, its functionality is not restricted to environmental vibrations sustained at a specific resonant frequency, because just a change in orientation is enough to drive the device.

Compared to other more complex generators, the presented device can be more reliable since it operates with only one movable part. Furthermore, the absence of elastically deformable structures in the system eliminates fatigue failure.

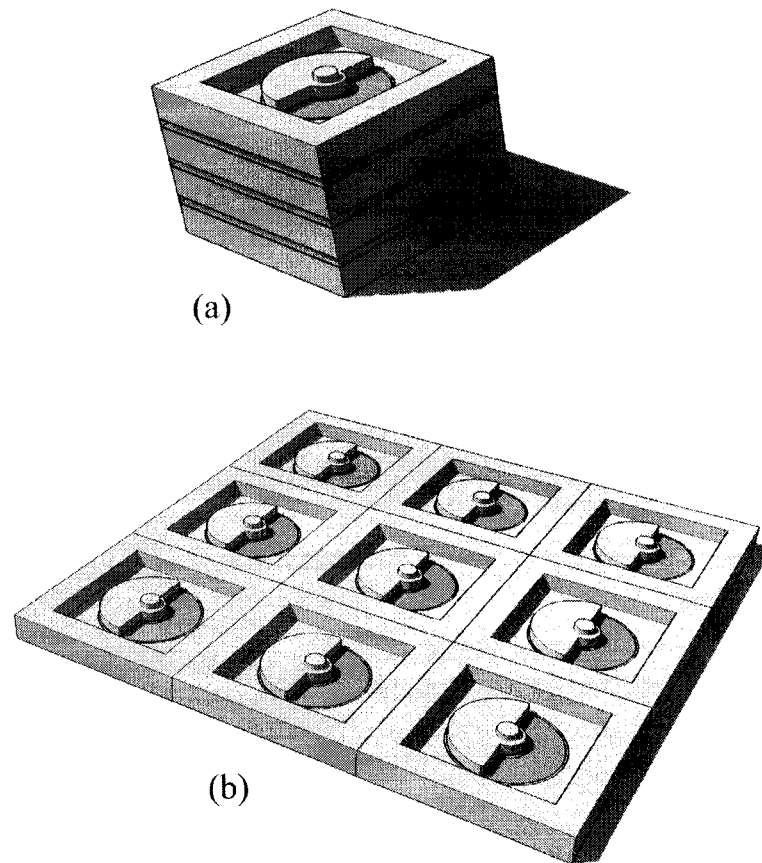


Figure 5. Stacks and arrays of microgenerators for increased power generation.
(a) Vertical stacks of microgenerators, (b) Horizontal arrays of microgenerators.

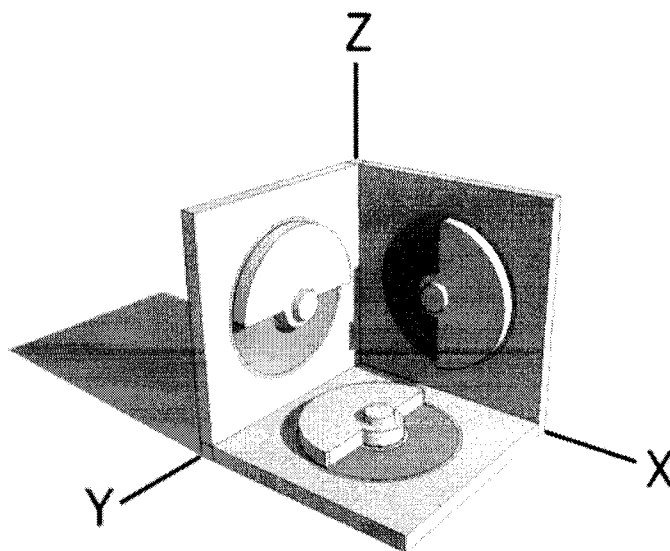


Figure 6. Multiple-axes mounting system of the microgenerator.

These two features can yield a maintenance-free energy source suitable to supply power to implantable devices over long periods of time and therefore minimize the frequency of invasive surgeries nowadays needed for replacement of an implant when its battery reaches the end of its lifetime.

The essential simplicity of the microgenerator allows its batch fabrication using the MEMS technology, and a number of these generators can be arranged vertically or horizontally, as shown in figure 5, or scaled up versions can be used to meet higher power demands. This modularity also enables the use of a multiple-axes mounting system, as shown in figure 6, to ensure power generation at any physical posture of the patient, e.g. standing or laying down on the back or on a side.

The device can be implanted in any part of the body, provided that it will be exposed to enough motion so as to produce sufficient power for the target device. In the case of modern pacemakers, as the person increases his/her physical activity, more energy is drawn from the battery, as more pulses have to be applied to the myocardium, hence more rapidly the battery exhausts. Conversely, for a pacemaker using the proposed microgenerator an increased physical activity of the patient would mean higher energy generation rate and power availability.

2.4 Target Application Areas

The design parameters of the microgenerator can be fine-tuned to meet the power requirements of existing electronic medical implants that already face the problem of limited energy content of batteries, e.g. cardiac pacemakers and defibrillators, cerebral pacemakers, hydrocephalus pumps, cochlear implants; as well as those implants in the stage of research and development that may greatly benefit from using an in-body renewable power source that permits integration and miniaturization, such as artificial retinas, ingestible video cameras and smart pills, continuous glucose-monitoring systems, muscle stimulators, integrated pain relief and drug delivery systems, in-body blood pressure telemetry sensors and mini autonomous surgical robots. The device can serve also as a power supply for low power integrated therapeutic devices to be anchored on the skin or external organs, such as hearing aid instruments, glucose-level-

measurement/insulin-liberation patches and other closed-loop physiological function controllers which perform blood sampling, analysis/diagnosis and drug delivery.

In this thesis, the design of the microgenerator will be optimized for its application in cardiac pacemakers, because the survival and long-term health of a recipient of one of these implants strongly depends on the power supply capacities of the pacemaker.

Chapter Summary

In this chapter the fundamental components and operating principle of a bio-mechanically driven MEMS power generator to overcome the problem of limited energy content of batteries in implantable medical devices have been presented, as well as the key features that enable the use of the microgenerator in biomedical implants and the possible target devices that could benefit from using the microgenerator. From these devices, cardiac pacemakers were chosen as the top-priority target device for which the design of the microgenerator will be optimized.

CHAPTER 3

Microgenerator Design

Supported on a brief description of the heart's excitation and conduction system, this chapter explains the role of a pacemaker as a therapeutic implant, then establishes its typical power requirements, to be met by the microgenerator, and presents the mathematical model that allows predicting the behavior of the microgenerator and optimizing its design parameters. Two possible rotor geometries for the microgenerator are proposed to create the instability that enables the Earth's gravitation to generate the driving torque. The selection of magnetic material, along with the deposition, micropatterning and magnetization techniques necessary to produce the thin film alternate polarity permanent magnets in the rotor are presented. Then, a nanoparticle based lubrication system is proposed to reduce friction between movable parts in the microgenerator as a solution to lessen energy losses and extend the lifetime of the device. Finally, simulation results for design verification are presented, as well as the design strategy employed to optimize the microgenerator for use in pacemakers and the final design specifications are summarized in a table.

3.1 Function of a Pacemaker

The heart is composed of four major muscles: the right atrium, left atrium, right ventricle and left ventricle, redrawn in figure 7 from [1], that make up the myocardium; and specialized muscular fibers that can be subdivided into excitation and conduction fibers, responsible of the regular pumping of the heart [1]. Those fibers in turn are classified into the following groups: the sinoatrial (SA) node, the internodal tracks, Bachmann's bundle, the atrioventricular (AV) node, the bundle of His, bundle branches and Purkinje fibers.

During normal sinus rhythm, the heart is controlled by the SA node, which depolarizes at a rate of 60 to 100 beats per minute. The right atrial internodal tracks and Bachmann's bundle conduct the SA-nodal activation throughout the atria, initiating a coordinated contraction of the atrial walls. Meanwhile, the electrical impulse transfers through the AV node that introduces a delay allowing the contraction of the atria to complete before ventricular contraction is initiated. Then, the bundle of His, bundle branches and Purkinje fibers conduct the electrical impulse at a high velocity while splitting the excitation throughout the two ventricles, enabling a coordinated and massive contraction [1].

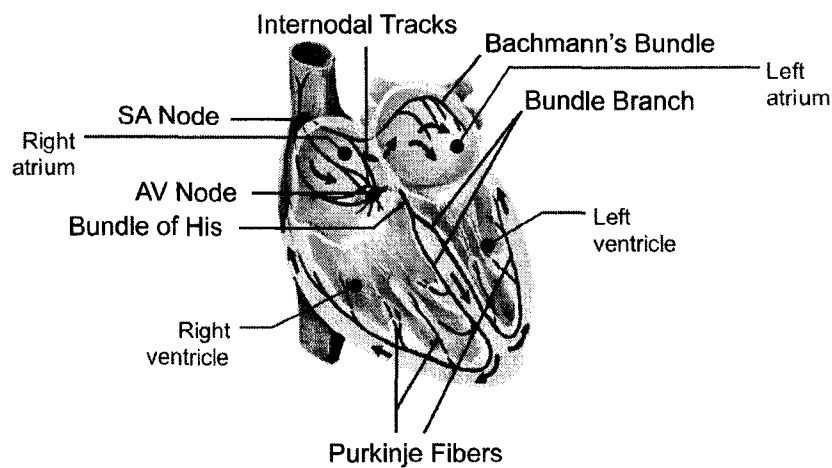


Figure 7. Excitation and conduction system and major muscles in the human heart [1].

These sequential contractions of the muscular fiber groups can be traced in the electrocardiogram (ECG) signal, redrawn in figure 8 from [1], which records the electrical activity generated by the heart. The baseline of electrical potentials in the ECG signal is known as the isoelectric line. The first ECG wave is the P-wave, which reflects the depolarization of the atria. Following the P-wave is the PR interval, a short relatively isoelectric period, related to the propagation delay induced by the AV node on the cardiac impulse in its way from the atria to the ventricles. Once the excitation reaches the ventricles, a rapid and large wave is observed, called the QRS complex or R-wave, that corresponds to the depolarization of the ventricles. Following the QRS complex, another isoelectric period, the ST interval, is observed. The ST interval represents the duration of depolarization after all ventricular cells have been activated. After the ST segment, the

ventricular cells return to their electrical and mechanical resting state, completing the repolarization phase, which is observed as the T-wave [1].

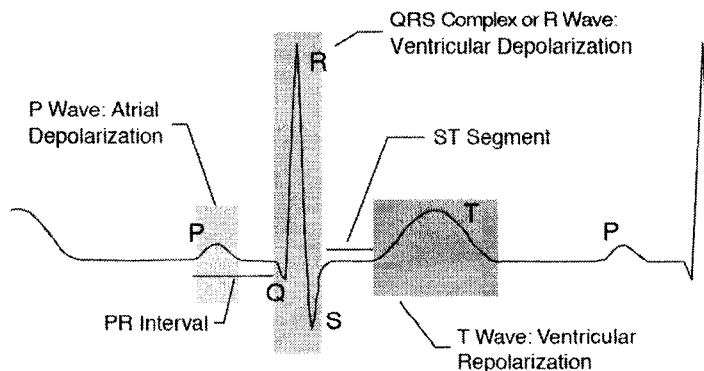


Figure 8. Typical electrocardiogram (ECG) and its characteristic waves [1].

Arrhythmia disorders entail the abnormal or irregular beating rhythm of the heart due to asynchrony of the cardiac chambers [1], negatively affecting the hemodynamic performance of the circulatory system. The therapeutic function of a cardiac pacemaker in the treatment of arrhythmia is to restore the synchrony between the atria and ventricles by applying controlled electrical pulses to the heart muscles.

3.2 Design Requirements

Redrawn from [1], a block diagram of a typical cardiac pacemaker is depicted in figure 9. For effective pacing, the output pulses of the pacemaker should have an appropriate width and frequency and sufficient energy to depolarize the myocardial cells in the vicinity of the electrodes. On successful depolarization, the electrical stimulation will propagate from the cells surrounding the electrodes to the neighboring cells throughout the entire excitation and conduction muscular fiber system of the heart, completing a contraction sequence.

The typical power supply specifications of a cardiac pacemaker are listed in Table 1 [1–4]. From Table 1, it is evident that the proposed microgenerator must generate at least 3.0 volts open circuit voltage to energize the control unit, the telemetry system and the sensors in the pacemaker, as well as to provide 3 to 6 μJ of energy per pulse to the

microelectronic Demand Pulse Generator (DPG). Higher power generation may help to include additional microelectronic-based functionalities in a future pacemaker system.

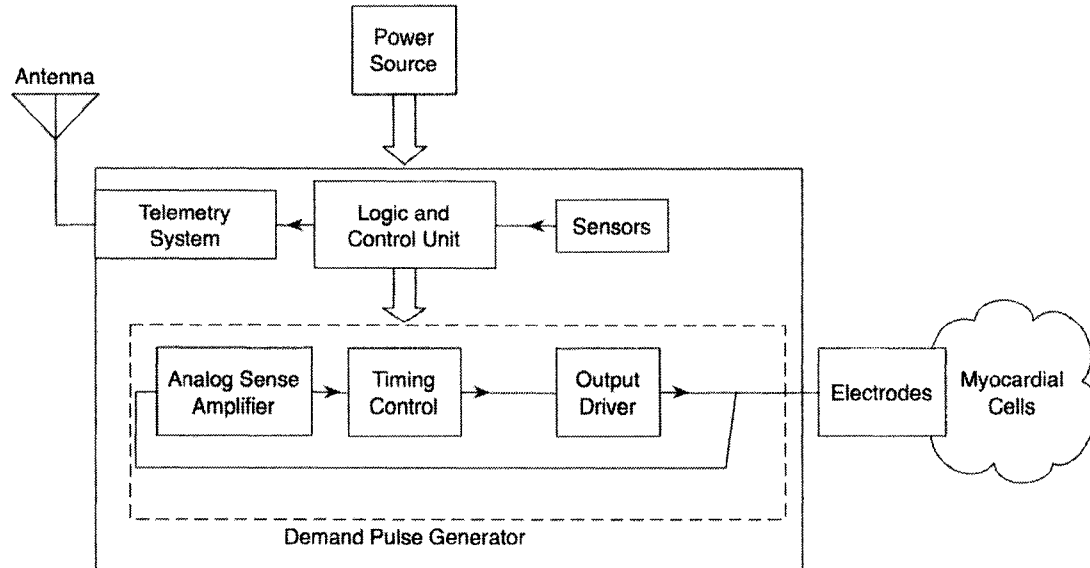


Figure 9. Block diagram of a typical cardiac pacemaker.

Table 1. Typical Cardiac Pacemaker Power Supply Specifications.

Parameter	Value	Unit
Battery open circuit voltage	3.0	Volts
Battery capacity	2	Ah
Pacemaker control unit voltage supply	2.2	Volts
Pacemaker control unit current drain	10	μ A
Pulse duty cycle	16.7	%
Energy consumption per pulse	3-6	μ J
Battery dimensions (length x width x height)	49 x 46 x 6	mm
% volume occupied by the battery in the pacemaker	50 (Approx.)	%

3.3 Mathematical Model of Axial Flux Brushless Power Generators

The induced RMS voltage across the terminals of a planar conductor coil exposed to a changing axial magnetic flux can be expressed as [9]:

$$V_{\text{RMS}} = 2\beta\sqrt{2} N_p^2 \Omega N_t B S \quad (1)$$

where β is a shape factor, N_p is the number of alternate polarity magnetic pole pairs in the rotor, N_t is the number of coil turns exposed directly to the axially changing magnetic flux, B is the remanence of the permanent magnets and S is the area of the planar coil covered by the pole pieces. Ignoring the fringing fields, the product βB represents the magnetic flux density in the rotor-stator gap.

The shape factor β as described in [10–11] determines the percentage of flux linkage between the rotor and stator and depends on the relative thicknesses of the permanent magnets embedded in the rotor, the planar coil and the gap between them, as shown graphically in figure 10, and is given by:

$$\beta = \frac{T_{pm}}{T_{pm} + T_{cl} + T_{ag}} \quad (2)$$

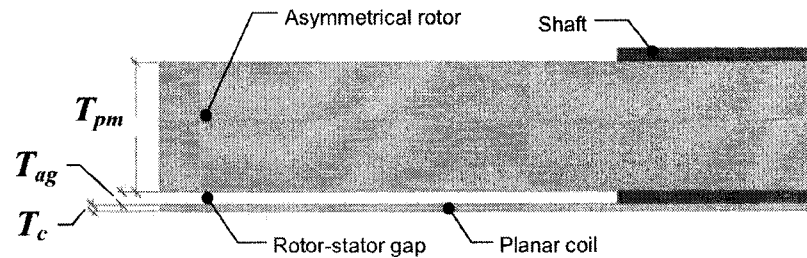


Figure 10. Thickness parameters used to determine the shape factor β .

where T_{pm} is the thickness of the permanent magnets, T_{cl} is the thickness of the coil layer, and T_{ag} is the thickness of the rotor-stator gap. The rotor is slightly thicker than the permanent magnets as the magnets are fully embedded in the structural material of the rotor body. As can be seen from equation (2), the thickness of the rotor-stator gap and the

planar coil should be kept to a minimum in order to obtain a shape factor close to unity to maximize the output voltage. The angular velocity Ω of the rotor in equation (1) can be determined from the relation:

$$\Omega = 4\sqrt{3} \sqrt{\frac{g \sin(\theta)}{R_p \pi}} \quad (3)$$

developed in this research work, where g is the acceleration due to gravity, θ is the instantaneous angular displacement and R_p is the radius of the rotor. The generated RMS power thus can be calculated from [9]:

$$P_{\text{RMS}} = \frac{V_{\text{RMS}}^2}{R} \quad (4)$$

where R is the total ohmic resistance of the planar coil.

3.4 Rotor Geometry

In this thesis two possible rotor geometries for the microgenerator were investigated: a semicircular rotor geometry and a circular rotor geometry.

Semicircular Rotor Geometry – A conceptual model of this geometry is shown in figure 11. In this approach, a number of alternate polarity permanent magnets or pole pieces are embedded in a semicircular shaped rotor made of a non-magnetic structural material. It is the asymmetrical shape of the rotor that causes it to leave its initial stable position in the presence of an external excitation. The Earth's gravitational attraction on the rotor center of mass, which has been displaced out of the rotation axis, generates the actuating torque, while the magnets embedded in the rotor are the source of magnetic flux that, as the rotor oscillates, fluctuates in direction and magnitude over the planar coils embedded in the stators, thereby inducing a voltage in them.

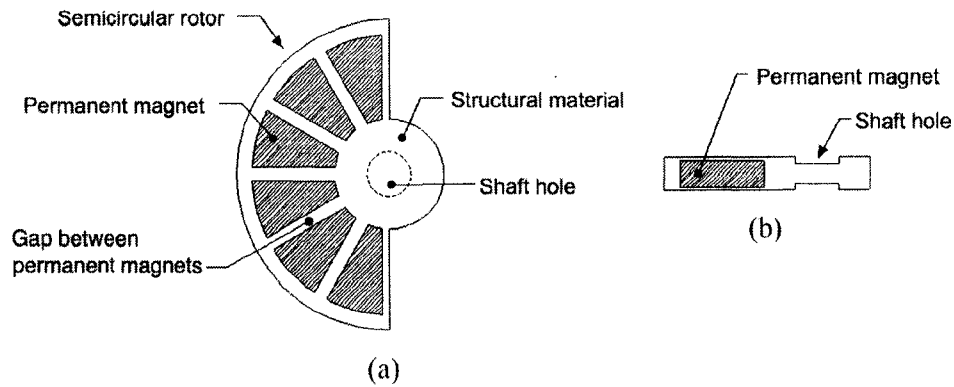


Figure 11. Semicircular rotor geometry.

(a) Top view of the semicircular rotor, (b) Cross-section view of the semicircular rotor.

Circular Rotor Geometry – In this geometry, depicted in figure 12, an asymmetrical destabilizer body made of a high mass density material, e.g. gold or tungsten, has been formed along a portion of the circumference of a circular rotor embedded with alternate polarity permanent magnets. In this configuration, it is the asymmetrical shape of the destabilizer what displaces the center of mass out of the rotation axis, enabling the Earth’s gravitation to generate the actuating torque. The major advantage of this geometry is that the entire area of the planar coils embedded in the stators is exposed to the changing magnetic flux created by the mechanical oscillation of the rotor, fact that contributing to a higher power generation.

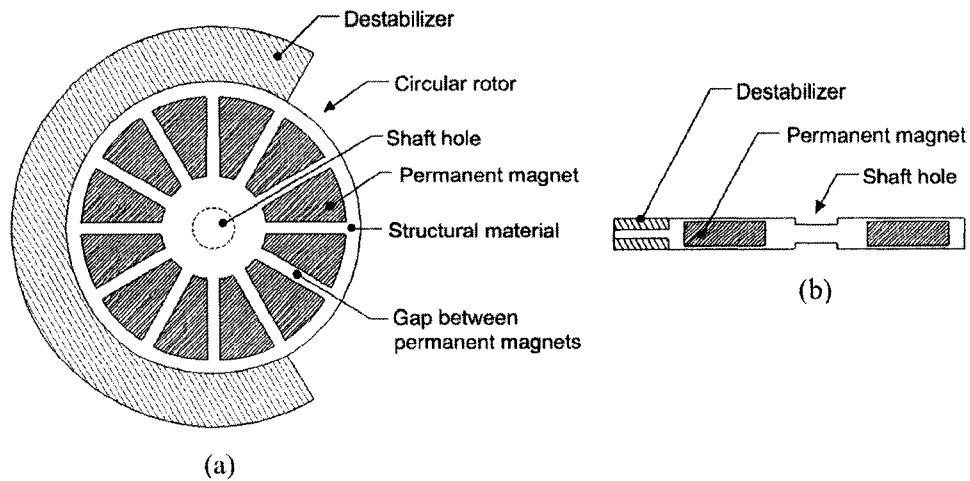


Figure 12. Circular rotor geometry.

(a) Top view of the circular rotor, (b) Cross-section view of the circular rotor.

The fabrication process of a microgenerator with a semicircular rotor will require fewer process steps and materials than a microgenerator that incorporates a circular rotor, hence the later will be more expensive. A semicircular rotor microgenerator occupies a smaller volume, however it cannot reach the energy generation capability of a circular rotor microgenerator. Additionally, in the circular rotor geometry the magnitude of the actuating torque, exerted by the Earth's gravitation on the rotor, can be controlled by changing the radius, thickness and material of the destabilizer independently of the dimensions or material of the rotor and permanent magnets.

3.5 Magnetic Material Selection

Investigation shows that the high coercivity $\text{Nd}_2\text{Fe}_{14}\text{B}$ (abbreviated NdFeB) crystalline system is the most suitable for the target design, since this magnetic material possesses the highest remanence and energy density compared to other modern hard magnetic materials such as Samarium-Cobalt (SmCo), Iron-Platinum (FePt), and Cobalt-Platinum (CoPt) [31–39]. NdFeB is a finely grained nanostructured material, which in bulk form can maintain maximum energy products of up to 50 MGOe (0.4 MJ/m) [32]. Although NdFeB permanent magnets have been produced in industrial scale since 1983 and there exist many ways to manufacture them, this alloy has not been used extensively in MEMS due to the lack of readily available deposition, etching, and magnetization techniques.

At present only magnetron sputtering and the pulsed laser deposition (PLD) methods [32–34] have been successfully applied to produce thin NdFeB films with properties comparable to those of bulk magnets. With magnetron sputtering, maximum film thickness of about 10 μm can be achieved in one deposition cycle [32]. Sputtered NdFeB films feature good mass density and coercivity in the order of 796 KA/m. On the other hand, NdFeB films deposited by PLD feature high purity and can be grown at rates of 50 to 100 $\mu\text{m}/\text{hour}$, with typically achievable remanence of 1 Tesla (T) and maximum achievable remanence of up to 1.5 T [33–34]. The PLD technique still faces technical problems that have prevented it to be widely used, e.g. lack of film uniformity over large substrate areas and splashing effects [34]. Despite this limitations, from the point of view of high deposition rate, the PLD method is a good choice for the fabrication of the NdFeB magnets for the proposed microgenerator. Regarding the low corrosion resistance

of NdFeB thin films, the micromagnets in the rotor are to be immediately coated with a protective layer before being exposed to air and to the strong etchants used to pattern other materials during the fabrication process.

3.6 Magnetization of NdFeB Magnets

A major design challenge to realize the MEMS microgenerator appears to be the alternate polarity magnetization of the deposited and patterned NdFeB thin film magnetic pole pieces embedded in the rotor. Although a number of different methods for alternate polarity magnetization are available [40-43], it appears that none of the methods is suitable for the microgenerator due to micro-sized dimensions and micrometer scale proximity of the pole pieces. After investigation, the author has developed a novel method of alternate polarity magnetization of very close proximity thin film magnets. The capacitor discharge magnetization circuit used for the developed Magnetic Flux Shielding Selective Magnetization (MFSSM) method is illustrated in figure 13. As shown in figure 13, in the magnetizing fixture two identical high-permeability (nickel, Permalloy®, MU-metal®) shielding plates with protruding teeth are placed above and below the set of thin film magnets to be magnetized. Then, the stack of shielding plates and magnets is secured between the poles of a commercial capacitor discharge magnetizer.

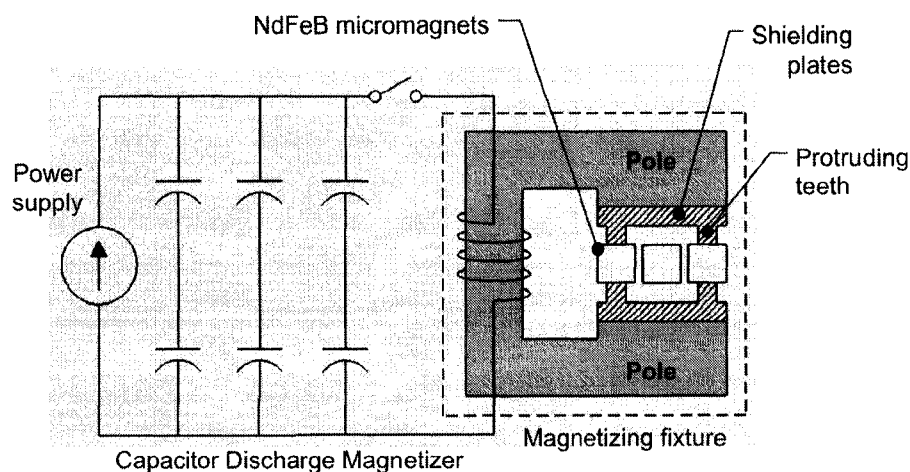


Figure 13. Capacitor discharge magnetization circuit used to implement MFSSM.

The two stages of the MFSSM method are depicted in figure 14. During forward magnetization, the magnetizing field H generated by the capacitor discharge magnetizer is directed towards the selected pole pieces by aligning them with the protruding teeth of the shielding plates. As a result a high permeability magnetic path is established through these pole pieces, whereas the pole pieces in between the aligned ones are placed in a low permeability magnetic path, i.e. they become shielded. Thus, when applying the magnetizing field in the first stage (figure 14a), the shielded pole pieces do not reach the magnetization saturation point of the material and remain unmagnetized when the field is withdrawn. In the second stage (figure 14b), the direction of the magnetizing field H is reversed while the protruding teeth of the shielding plates are aligned with the pole pieces that were shielded in the first stage. As a result, the pole pieces now in the high permeability magnetic path are magnetized in the reverse polarity and the magnetizing force through the shielded ones is not strong enough to switch their previously established polarity as they feature a high coercivity property.

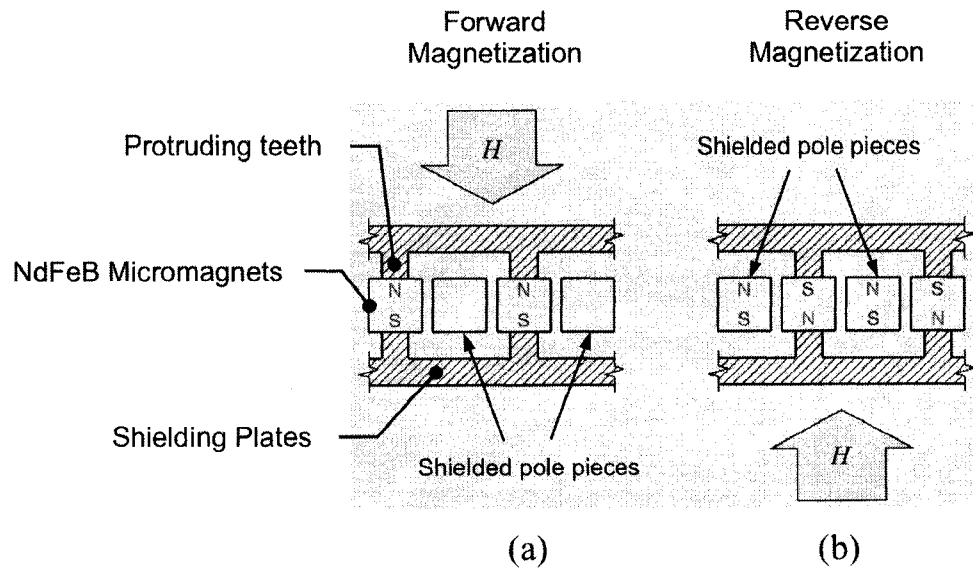


Figure 14. Stages of the MFSSM magnetization method.

(a) First stage – forward magnetization, (b) Second stage – reverse magnetization.

To verify the developed MFSSM magnetization method, a magnetostatic finite element analysis simulation was carried out using MagNet™. In the model used for the

simulation, as shown in figure 15, a set of three unmagnetized NdFeB thin film pole pieces are placed next to each other on the same plane and separated by an airgap.

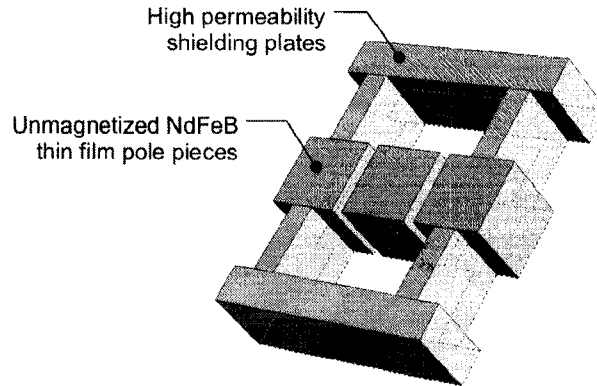


Figure 15. 3D Model used for simulation of the MFSSM magnetization method.

The shielding plates are placed on top and bottom of the magnet array, with their teeth touching the two NdFeB thin film pole pieces at the extremes. For more efficient meshing and shorter simulation time, the rotor structural material and the protective coating of the NdFeB thin film pole pieces were not included in the simulation. The model was then exposed to a constant and uniform magnetizing field produced by an infinitely long solenoid that plays the role of the actual capacitor discharge magnetizer. From the results of simulation, shown in figures 16 and 17, it is evident that most of the magnetic flux is confined within the magnetic path passing through the NdFeB thin film pole pieces at the extremes, while just a few flux lines cross through the NdFeB thin film piece in the center, i.e. the magnet in the center is being shielded from the magnetizing field. Figure 17 is a plot of the magnetic flux densities measured in a horizontal line that intersects the three micromagnets through the center. The peaks correspond to the magnetic flux density at the interior of the micromagnets on the extremes and the valley corresponds to the magnetic flux density in the shielded magnet. From figure 17, it can be seen that the magnets at the extremes receive a magnetizing force approximately five times greater compared to the shielded magnet. As a result, the magnets on the extremes will reach saturation earlier compared to the shielded magnet and will be the only ones in attaining a permanent magnet characteristic after turning off the magnetizing field. These

simulation results establish the validity of the developed MFSSM magnetization method that is to be used for alternate polarity magnetization of the permanent magnets embedded in the rotor of the microgenerator.

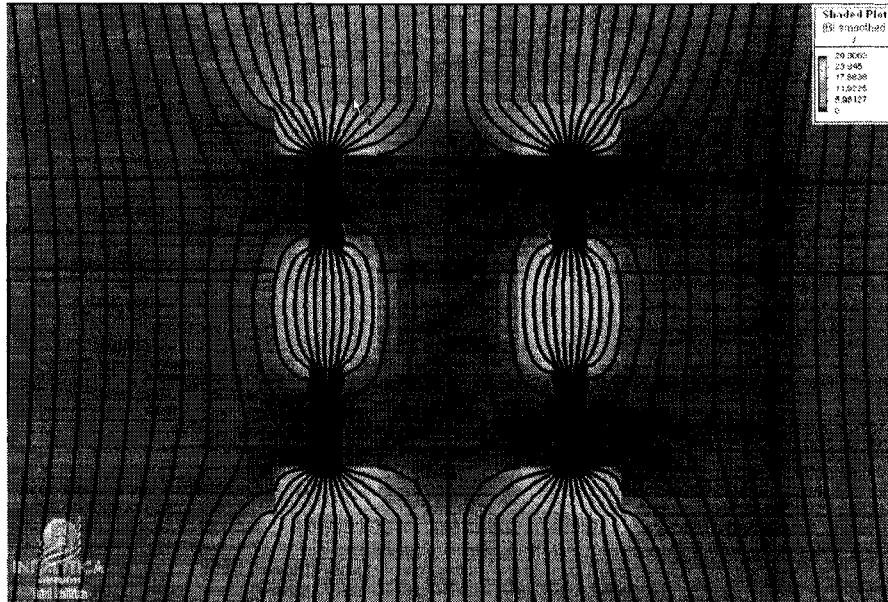


Figure 16. Simulation results of magnetic flux density in the MFSSM method.

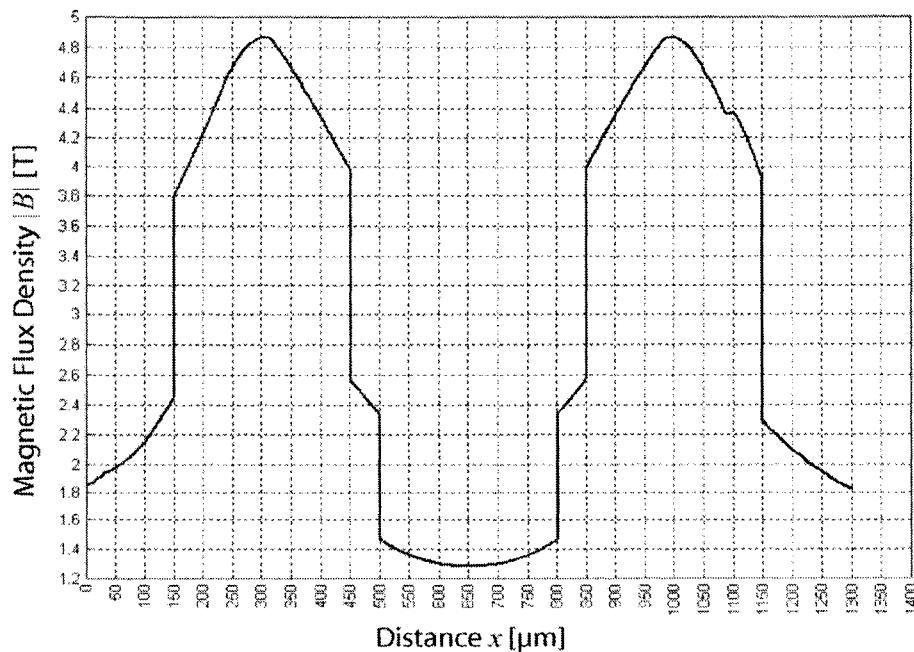


Figure 17. Magnetic flux density along a line crossing through the pole pieces.

3.7 Lubrication System

As the rotor oscillates around the central shaft, the friction at the interface between them, as shown in figures 18 and 19, will unavoidably wear these bodies and will produce losses due to frictional forces opposing to the movement of the rotor. If the rotor was made of a soft material, e.g. SU-8 (as used in [9]) and the shaft was fabricated of a hard material, like polysilicon, the rotor would wear very fast if no bearing or lubrication mechanism is incorporated to the system. Additionally, due to the small mass of the rotor, the magnitude of the frictional force may surpass the gravitational torque that causes the rotor to oscillate, thus preventing the rotor from moving or from reaching maximum angular velocity. However, if friction is controlled properly, energy losses can be reduced to allow satisfactory operation of the device and wear can be minimized to a point that the life span of the generator extends for the term of years. With this purpose a suitable lubrication mechanism must be incorporated in the system. The lubrication system of choice must meet the conditions of micro-scale manufacturability and batch fabrication capability. Furthermore, its tribological properties must remain the same during the anticipated life span of the microgenerator and it must not interfere with the magnetic/electric circuits in the microgenerator.

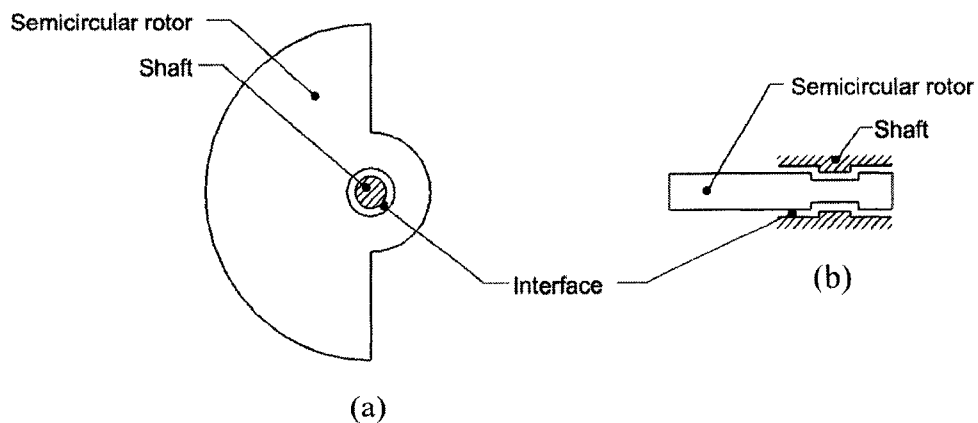


Figure 18. Detail of the interface between a semicircular rotor and the shaft.
(a) Top view of the semicircular rotor, (b) Cross-section view of the semicircular rotor.

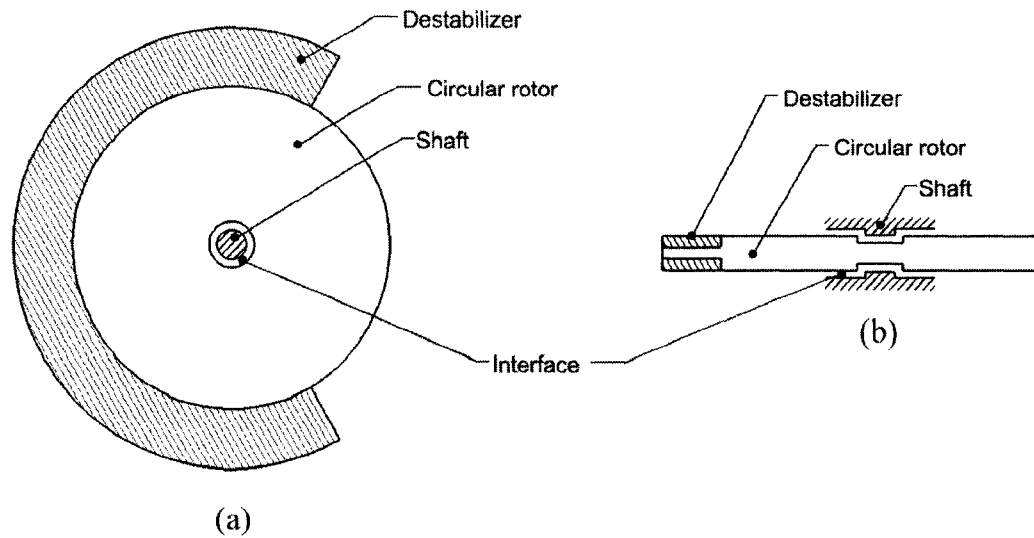


Figure 19. Detail of the interface between a circular rotor and the shaft.

(a) Top view of the circular rotor, (b) Cross-section view of the circular rotor.

Thin air film hydrodynamic lubrication systems, as used in [10–11], appear not to be suitable for the proposed microgenerator, as the low relative velocity between sliding surfaces of the shaft and the rotor does not allow the formation of an air film capable to keep separation between them, and also because the microgenerator is to be vacuum-sealed in order to minimize mechanical damping of the rotor. Conventional oil or silicone lubricants cannot be used either as their tribological properties are highly dependant on temperature, in vacuum they volatilize away, their surface tension and viscosity may be high enough to clog the rotor and the lubricant itself could be a source of contamination if leakage occurs through microscopic cracks in the walls of the microgenerator.

Many attempts have been made to improve the tribological performance of MEMS. As an example, some alcohols like propanol, ethanol, butanol or pentanol have been used [44] to produce ultra-thin low-viscosity liquid films on the surfaces of movable parts by condensation of alcohol vapor. Surface texturing is a friction reduction technique that entails the modification of the roughness of the sliding surfaces by means of selective surface etching, chemical treatment or laser machining [45]. Micro-sliders, used in magnetic data storage devices [46], are flexible structures that reduce the contact angle and contact area between movable parts and employ hydrodynamic lubrication to keep separation between them. Solid lubricants are a good alternative to friction reduction in

MEMS because a number of them can be deposited using standard microfabrication techniques, like chemical vapor deposition (CVD), epitaxial growth or electroplating [47]. Some most prominent solid lubricant films are those made of super-hard materials, like synthetic diamond or carbides containing tungsten, silicon, aluminum or titanium; also soft metallic films like TiN, silver and thick plasma-sprayed layers of chromia-molybdenum, zirconia-alumina and alumina-titania; self-assembled monolayers (SAMs) of methylated fluorocarbon and other organic compounds; thin films or powder of graphite, molybdenum disulfide or *Molybdenite* (MoS_2) and tungsten disulfide or *Tungstenite* (WS_2).

The major advantage of solid lubricants is that they can provide effective lubrication while eliminating the strong surface tension and high viscosity of liquid phase oil-based or silicone-based lubricants. Solid lubricants are also well suited for low speed or vacuum applications, where hydrodynamic lubrication cannot be created. These features make solid lubricants a suitable solution to reduce friction in the presented microgenerator.

An electroless deposited Ni-P-(IF- WS_2) composite solid lubricant film presented by [48] consisting of a suspension of inorganic Fullerene-like tungsten disulfide nanoparticles (IF- WS_2) aggregated to a nickel-phosphorus (Ni-P) alloy was developed and tested to compare its tribological performance with other Ni-P based solid lubricant films already being used as wear-resistant coatings. The IF- WS_2 nanoparticles, synthesized through the method described by [49], range in size from 100 nm to 200 nm and even though they are not perfect spheres, have a very definite boundary, which is the consequence of their multilayer closed crystalline structure that, differently from amorphous WS_2 nanoparticles, enables them to roll and slide.

The experiments to determine wear and friction coefficient of the different Ni-P films tested by [48] yield the results shown in Table 2. From Table 2, it is evident that the Ni-P-(IF- WS_2) film possesses considerably better tribological properties than other Ni-P based solid lubricant films.

Table 2. Wear and Friction Coefficient of different Ni-P thin films [48].

Thin Film	Mass loss of block (mg)	Friction Coefficient
Ni-P	15.6	0.090
Ni-P-(2H-WS ₂)	5.2	0.062
Ni-P-Graphite	4.3	0.067
Ni-P-(IF-WS ₂)	3.0	0.030

According to [48-49] and [52], the favorable tribological properties of the Ni-P-(IF-WS₂) film are due to the ability of IF-WS₂ nanoparticles to roll/slide between interfacing surfaces; also, during friction, they are slowly released from the Ni-P alloy, providing continuous replenishing of lubricant material; they serve as spacers, preventing contact between asperities; they can fill up very small pores, contributing to reduce surface roughness; they associate with the wear particles and facilitate them to slide past the contact area, limiting abrasive wear; some particles exfoliate, yielding one-atom thick sheets of hexagonal crystalline structure that locally produce a superlubricity effect, also observed in graphite [50–51]. A conceptual 3D model of the Ni-P-(IF-WS₂) solid lubricant film is depicted in figure 20.

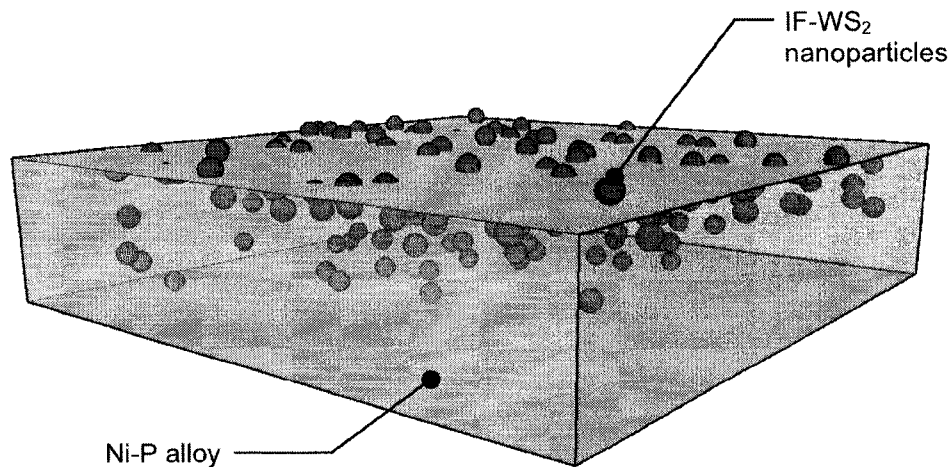


Figure 20. Conceptual 3D Model of the Ni-P-(IF-WS₂) solid lubricant film.

As can be seen from figure 20, some nanoparticles move freely on the surface of the film while the rest, to be released along time due to friction, is trapped in the Ni-P alloy.

Due to the good experimental performance of the Ni-P-(IF-WS₂) film, its ability to be integrated to a batch fabrication process, as it can be electroless deposited, and considering the complexities of implementing micro ball bearings, micro sliders and other solid or liquid lubricants, a thin coating of Ni-P-(IF-WS₂) around the central shaft was selected as the lubrication system to minimize wear and energy losses due to friction between interfacing surfaces of the shaft and the rotor in the microgenerator system.

3.8 Design Strategy and Final Device Specifications

Following equation (1), the major design objective is to minimize the overall volume of the microgenerator while optimizing the rotor size to increase the exposed face area S . Additionally, a double stator configuration, one above and one below the rotor will double the coupling area and thereby ensure higher power generation. Once the geometrical specifications of the rotor are fixed, the number and shape of the pole pieces are to be determined based on the capabilities of today's microfabrication technology to ensure manufacturability. To determine the number of pole pieces to be embedded in the rotor of the microgenerator, MATLAB™ simulations were carried out using the magnetic properties of NdFeB and plots of the maximum generated output voltage as a function of different number of pole pairs embedded in a circular and semicircular rotor are shown in figure 21. From figure 21, it can be seen that the circular rotor geometry with 12 pole pairs can generate 9.0 volts RMS voltage. The semicircular rotor geometry with 12 pole pairs can generate about 5 volts RMS voltage. Nevertheless, due to fabrication constraints, realization of such a high number of pole pairs in the relatively small area of a semicircular rotor is really challenging considering the capabilities of today's microfabrication technology. However, investigation shows that 6 pole pairs embedded in the semicircular rotor geometry enable easy manufacturability and can generate 1.0 volt RMS voltage in a 2 x 2 mm² microgenerator footprint area with a single stator. Three of such generators can be stacked vertically to meet the requirement of 3.0 volts power supply of a typical cardiac pacemaker. For a double stator configuration, only two generators will be required.

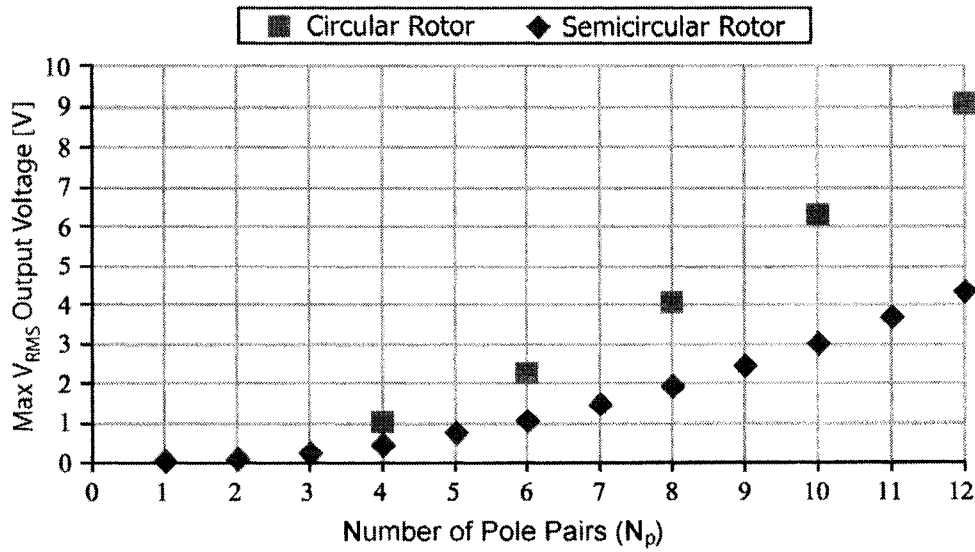


Figure 21. Maximum output voltage as a function of number of embedded pole pairs.

Figure 22 shows a plot of the rectified maximum generated output voltage waveform as a function of the angular displacement of the semicircular rotor for different number of pole pairs. Figure 23 shows the rectified maximum generated output voltage waveform as a function of the angular displacement of the circular rotor for different number of pole pairs. In both cases, a ring-shaped *back-iron* piece of soft (low-coercivity high-permeability) magnetic material has been used under the planar coil in the stator to avoid flux leakage and concentrate the magnetic flux in the rotor-stator gap. Based on the results presented in figures 21 to 23, 6 pole pairs have been chosen for the semicircular rotor and 12 pole pairs have been chosen for the circular rotor. The spacing between the rotor and the stator, number of coil conductors, conductor cross-sectional area, and conductor pitch have been determined to match the available copper deposition and etching capabilities of a standard microfabrication foundry as described in the next chapter.

Detailed specifications for both types of microgenerators are summarized in Table 3 and cross-sectional diagrams (not in scale) of the final microgenerator for both the semicircular and circular rotor geometries for a double stator configuration are shown in figures 24 and 25, respectively.

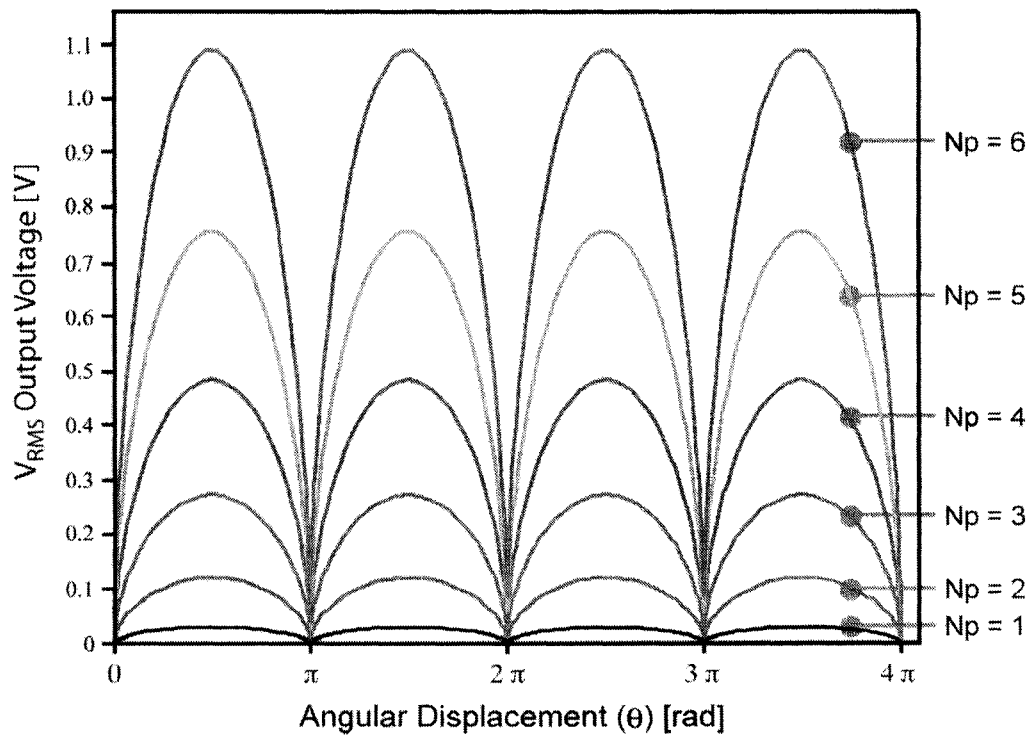


Figure 22. Output voltage waveform of a microgenerator with semicircular rotor.

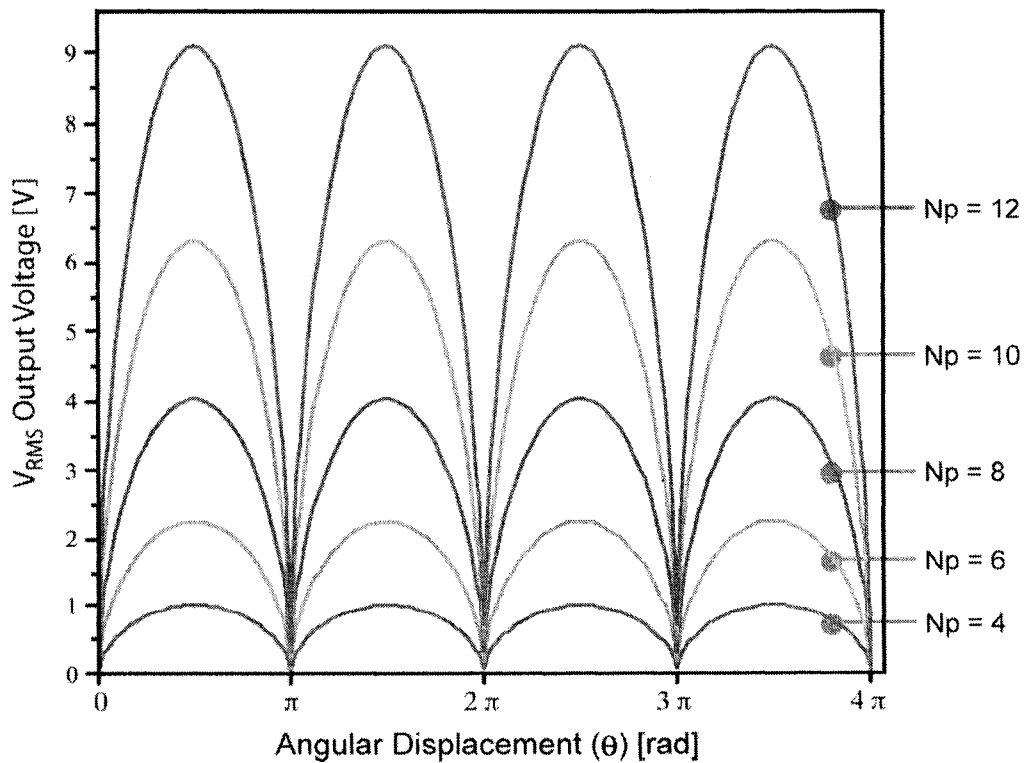




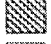

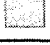
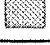



Figure 23. Output voltage waveform of a microgenerator with circular rotor.

Table 3. Final Design Specifications of the Microgenerator.

Parameter	Value		Unit
	Semicircular Rotor Microgenerator	Circular Rotor Microgenerator	
Footprint: length x width	2 x 2	4 x 4	mm
Thickness of micromagnets	100	100	μm
Thickness of coil layer	1	2	μm
Thickness of rotor-stator gap	14	13	μm
Generator total thickness	500	500	μm
Geometrical factor, β	0.87	0.89	
Radius of rotor	500	1500	μm
Total face area of rotor	0.393	7.069	mm^2
Cross section area per pole piece	0.040	0.111	mm^2
Rotor area covered by pole pieces	60.35	18.81	%
Maximum angular velocity	182.50	105.37	rad/s
Number of pole pairs in rotor	6	12	
Number of coil turns	259	179	
Coil cross section: height x width	1 x 1	2 x 2	μm
Remanence of micromagnets	1.1	1.1	T
Exposed coil face area	0.237	1.33	mm^2
Coil resistance	3.0	1.4	$\text{K}\Omega$
RMS open circuit voltage per coil	1.09	9.08	V
RMS output power per coil	0.397	59.732	mW

	Silicon		NdFeB		SU-8 Photoresist
	SiO ₂		Gold		Copper
	Epipoly		Ni-P-(IF-WS ₂)		Permalloy

Key of Materials

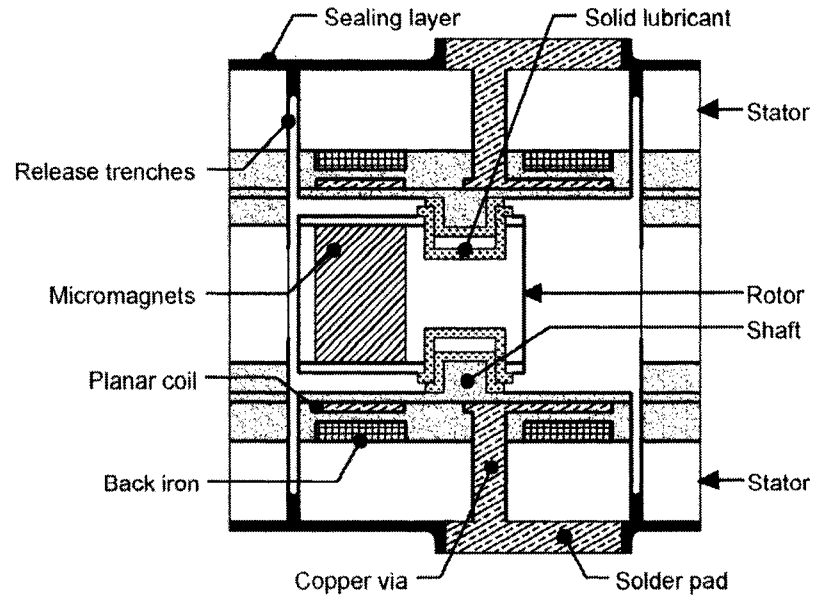


Figure 24. Cross-sectional view of the final microgenerator with a semicircular rotor.

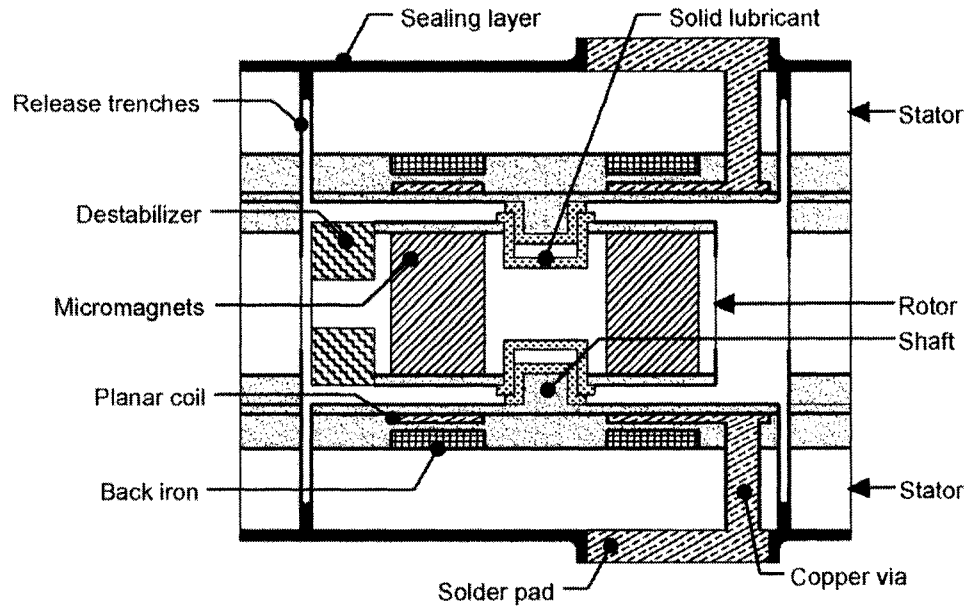


Figure 25. Cross-sectional view of the final microgenerator with a circular rotor.

Chapter Summary

In this chapter the function of a cardiac pacemaker as a therapeutic implant was defined in terms of the physiology of the excitation and conduction system of the human heart and the contraction sequence that takes place in it triggered by electrical impulses. The power supply requirements of a typical cardiac pacemaker were extracted in order to optimize the design of the microgenerator to meet such requirements. The analytical model that predicts the behavior of the microgenerator and allows optimization of its design parameters was presented. A semicircular rotor geometry and a circular rotor geometry with a destabilizer, both unstable in nature, were presented to enable power generation from the natural movements of the human body and key features of both were highlighted. The magnetic material for the thin film micromagnets to be embedded in the rotor was selected with the high-remanence, high-coercivity and high-energy product properties as the selection criteria and the deposition and micropatterning techniques necessary to produce such micromagnets were identified. A novel MFSSM magnetization method to produce alternate polarities in close-proximity thin film micromagnets was disclosed and proven valid through finite element analysis simulation. The suitability of a nanoparticle based lubrication system to minimize energy losses and wear by friction between the rotor and the shaft was justified. Finally, the design parameters of the generator were optimized to meet the power requirements of a typical cardiac pacemaker following a design strategy that takes into account constraints in the dimensions of the microgenerator and available fabrication capabilities as well as simulation results.

CHAPTER 4

Microgenerator Fabrication

This chapter describes the microfabrication process sequence developed to batch fabricate the microgenerator. The process sequence involves the fabrication of the rotor, the fabrication of the stator and finally the assembly of these parts into a single vacuum encapsulated functional unit. The mask sets, necessary in the etching steps, have been developed using IntelliSuite™ and validated through simulation to check for mask errors and geometrical compatibility. The deposition and patterning techniques for the major materials, as described in the previous chapter, have been determined by researching into the capabilities of existing commercially accessible microfabrication facilities in Canada and the United States to ensure manufacturability. The 3D models of the rotor and the stator, as generated by IntelliSuite™ after simulation of the fabrication process, match the design requirements. The generated step-by-step process tables and mask sets can be used by any standard microfabrication facility to fabricate the device.

4.1 Fabrication Strategy

The fabrication process of the microgenerator has been divided into three phases: rotor fabrication, stator fabrication and assembly/encapsulation. The following description and diagrams of the fabrication process refer to a microgenerator with a circular rotor. For a microgenerator with a semicircular rotor, the mask sets are to be replaced following the design specifications listed in Table 3 and the steps associated with the destabilizer fabrication are to be omitted.

The description of each process step is followed by the corresponding figure, showing on the left hand side the conceptual cross-section diagram of the structure at that step and to the right hand side the IntelliSuite™ generated 3D model of the process step simulation. The materials used in the fabrication process are represented in the conceptual cross-section diagrams as crosshatch shadings encoded in the material key of figure 26.



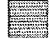


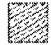



	Silicon		NdFeB		SU-8 Photoresist
	SiO ₂		Gold		Copper
	Epipoly		Ni-P-(IF-WS ₂)		Permalloy

Figure 26. Key of materials used in the fabrication process.

4.2 Rotor Fabrication

The rotor fabrication has been grouped into 16 major steps.

Step 1

On the bottom of a cleaned and two-side polished 100 μm thick <100> oriented silicon substrate, a 1.0 μm thick film of SiO₂ is thermally grown to serve as a seed layer, as shown in figure 27.

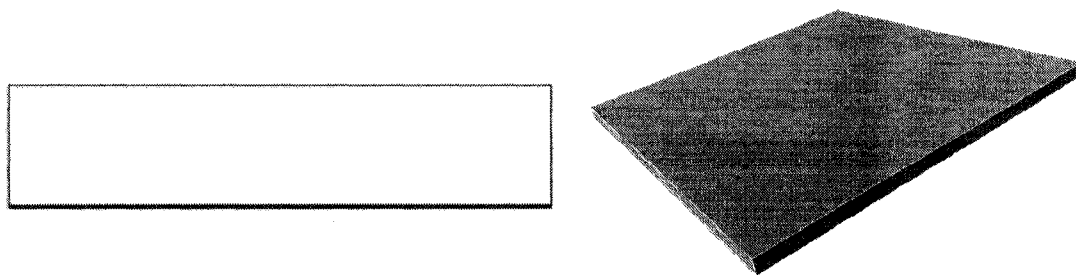


Figure 27. Rotor fabrication step 1 – thermal growth of bottom SiO₂ seed layer.

Step 2

A 15 μm thick film of epitaxial polysilicon (epipoly) is then grown on the SiO_2 seed layer [53] to serve as the first structural layer, as shown in figure 28.

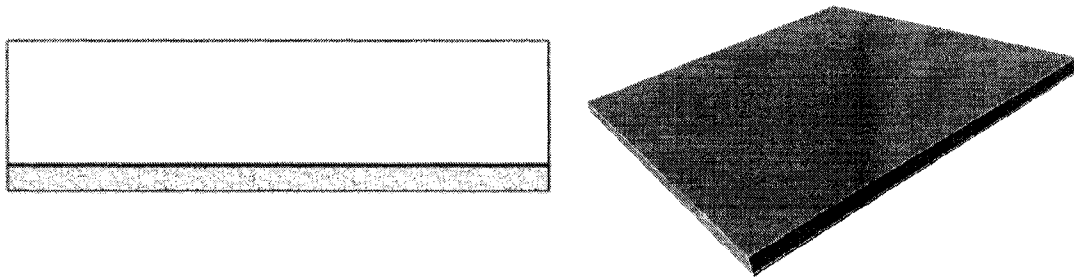


Figure 28. Rotor fabrication step 2 – growth of first epipoly structural layer.

Step 3

The wafer topside is then patterned using a photoresist and through etched using the advanced oxide etch (AOE) technique to create openings that will contain the NdFeB pole pieces, as shown in figure 29.

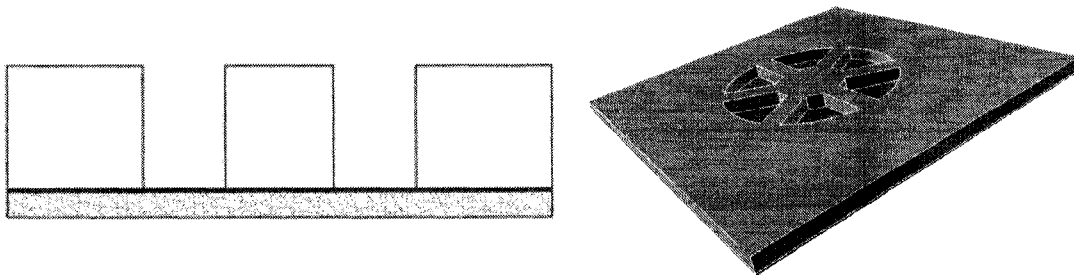


Figure 29. Rotor fabrication step 3 – patterning of openings for NdFeB pole pieces.

Step 4

A thick layer of NdFeB is then deposited on top of the wafer using the pulsed laser deposition (PLD) technique [39] up to completely fill up the openings for the pole pieces, as shown in figure 30.

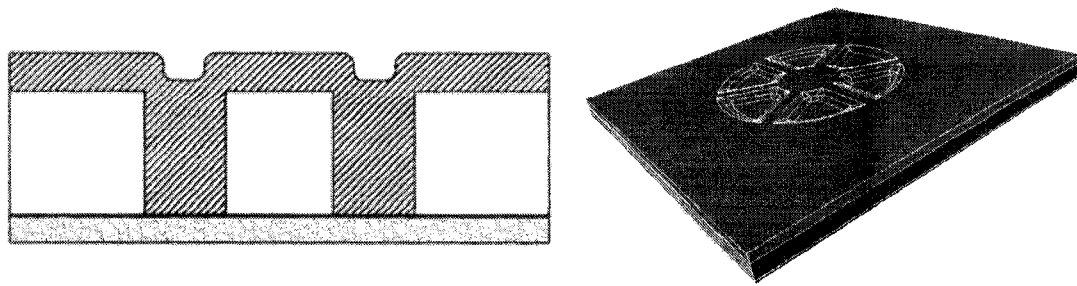


Figure 30. Rotor fabrication step 4 – deposition of NdFeB thick film using PLD.

Step 5

Excess NdFeB is then removed by mechanical polishing, as shown in figure 31. No chemicals are used at this step in order to avoid oxidation of the magnetic material and degradation of its magnetic properties.

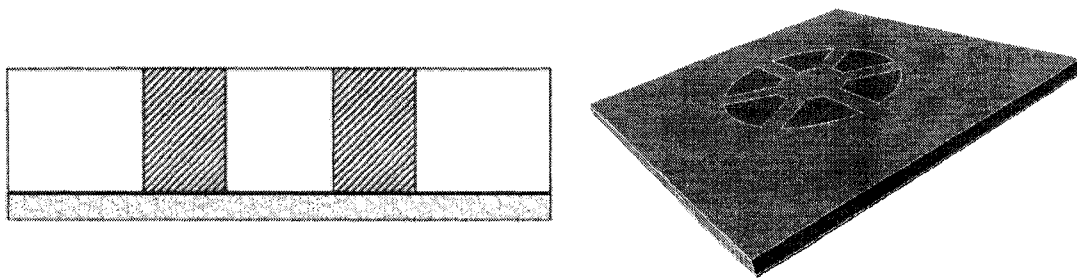


Figure 31. Rotor fabrication step 5 – removal of excess NdFeB by polishing.

Step 6

On the top of the wafer a new 1.0 μm thick seed layer of SiO_2 is then deposited using LTO LPCVD technique, as shown in figure 32.

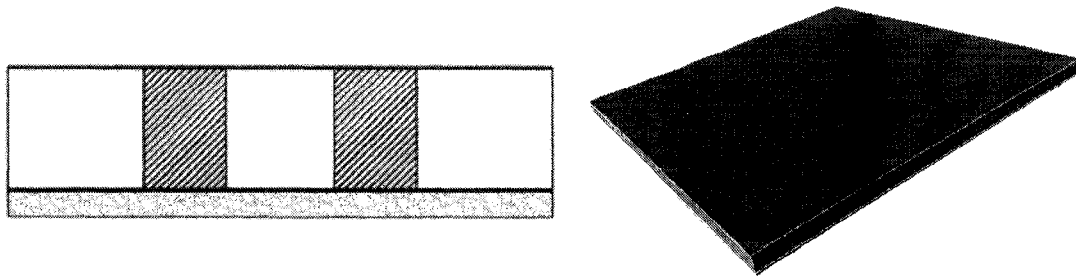


Figure 32. Rotor fabrication step 6 – deposition of SiO₂ seed layer on top of the wafer.

Step 7

A second 15 μm thick structural layer of epitaxial polysilicon is grown on the top SiO₂ seed layer, as shown in figure 33. This epitaxial layer encapsulates the magnetic material to protect it from corrosion and contamination during the rest of the fabrication.

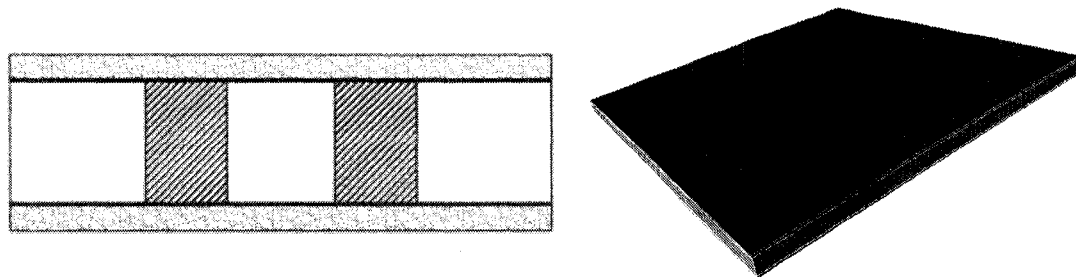


Figure 33. Rotor fabrication step 7 – growth of second epitaxial structural layer.

Step 8

To form the rotor-stator gap the top and bottom epitaxial layers are then patterned and partially etched to a depth of 10 μm, as shown in figure 34.

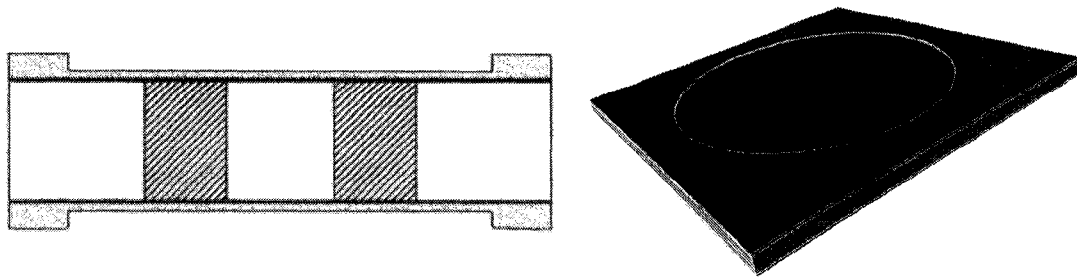


Figure 34. Rotor fabrication step 8 – patterning of the rotor-stator gap.

Step 9

The wafer is then partially etched from both sides using deep reactive ion etch (DRIE) technique to create 30 μm deep trenches with the shape of the destabilizer at the periphery and the shape of the shaft holes at the center, as shown in figure 35.

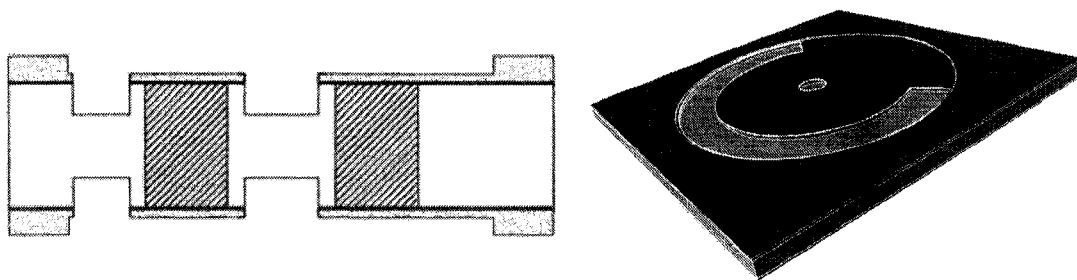


Figure 35. Rotor fabrication step 9 – patterning of destabilizer shape and shaft holes.

Step 10

A 30 nm thick seed/adhesion layer of Cr is sputter deposited on both sides of the wafer. Then, photoresist layers are deposited and patterned, leaving open only the destabilizer trenches. Connecting an electrode to the Cr seed layer through an opening in the photoresist, gold is electroplated to fill up the destabilizer trenches, as shown in figure 36.

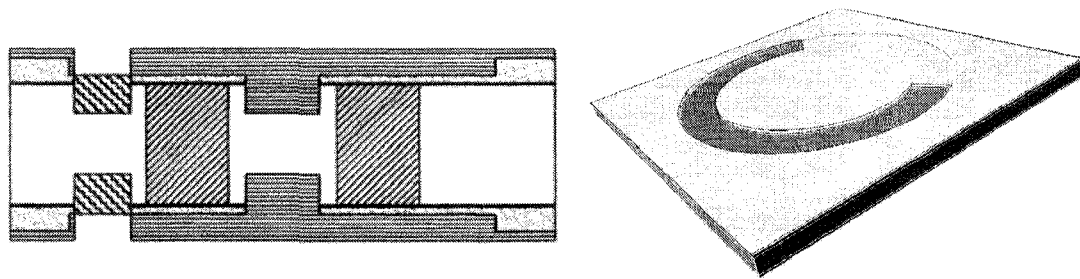


Figure 36. Rotor fabrication step 10 – electroplating of gold for the destabilizer.

Step 11

After electroplating the photoresist is stripped and a light bath of etchant is used to eliminate the remaining portion of the Cr seed layer. A 5 μm thick Ni-P-(IF-WS₂) conformal solid lubricant film is electroless deposited [48] on both sides of the wafer, as shown in figure 37.

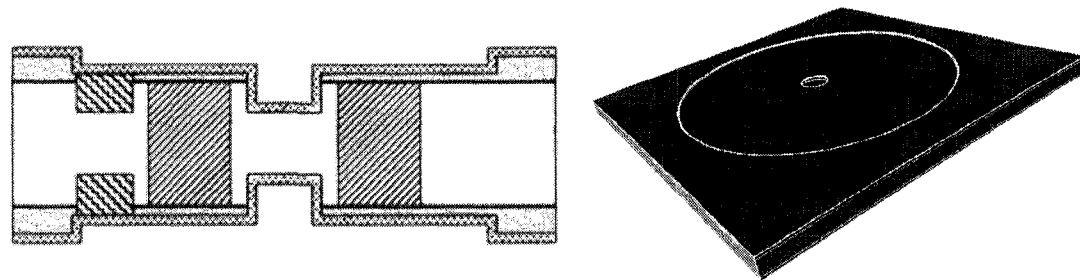


Figure 37. Rotor fabrication step 11– electroless deposition of solid lubricant film.

Step 12

The solid lubricant film on both sides of the wafer is patterned using a photoresist and etched using a Nitric-Acid/Acetic-Acid/Sulfuric-acid isotropic wet etch solution [52] to leave a thin coating of solid lubricant only in the shaft holes and at their vicinity, as shown in figure 38.

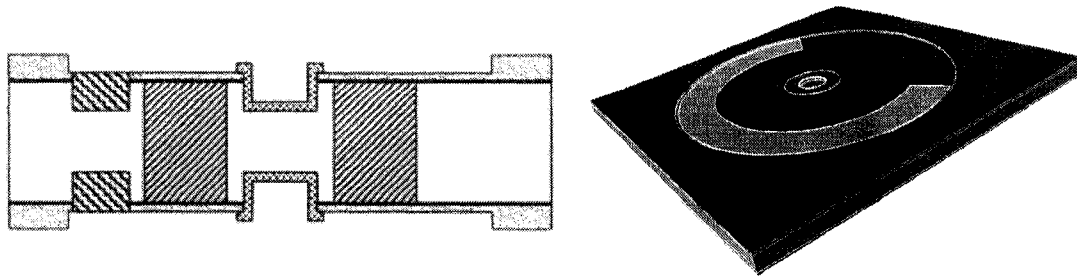


Figure 38. Rotor fabrication step 12 – patterning of solid lubricant film in shaft holes.

Step 13

A 5.0 μm thick SU-8 sacrificial layer is spin deposited on the bottom side over the epipoly layer, as shown in figure 39, to support the rotor when cut from the wafer in the subsequent process step.

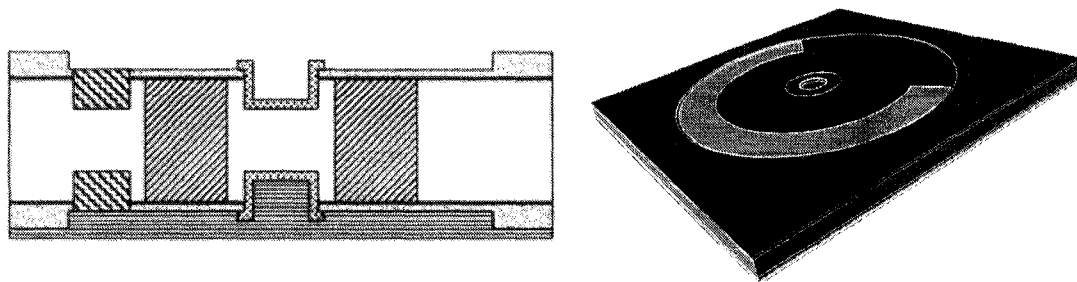


Figure 39. Rotor fabrication step 13 – deposition of bottom sacrificial SU-8 layer.

Step 14

The wafer topside is then patterned using a photoresist and DRIE-etched down to the SU-8 layer to create the rotor geometry, as shown in figure 40. At the completion of this step the rotor will be separated from the wafer, held in place only by the underlying SU-8 layer.

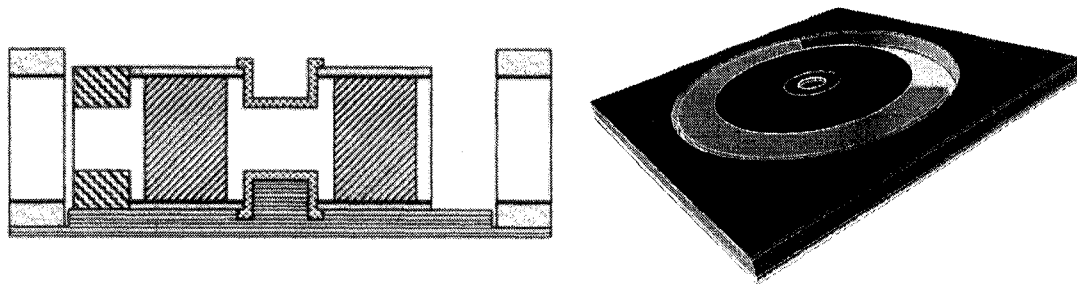


Figure 40. Rotor fabrication step 14 – patterning of the rotor geometry.

Step 15

Another 5 μm thick SU-8 layer is spin deposited on the top side over the epoxy layer, fully capturing the rotor, as shown in figure 41.

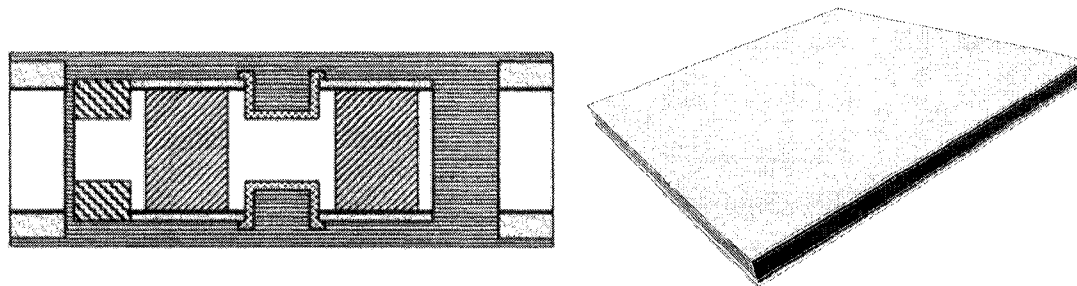


Figure 41. Rotor fabrication step 15 – deposition of top sacrificial SU-8 layer.

Step 16

Finally, the SU-8 layers are etched on both sides of the wafer to expose the structures and partially release the rotor, as shown in figure 42. This process step completes the rotor fabrication process. At this stage the magnetization of the pole pieces can be carried out. Full release of the rotor will be performed after assembly to the top and bottom stators, as explained in the assembly and encapsulation section later in this chapter.

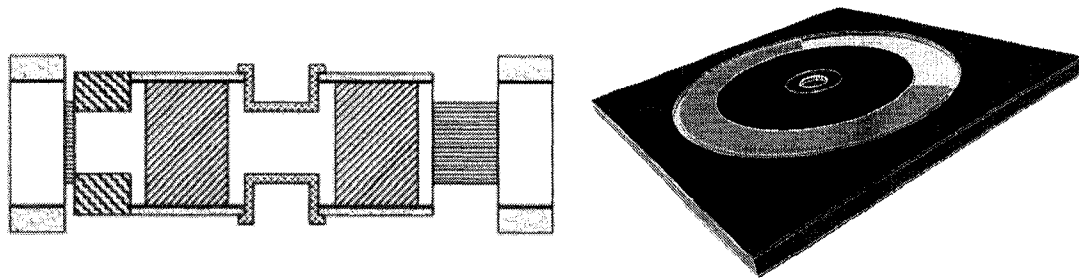


Figure 42. Rotor fabrication step 16 – partial release of the rotor.

The labeled cross-section view and full view of the completed 3D model resulting from simulation in IntelliSuite™ of the developed process sequence are shown in figures 43 and 44, respectively.

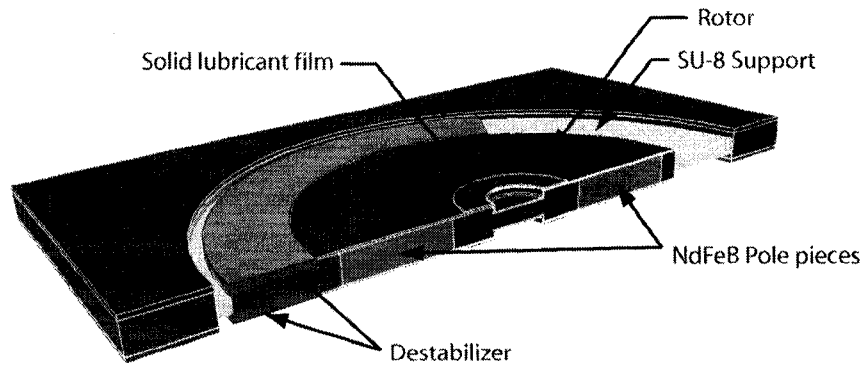


Figure 43. IntelliSuite™ simulation result of rotor process sequence (cross section).

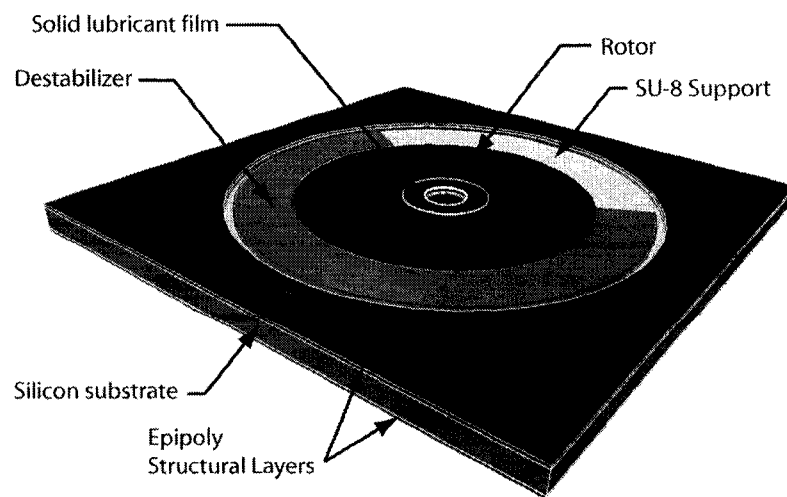


Figure 44. IntelliSuite™ simulation result of rotor process sequence (full view).

4.3 Stator Fabrication

The stator fabrication has been grouped into 14 major steps.

Step 1

A 1.0 μm thick film of SiO_2 is thermally grown on a cleaned and top-side polished 150 μm thick $\langle 100 \rangle$ oriented Silicon wafer, as shown in figure 45, to serve as an electrical insulation.

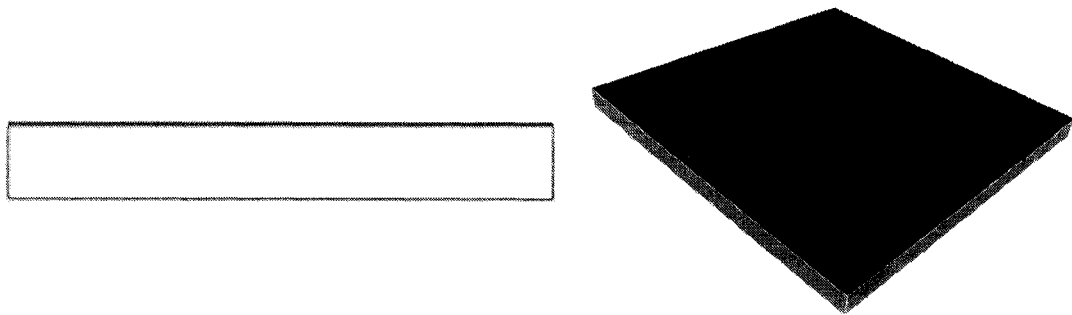


Figure 45. Stator fabrication step 1 – thermal growth of top SiO_2 insulating layer.

Step 2

A thin seed film of nickel is sputter deposited and then a 10 μm thick layer of Permalloy® (19% Ni - 81% Fe) is electroplated [54] on top of the oxide layer, as shown in figure 46.

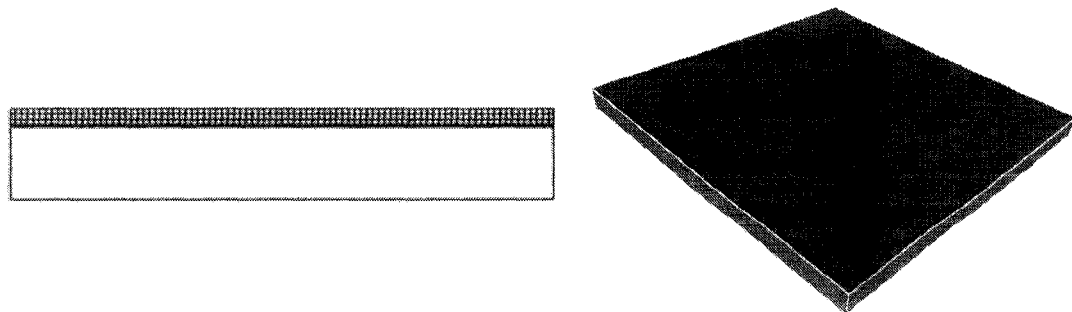
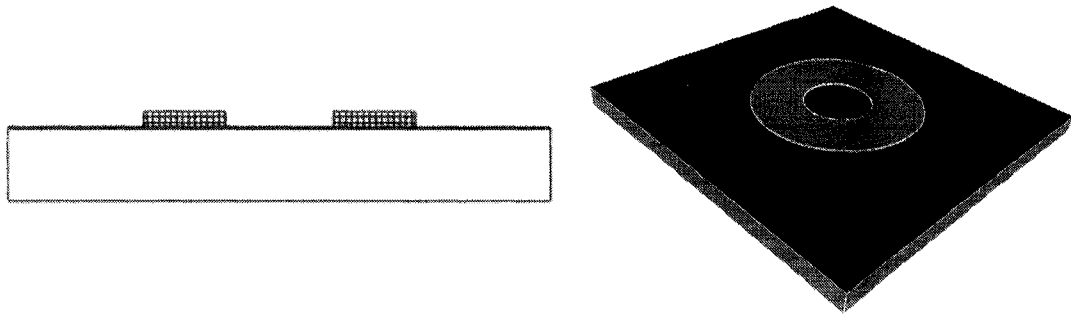


Figure 46. Stator fabrication step 2 – electroplating of Permalloy® layer.

Step 3

The Permalloy® layer is patterned with a photoresist and etched down to the oxide surface, as shown in figure 47, to form the ring-shaped back-iron piece that will concentrate the magnetic flux in the rotor-stator gap.



8

Figure 47. Stator fabrication step 3 – patterning of the back-iron piece.

Step 4

Another 1.0 μm thick layer of SiO_2 is deposited using LTO LPCVD technique and a first 20 μm thick epitaxial polysilicon (epipoly) structural layer is grown using the oxide as the seed layer. The epipoly layer is then planarized, as shown in figure 48. At the completion of this step the Permalloy® back-iron piece will be encapsulated and electrically isolated.

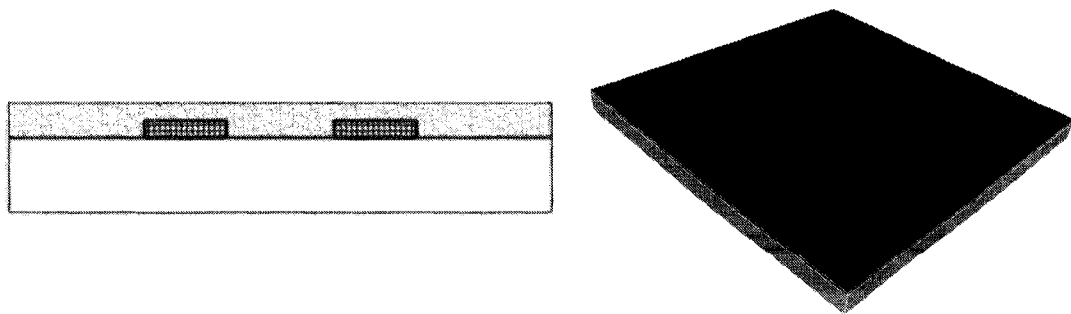


Figure 48. Stator fabrication step 4 – growth of first epipoly structural layer.

64

Step 5

Following the *Damascene* copper patterning technique described in [55–59], the epilayer is dry etched to create grooves for the planar copper coil tracks and its terminals, as shown in figure 49.

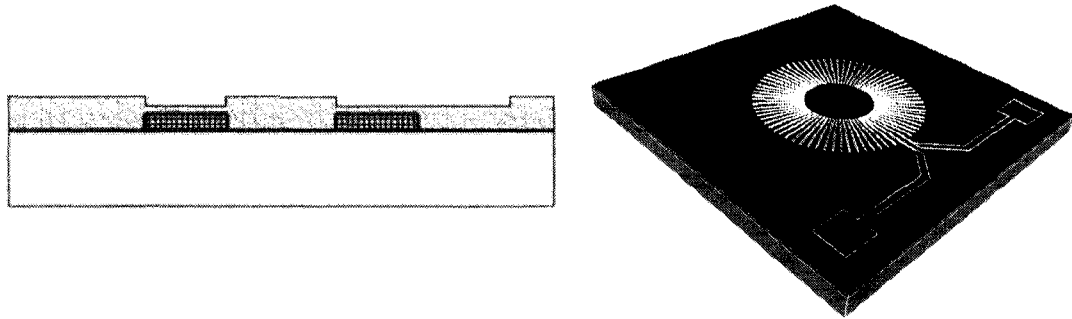


Figure 49. Stator fabrication step 5 – patterning of planar coil tracks and terminals.

Step 6

A 30 μm thick back-copper layer is electroplated on a sputter deposited thin copper film on the bottom of the wafer, as shown in figure 50.

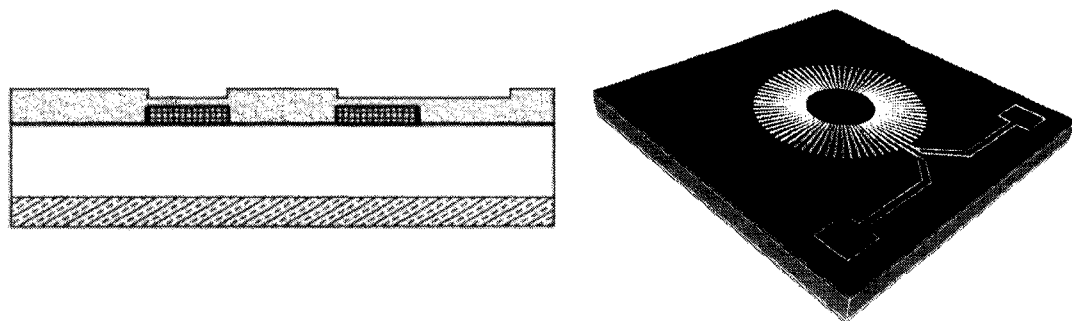


Figure 50. Stator fabrication step 6 – electroplating of back-copper layer.

Step 7

The wafer is then through etched using DRIE technique to form the vias that will connect the coil terminals to the external solder pads, as shown in figure 51. The back-copper

layer will serve in the subsequent process as the seed layer for copper to fill up the vias from their deepest zone.

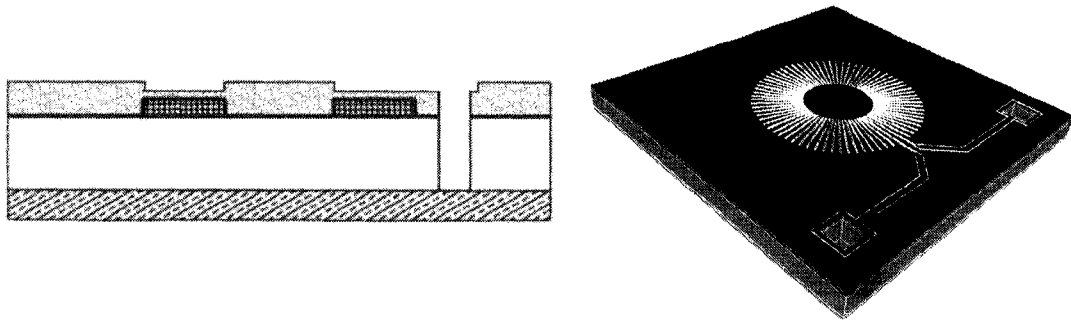


Figure 51. Stator fabrication step 7 – patterning of vias to the planar coil terminals.

Step 8

A 1.0 μm thick film of SiO_2 is thermally grown on the exposed surfaces of silicon and epipoly to provide electrical insulation. Then, a thin copper seed layer is sputter deposited on top of the wafer. Using this film and the back-copper layer as a near-electrode, a thick film of copper is electroplated on top. In this step the grooves defining the planar coil will be completely filled up with copper as well as the vias to the coil terminals, as shown in figure 52.

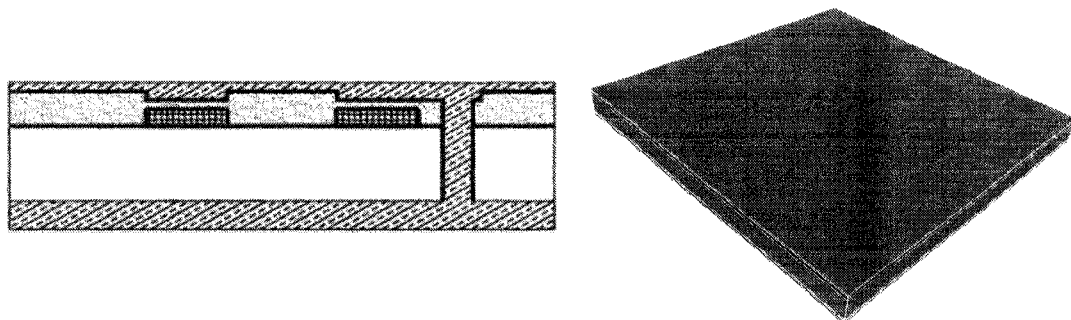


Figure 52. Stator fabrication step 8 – copper electroplating of planar coil and vias.

Step 9

Polishing removes excess copper down to the oxide layer, as shown in figure 53, completing this way the *Damascene* copper patterning process.

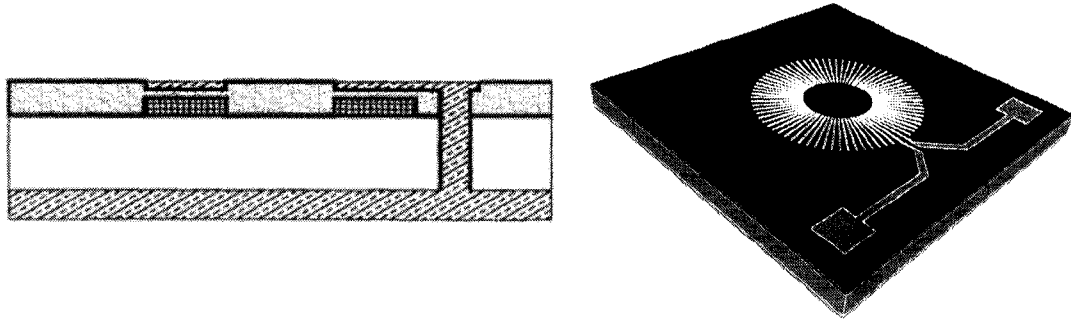


Figure 53. Stator fabrication step 9 – polishing of excess copper.

Step 10

A 1.0 μm thick seed layer of SiO_2 is deposited with LTO LPCVD technique to electrically isolate the planar coil and protect it from oxidation, which might reduce the small amount of conductive material if not controlled rapidly. A second 35 μm thick structural layer of epipoly is then grown on top of the oxide layer, as shown in figure 54.

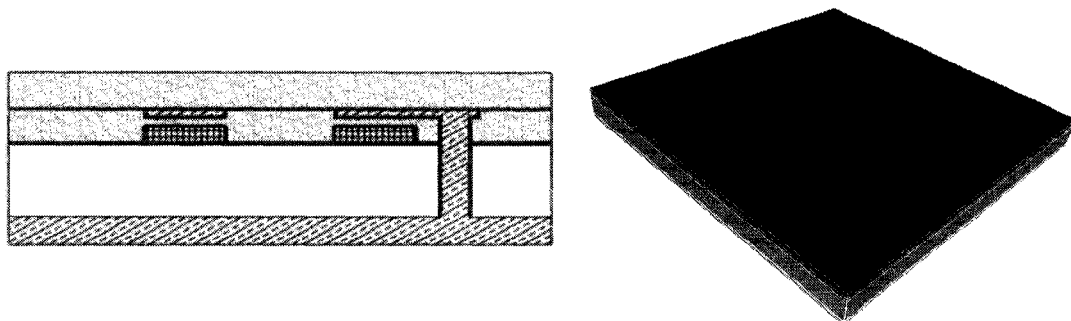


Figure 54. Stator fabrication step 10 – growth of second epipoly structural layer.

Step 11

The second epipoly structural layer is patterned and etched down to a 30 μm depth to create the shaft geometry, while a remaining 5 μm thick epipoly layer is left to protect the planar coil, as shown in figure 55.

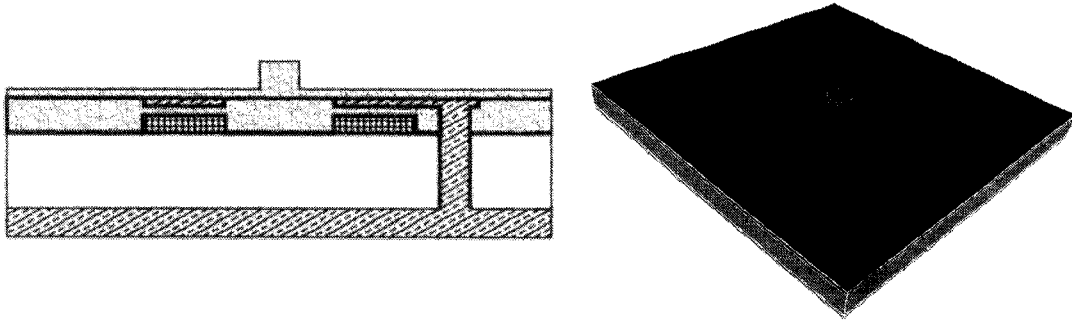


Figure 55. Stator fabrication step 11 – patterning of the shaft.

Step 12

A 5 μm thick Ni-P-(IF-WS₂) conformal solid lubricant film is then electroless deposited on top of the wafer, as shown in figure 56.

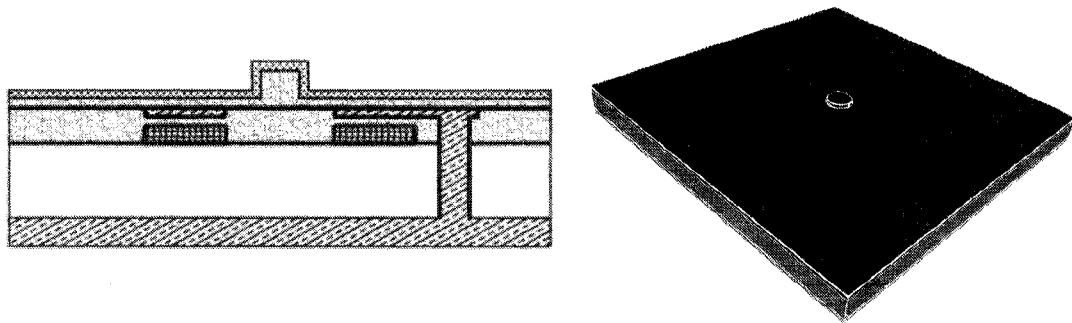


Figure 56. Stator fabrication step 12 – electroless deposition of the solid lubricant film.

Step 13

The solid lubricant film is patterned with a photoresist and etched to create a thin coating of solid lubricant only around the shaft, as shown in figure 57.

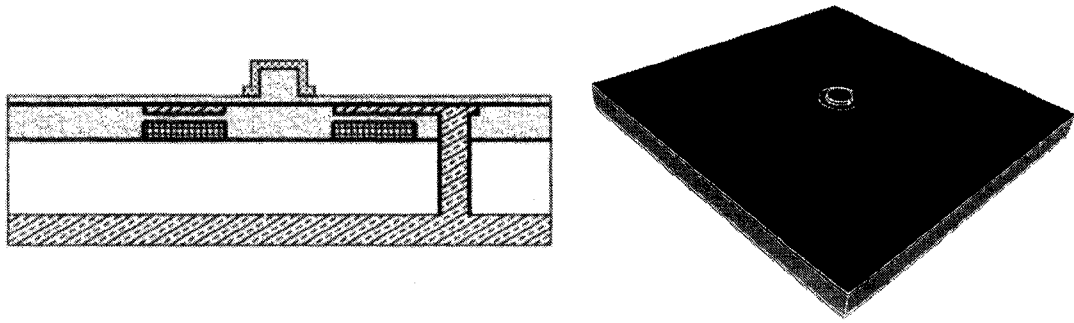


Figure 57. Stator fabrication step 13 – patterning of solid lubricant film around shaft.

Step 14

Finally, the wafer is through etched using DRIE technique, as shown in figure 58, to create the thin rotor-release trenches which function will be clarified in the next assembly and encapsulation section. This process step completes the stator fabrication process.

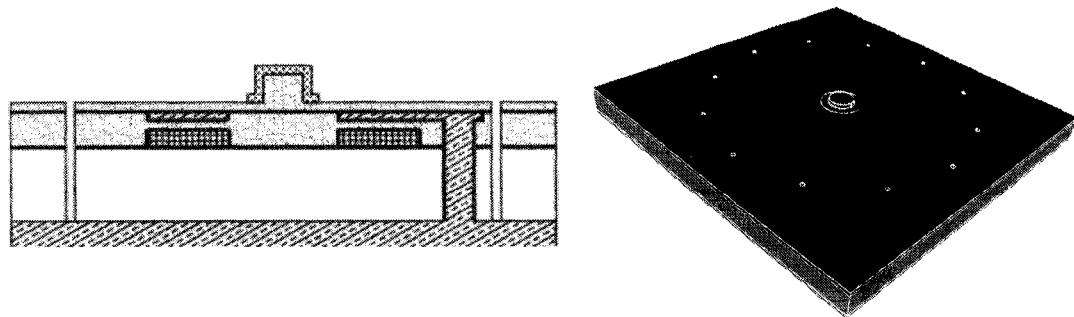


Figure 58. Stator fabrication step 14 – patterning of rotor-release trenches.

Labeled 3D models of the structure, resulting from IntelliSuite™ simulation of the developed process sequence are shown in figures 59 to 61. Figure 59 (cross-section 1) shows a cross-section view of the structure at process step 9 at a plane crossing through the middle of the copper vias (the oxide film has been omitted for better visualization).

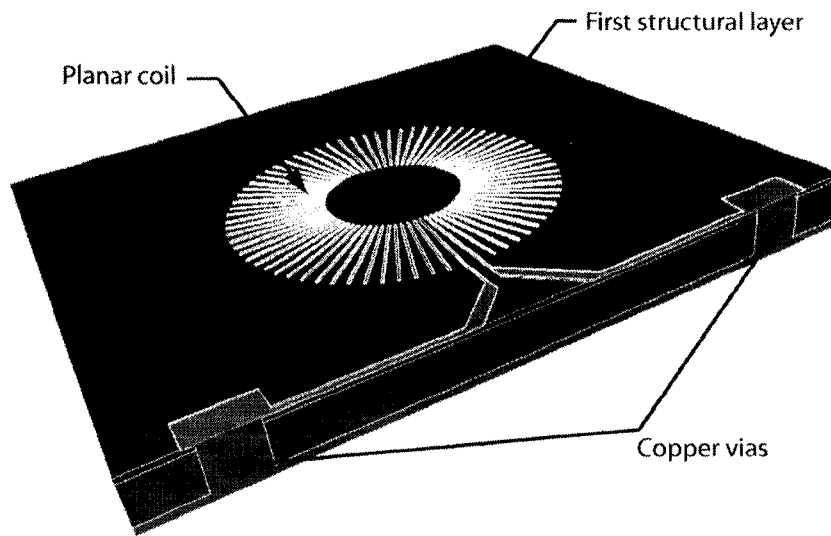


Figure 59. IntelliSuite™ simulation result of stator process sequence (cross section 1).

Figure 60 (cross-section 2) shows a cross-section view of the completed structure at a plane crossing through the center of the stator. Figure 61 shows a full view of the completed structure.

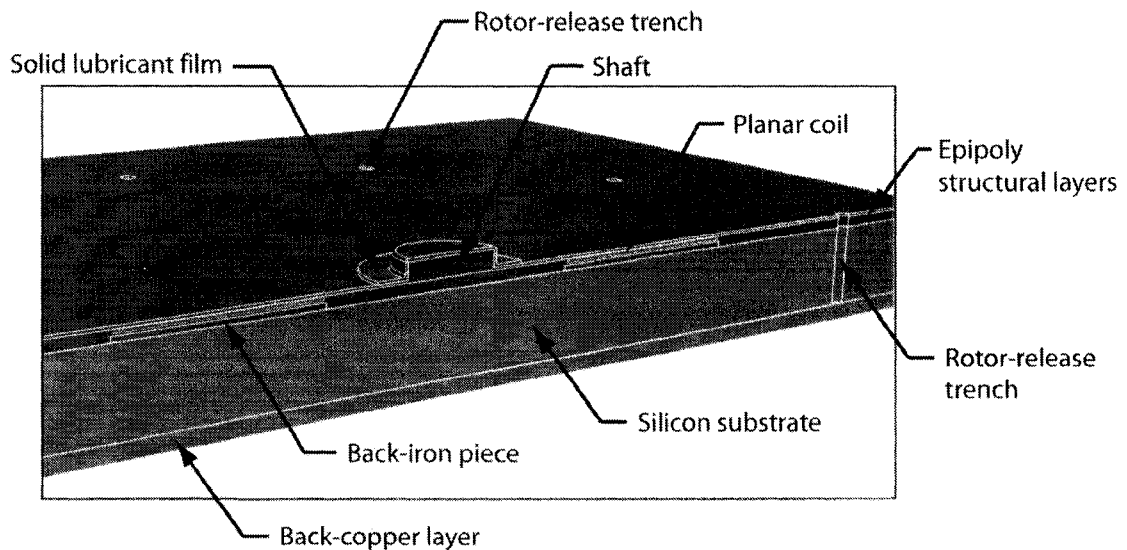


Figure 60. IntelliSuite™ simulation result of stator process sequence (cross section 2).

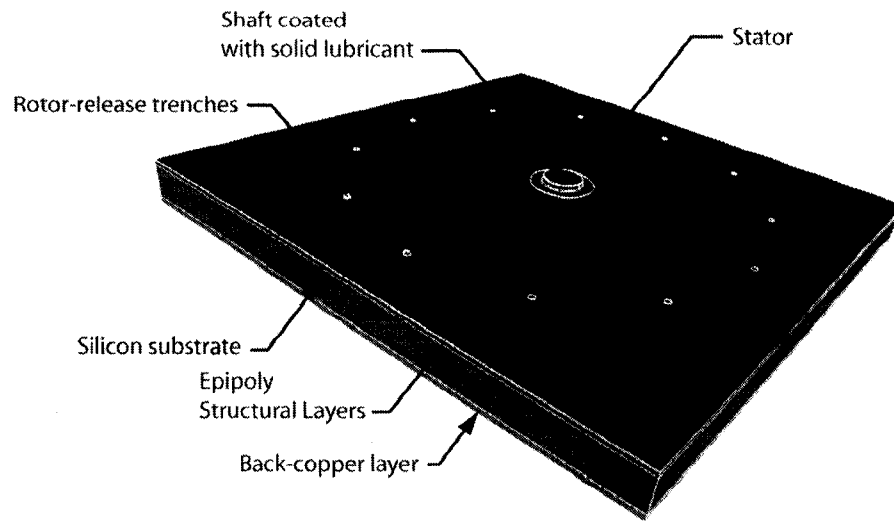


Figure 61. IntelliSuite™ simulation result of stator process sequence (full view).

4.4 Assembly / Encapsulation of the Microgenerator

The exposed epitaxial polysilicon surfaces of the rotor and stator are wet oxidized to prepare them for bonding [60–62]. This oxidation process will reduce further the diameter of the rotor-release trenches. After alternate polarity magnetization of the rotor, it is aligned between two identical stators, as shown in figure 62.

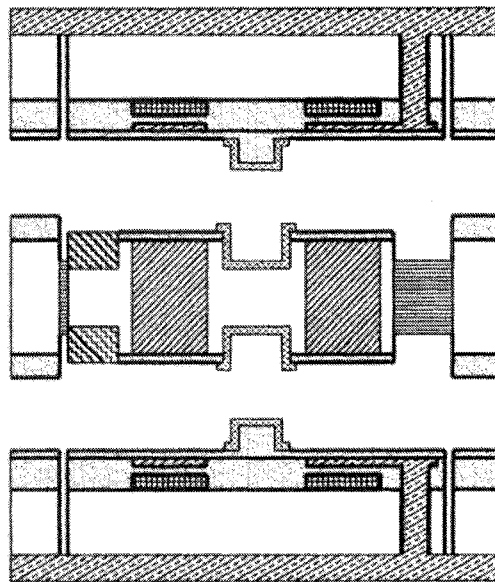


Figure 62. Assembly & Encapsulation step 1 – alignment of rotor and stators.

The three-wafer stack is assembled, hermetically bonded and annealed at 100° C in a single step using the direct oxide bonding (DOB) technique described in [60–62], as shown in figure 63, which is vacuum-encapsulation compatible and preserves the magnetization of the NdFeB pole pieces that have a Curie point of 150° C.

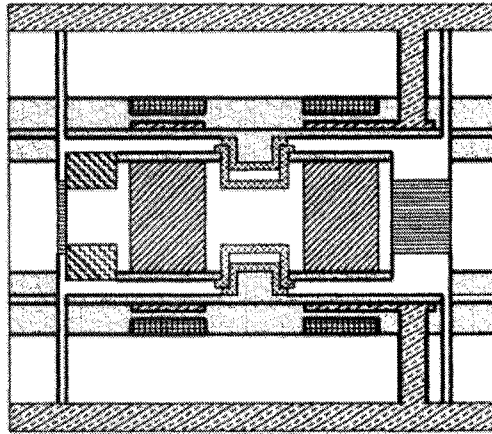


Figure 63. Assembly & Encapsulation step 2 – Assembly and bonding

The back-copper layers are patterned to form the contact pads. Then, the rotor is released enabling it to move freely around the shaft by injecting SU-8 solvent through the rotor-release trenches, as shown in figure 64.

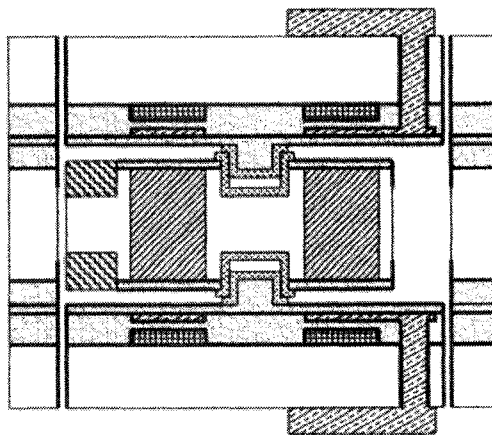


Figure 64. Assembly & Encapsulation step 3 – Solder pads patterning and rotor release.

Combining dry oxidation and LTO LPCVD deposition at temperatures below the Curie point of the micromagnets, a 3 to 5 μm thick film of silicon dioxide is deposited/grown on the top and bottom silicon surfaces and inside the rotor-release trenches, vacuum sealing the microgenerator. The oxide will not invade the interior of the microgenerator, as the rotor-release trenches will clog rapidly. A final mechanical polishing will expose the copper solder pads, as shown in figure 65.

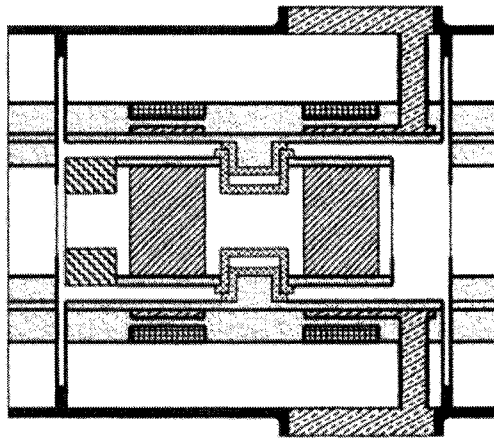


Figure 65. Assembly & encapsulation step 4 – vacuum sealing.

Before dicing the microgenerators, the solder pads can be coated with a plastic film or paint, which would protect them from oxidation until the moment of soldering/wire-bonding to the circuitry of the target biomedical device, when cleaning with acetone will be enough to expose the solder pads.

Chapter Summary

In this chapter the detailed fabrication process of a circular rotor microgenerator has been presented, dividing the sequence into 16 steps for the rotor fabrication, 14 steps for the stator fabrication and 4 steps for the assembly/encapsulation procedure. Conceptual cross-section diagrams of the structures at every process step have been used for the reader's better understanding of the fabrication and IntelliSuite™ generated 3D models resulting from simulation of the process table have been shown for every step of the rotor and stator fabrication and for the completed structures.

CHAPTER 5

Microgenerator Mounting and Actuation System

The first section of this chapter describes a mounting and actuation system that has been developed to provide biocompatible encapsulation for the microgenerator and integration with the standard modules of a cardiac pacemaker. The developed system also enables the microgenerator to be actuated by the pressure caused by the contraction of the thorax muscles during breathing in order to maintain energy generation even when the recipient is at rest or sleeping. Then, the human respiration mechanism is briefly introduced to explain which specific pressure in the thorax is capable of driving the microgenerator. Finally the forces that comprise the mechanical input to the microgenerator and the resulting behavior are described.

The built-in encapsulation of the microgenerator, formed by the stator bodies and the structure surrounding the rotor, allows its use as an off-the-shelf component simply to be soldered to the PCB of certain types of biomedical devices, such as cochlear implants or hearing aid instruments, in which the turning of the head may provide actuation for the microgenerator to produce enough power for the device, that would operate mostly during the day or whenever the recipient is awake. However, in critical applications, such as a cardiac pacemaker, continuous energy generation must be assured. For this purpose, a mounting and actuation system specially suited to enable the microgenerator to be used as a power source for cardiac pacemakers has been designed. In this system, the actuation of the microgenerator relies on the changes in thorax pressure during the inhalation and exhalation phases of breathing. The system consists of a silicone based biocompatible package designed to encapsulate and mount the microgenerator, and a breathing actuation

mechanism that drives the microgenerator from breathing to produce power even when the recipient is at rest or sleeping. The package also considers accommodation of the circuitry and sensors of the pacemaker and connection to the electrodes.

5.1 Silicone Encapsulation Package

In the system, a soft silicone rubber capsule filled with liquid silicone, as shown in figure 66, encapsulates the microgenerator and the designed breathing actuation mechanism, described later in this section. The silicone capsule and the microelectronic circuits of the pacemaker are to be surface mounted on a small PCB, as shown in figure 67.

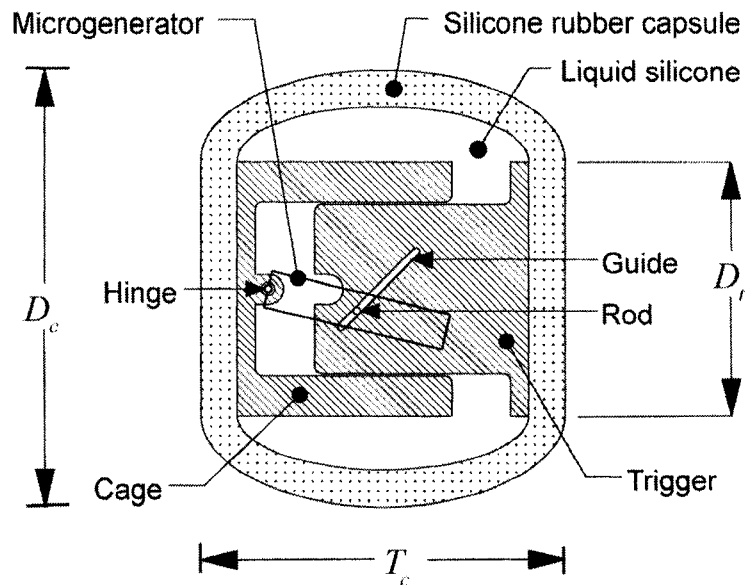


Figure 66. The microgenerator and actuation mechanism in a silicone rubber capsule.

A hard casing that holds the PCB and the whole system is then wrapped using another silicone capsule through which the pacemaker electrodes are interconnected with the PCB. A high permeability metallic layer should be embedded in the hard casing to provide electromagnetic shielding. Silicone has been chosen to be the structural material of the packaging system because it is used extensively in medical implants due to its low chemical reactivity. Liquid silicone, used in breast implants, has been selected to create the inner atmosphere of the capsule, as unlike gases, it cannot filtrate through the silicone

rubber. Additionally, it will act as a lubricating agent for the hinges and the rods in the guides used to mount the microgenerator in the breathing actuation mechanism.

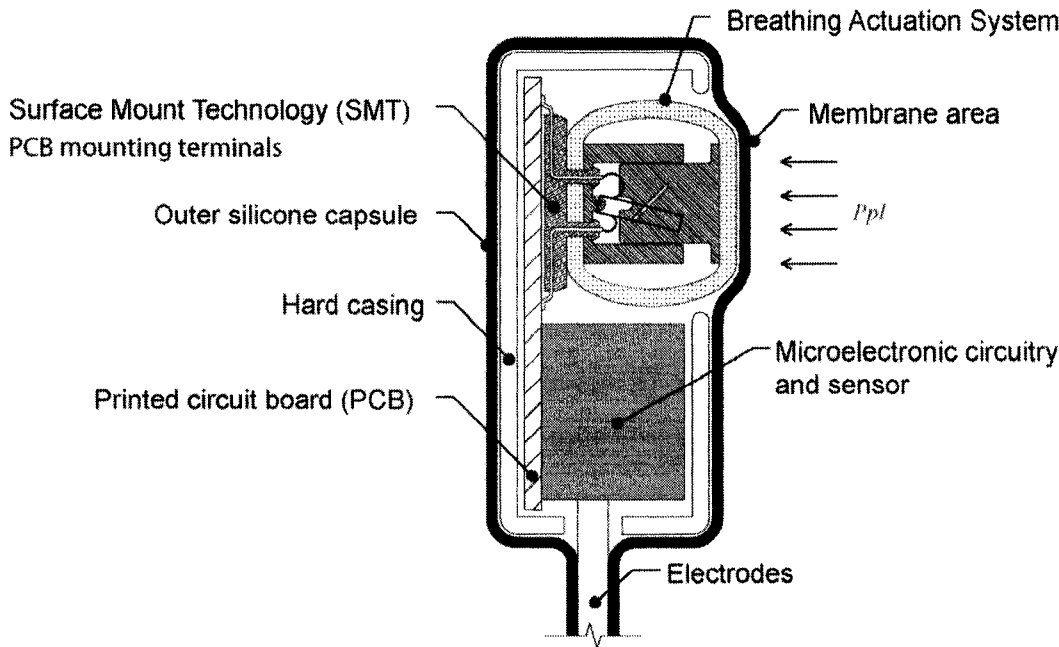


Figure 67. Silicone encapsulation of the complete pacemaker system.

First of all, the microgenerator is mounted in a housing with two lateral hinges and two driving rods attached at opposite sides, as shown in figure 68. Following figure 66 and 68, the hinges enable the microgenerator to be anchored to the baseplate of a cylindrical shaped cage through which a plunger-like solid silicone trigger piece moves like a piston due to a change in pleural pressure during breathing.

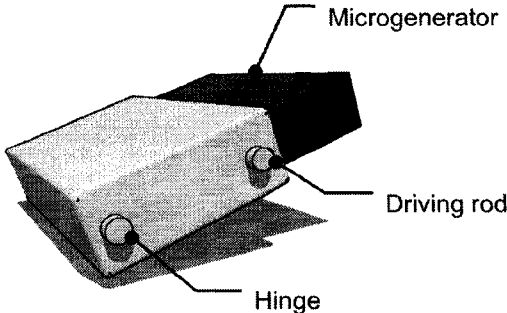


Figure 68. Attachment of the microgenerator to lateral hinges and driving rods.

The driving rods slide in slanted guides cut into the walls of the trigger piece. The shape of the cage and the trigger piece limit the angular displacement of the microgenerator to prevent breakage of the mechanism in case that too much force is exerted by the thorax muscles. This situation may occur, for example, when the recipient is under intense physical activity. The liquid silicone in the capsule is kept at an intermediate pressure within the range of the thorax pressure.

The capsule is to be mounted on the bone tissue of the sternum or the ribs or on any suitable support surface in such a way that the trigger piece remains oriented in the direction of the center of the thorax. At exhalation, when the lungs are deflated, the pressure inside the capsule generates a force proportional to the area A_t of the base of the trigger. This force is greater than the force exerted by the thorax on the trigger piece, thus, the trigger is pushed away from the fixed support as shown in figure 69a and the free end of the microgenerator moves downwards, as the driving rods attached to the microgenerator housing are pushed downwards due to the motion of the trigger piece.

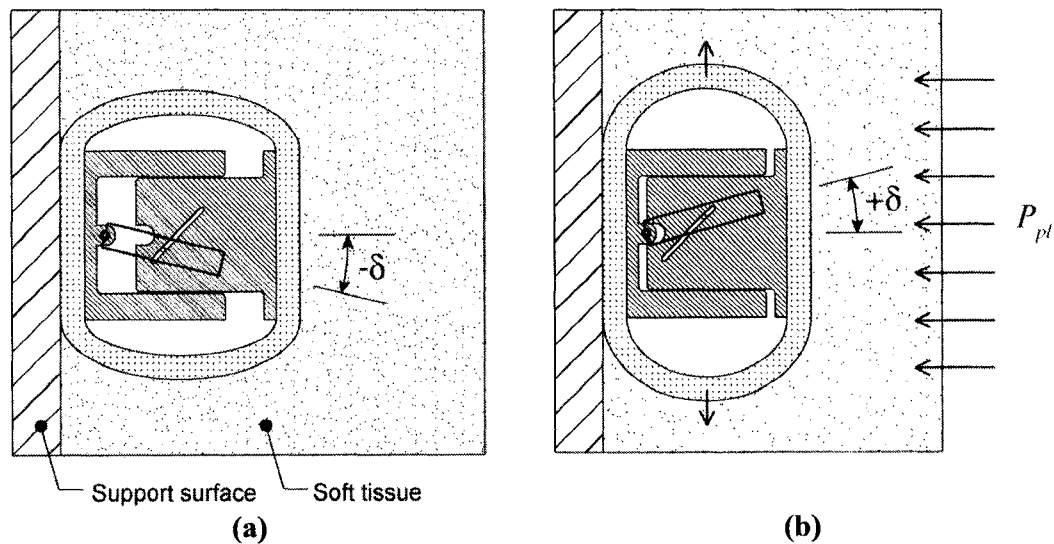


Figure 69. Operation of the breathing actuation mechanism.

(a) State of the system at exhalation, (b) State of the system at inhalation.

At inhalation, an increased thorax pressure compresses the soft tissue around the capsule against the support surface as shown in figure 69b. The force on the normal area A_t of the trigger piece coming from outside of the capsule becomes greater than the force exerted by the liquid silicone from inside of the capsule. As a result, the trigger moves towards

the fixed support, guiding the microgenerator upwards. In this way, with every inhalation and exhalation, the microgenerator will move up and down that will cause the rotor to oscillate, as described in section 5.3, to generate electrical power.

Assuming that the deformation of the silicone capsule is small and the liquid silicone is nearly incompressible, the volume inside the silicone capsule can be considered to remain constant throughout an inhalation-exhalation cycle. Thus the pressure exerted by the liquid silicone on the movable trigger can also be assumed to be constant.

Although the system for breathing actuation presented here produces oscillation of the rotor inside the microgenerator by the action of breathing, it still receives input from several organs in the body, as mentioned in section 1.2, such as the vibrations created by the heartbeat. The packaging of the microgenerator, as described here, is appropriate for the standing posture of the recipient. For other postures, the same packaging can be used just relocating the axis of the hinges and the orientation of the guides in the trigger. Therefore, for power generation at any physical posture of the recipient at least three generators, one for each spatial axis, should be present in the system as illustrated conceptually in figure 6. The liquid silicone in combination with the soft rubber silicone capsule will act as a spring system, but unlike conventional springs, silicone does not change its mechanical properties over time if not exposed to excessive heat, solvents or other chemicals that might modify its molecular structure. From this point of view the spring system can be regarded as a free-of-fatigue spring that may extend the life span of the system by eliminating fatigue failure associated to conventional springs.

5.2 Driving Pressure

The human ventilatory system includes the thoracic cavity and the abdominal cavity separated by the diaphragm [63] as shown in figure 70. Nearly one-third of the inner surface of the rib cage is composed of the area where the diaphragm is directly apposed to the rib cage. This is called the area of apposition, and the rest of the inner rib cage is apposed to the lung [64].

As the external intercostal muscles and the diaphragm contract, the lungs expand. The expansion of the lungs causes the pressure in the lungs to become slightly negative

relative to the atmospheric pressure. Consequently, the air moves from a region of higher pressure (the atmosphere) to a region of lower pressure (the lungs).

During expiration, the respiratory muscles relax and lung volume decreases. This causes pressure in the lungs to become slightly positive relative to the atmospheric pressure, which results in air leaving the lungs.

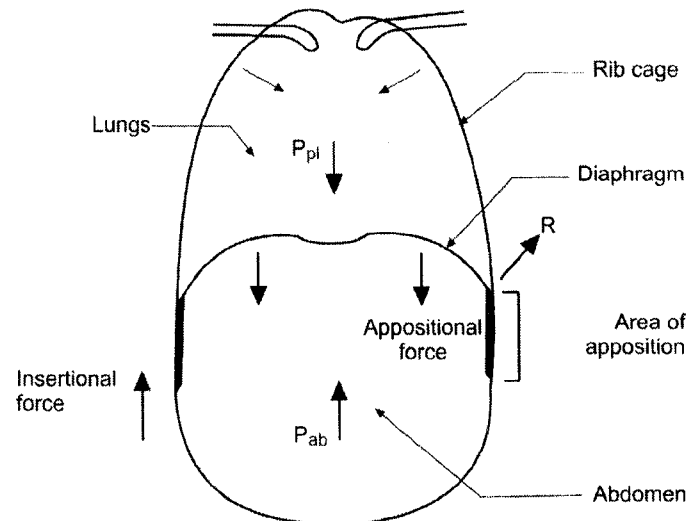


Figure 70. The human ventilatory system as shown in [55].

When the diaphragm contracts, it moves downwards like a piston, decreasing the pleural pressure in the area of lungs and increasing the abdominal pressure and the pleural pressure in the area of apposition, which is exerted outwards the inner surface of the lower rib cage [63].

The area of apposition is a good place for implantation of the microgenerator in the breathing actuation system explained in the previous section, since it is a wide area that allows many possible spots for implantation and because strong and well defined changes in pressure have been measured [64–65]. As determined in [63], the pleural pressure P_{pl} in the area of apposition raises from a baseline that equals the atmospheric pressure up to a maximum peak value of 490.32 to 980.67 Pa during inspiration and decreases back to the pressure baseline during expiration.

5.3 Mechanical Input to the Microgenerator

For the circular rotor geometry, the overall dimension of the microgenerator is $4 \times 4 \times 0.5$ mm³. This prompts the encapsulating soft rubber silicone capsule to have a diameter D_c of 10 mm and a thickness T_c of 8 mm to accommodate both the microgenerator and the breathing actuation mechanism. Assuming a circular surface of diameter 5.6 mm at the contact between the trigger and the inner wall of the capsule, the area of the capsule exposed to the normally incident pleural pressure in the apposition area A_t can be calculated as 24.63 mm². For any value of the pressure P_c of the liquid silicone inside the capsule within the range of change of pleural pressure (0 to 490.3 Pascal), for example 196.13 Pa, the internal force of the liquid silicone in the capsule F_c acting on the trigger can be calculated from $F_c = P_c \times A_t$, or 4.83 mN for the example. The external force F_t working on the area A_t in the opposite direction due to the pleural pressure can be calculated from $F_t = P_{pl} \times A_t$. This force F_t varies between 0 N to 12 mN, assuming 490.3 Pascal as the peak pleural pressure reached in the area of apposition [64]. Under these conditions the system will behave as shown in figure 71, in which the Ppl waveform is an approximation to the pleural pressure, waveform δ is the angle of the microgenerator respect to the z-axis and waveform Ω is the angular velocity of the rotor.

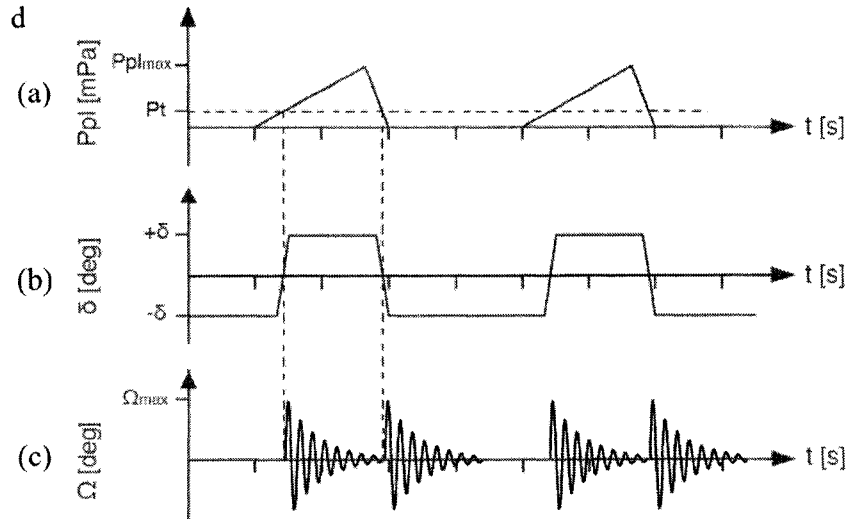


Figure 71. Waveforms of the mechanical input to the microgenerator.

(a) Approximation to the pleural pressure, (b) Angle of the microgenerator respect to the z-axis, (c) Angular velocity of the rotor.

While at rest, the thorax muscles exert nearly zero force over the trigger, so the internal force of the capsule keeps the trigger in the “out” position and the microgenerator is inclined at an angle $-\delta$ respect to the z-axis as shown in figure 70a. When inhaling the external force over the trigger raises and crosses the internal force threshold, causing the trigger to move to the “in” position and inclining the microgenerator to an angle $+\delta$ respect to the z-axis as shown in figure 70b. Assuming that the microgenerator was in stable state, it will start to oscillate at the change in inclination. Such an oscillation will be damped due to friction between the rotor and the shaft and due to the electromagnetic damping caused by the current induced in the planar coil.

In exhalation, the external force over the trigger will drop and will cross the threshold, so that the internal pressure of the capsule will take again the trigger to the “out” position and the microgenerator will be inclined back to the $-\delta$ angle. In this change of inclination the rotor will be taken to oscillation again. Thus, the microgenerator is actuated both, at the time of inhalation and at the time of exhalation. The average duration of a complete breath is 2 seconds. As the respiratory rate of a healthy adult human goes between 12 to 20 breaths per minute, the microgenerator will be actuated a minimum of 24 times per minute.

Chapter Summary

In this chapter a mounting and actuation system for the microgenerator was presented, providing details on the construction and materials for the package that contains and isolates the microgenerator from the live tissue, as well as the mechanism that enables the thorax muscles to actuate the microgenerator such that even when the recipient is at rest electricity for the pacemaker can still be generated. The way to integrate the encapsulation with the rest of the components of a pacemaker has also been clarified and the specific thorax pressure capable to drive the microgenerator has been exposed on the base of an explanation of the human respiration mechanism. The relevant forces that form the mechanical input to the microgenerator occurring in the system at inhalation and exhalation were described and numerical figures for them where derived from the physical dimensions of the package and the value of pleural pressure found in literature.

CONCLUSIONS

In this thesis, the design, fabrication and a scheme for mounting and actuation of a novel double stator axial flux bio-mechanically driven MEMS power generator for implantable medical devices, cardiac pacemakers in particular, has been presented. In the system, an asymmetrical pendulum-shaped rotor embedded with alternate polarity NdFeB thin film permanent magnets oscillates around a central shaft due to the overall movements of the human body and the local movement of the body organs to induce a voltage in planar coils embedded in a pair of stators. A semicircular rotor device of $1 \times 1 \text{ mm}^2$ footprint area of the rotor can generate $390 \mu\text{W}$ RMS power with an open circuit RMS voltage of 1.1 Volts per stator. Two of these microgenerators can be stacked to meet the power requirements of typical pacemakers. A circular rotor device with a $3 \times 3 \text{ mm}^2$ footprint area of the rotor can generate 59.7 mW RMS power with an open circuit RMS voltage of 9.0 Volts per stator. A mounting and actuation system has also been presented to physically mount the microgenerator along with the necessary microelectronic circuitry for the operation of the pacemaker. In its application to cardiac pacemakers, the designed mounting and actuation system enables the generator to produce power by means of the thorax pressure changes at inhalation and exhalation even when the recipient is at rest. Scaled or stacked versions of the microgenerator can be used to satisfy power requirements of other medical implants. The device can potentially provide a greater energy supply per unit volume compared to existing pacemaker batteries and can aid in developing smaller longer life pacemakers. Most importantly the microgenerator doesn't need injection of any sort of external gas or fuel for power generation. The maintenance free longer life of the microgenerator reduces the frequency of invasive surgery as necessary for implant replacement due to battery exhaust, particularly necessary for

existing pacemakers every 5 to 7 years. Additionally, a Magnetic Flux Shielding Selective Magnetization (MFSSM) method has been developed for alternate polarity magnetization of the deposited and patterned NdFeB thin film permanent magnets embedded in the rotor. A solid lubricant film composed of a blend of IF-WS₂ nanoparticles in a Ni-P alloy has been selected to minimize friction and wear in the shaft-rotor interfacing surfaces to ensure the long lifetime of the microgenerator.

Future Direction

The scalability and modularity of the developed MEMS power generator allow its optimization for target biomedical devices like blood pressure sensors, drug delivery systems and hearing aids. Without the need of an additional actuation mechanism, the motion of the forearms, wrists or feet, can drive the microgenerator in blood pressure sensors like those described in [69-71]. These monitoring systems, illustrated in figure 72, incorporate an instrumentation and diagnosis unit that interprets the electrical output of a MEMS pressure sensor, usually a silicon-based membrane with either, capacitive or piezoresistive sensing mechanism, and transmits the reading of pressure to a computer via a telemetry system. The received data is utilized to follow up a medical condition responsible of abnormal blood pressure and to prescribe a therapy accordingly.

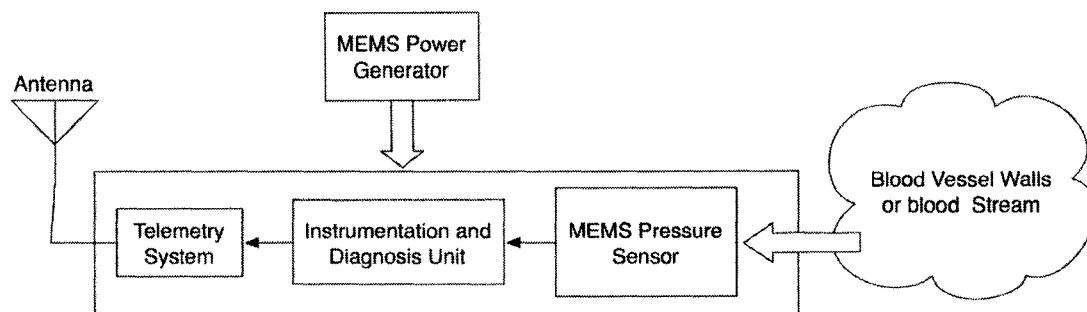


Figure 72. The MEMS power generator as a power supply of a blood pressure sensor.

Commercially available implantable pressure sensors, like that produced by [71], operate only when the physician interrogates the device by placing a nearby antenna that collects data and supplies power to the sensor. However, the autonomy that the developed MEMS

generator would give to these pressure sensors may allow their integration in a distributed wireless sensor network implanted throughout the human body. The sensors, placed in arms, legs and head, for example, would transmit their readings to a pacemaker for it to apply pulses with the most appropriate width and frequency to different areas of the myocardium in order to reach the optimum blood pressure at all measurement points, building this way a closed loop pacing system.

Due to the technical difficulties for the long-term supply of continuous electrical power to medical implants, most drug delivery systems nowadays are made passive, i.e. no microelectronics or electricity-consuming mechanical actuators are integrated to accurately regulate the drug flow. An example of a passive drug delivery system has been presented in [72] where a drug in a refillable reservoir is slowly released to the eye to treat conditions like diabetic retinopathy and glaucoma. The use of the developed microgenerator as a power supply may lead to advancements in active drug delivery systems like those in [73-74]. In these systems, depicted in figure 73, a logic/control and diagnosis unit determines the amount of drug to be delivered into the organism, as well as the delivery schedule to meet the prescribed therapy. Then, according to the diameter of the drug reservoir output pipe, the logic/control unit calculates the release time. Such a time is loaded into the timer/counter of a pulse generator that in turn activates either a microvalve that opens a pre-pressurized drug reservoir or a micropump that increases the pressure of the drug for it to be ejected out of the reservoir.

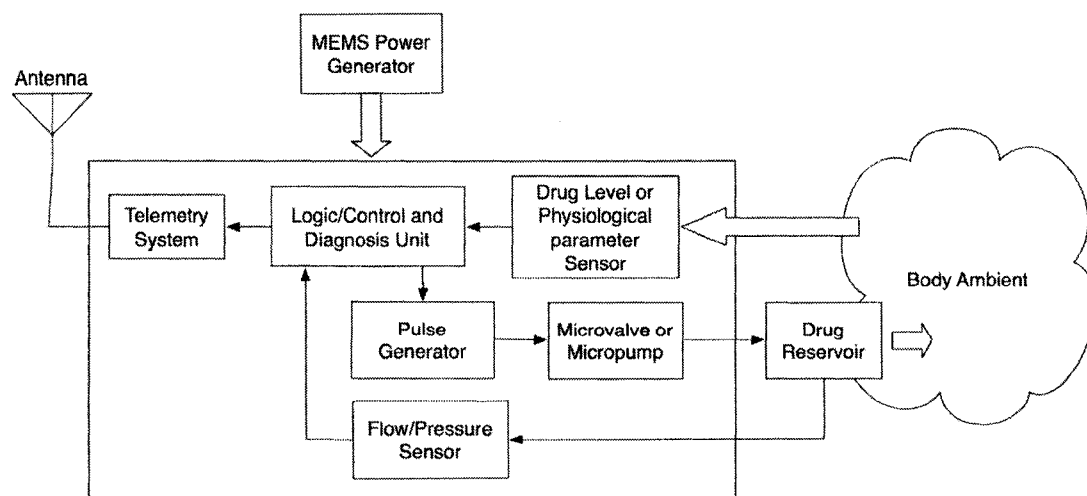


Figure 73. The MEMS power generator as a power supply of a drug delivery system.

A flow or pressure sensor may be also included in the system to assure that the amount of drug released from the drug reservoir matches the calculated value. For a closed loop control and depending on the nature of the physiological variable being controlled, a sensor module can be added to measure the concentration of medication or body chemicals like glucose or a physiological parameter like blood pressure.

The developed MEMS power generator may also open opportunities to realize devices like an active aqueous humor pressure controller for the treatment of glaucoma. In glaucoma disorders, the pressure of aqueous humor in the anterior chamber of the eye raises above normal levels, damaging permanently the nervous cells of the retina and causing blindness. In the proposed system, shown in figure 74, the developed MEMS power generator would provide electrical power driven by the rapid stochastic turning of the eye. A microvalve would be used to open the drainage of aqueous humor for it to be absorbed under a sac made of conjunctiva or to be injected directly into the blood stream. A MEMS pressure sensor would periodically acquire pressure measurements that the logic/control and diagnosis unit would employ to estimate the optimal aperture schedule of the microvalve in order to keep the pressure of aqueous humor within its safe range.

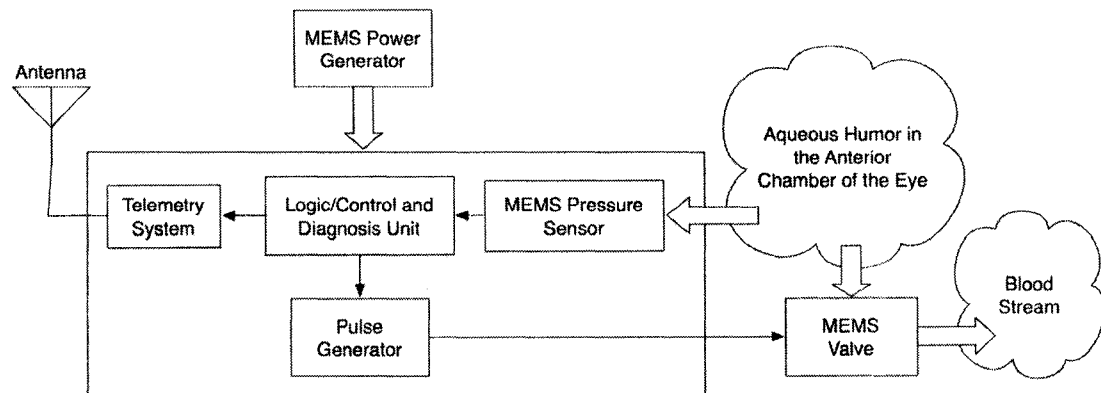


Figure 74. The MEMS power generator as a power supply of a pressure controller.

Employing the head turning as a source of driving motion, the developed MEMS power generator can also be integrated in hearing aid instruments or cochlear implants like those described in [75–76]. As shown in figure 75, these systems collect the mechanical vibrations within the audible range in the environment with a specialized acoustical sensor, like that described in [77]. The collected sound signal is filtered in a

microelectronic digital signal processor according to the particular needs of the recipient. The conditioned signal is amplified and sent to the auditory system by means of a set of electrodes or by an electromagnetic transducer that produces mechanical vibrations over the sensory cells/organs or the ear.

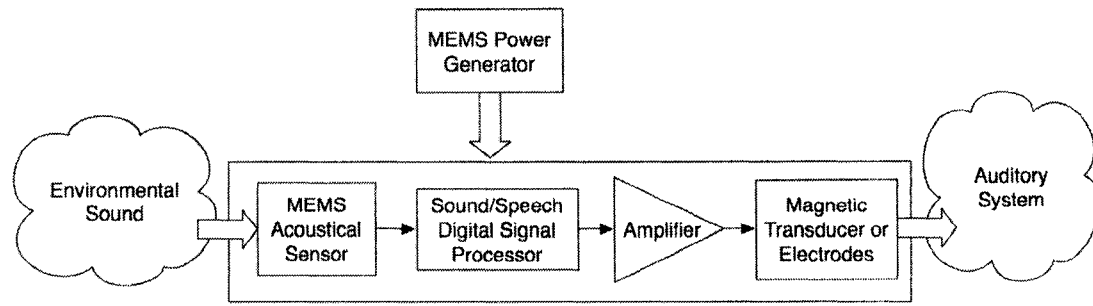


Figure 75. The MEMS power generator as a power supply of a hearing aid instrument.

To ensure power availability for the target device during periods of low or no muscular actuation over the microgenerator, a supercapacitor should be added to the system for energy storage. The top and bottom faces of the microgenerator are suitable to build MEMS based planar supercapacitors. The designed circular and semicircular rotor microgenerators allow 4 mm^2 and 16 mm^2 of capacitor plate area at each face, respectively. Supercapacitors made of activated carbon [78] have been in the market since long. Researchers now pursue the fabrication of MEMS supercapacitors [79–80] and supercapacitors based on carbon nanotubes [81–82] that are expected to surpass the energy density of electrochemical cell batteries. Whereas batteries rely on chemical reactions to produce ions that move from one electrode to the other, supercapacitors store energy in the form of an electric field and no chemical reaction occurs in them. For this reason, they deliver and store energy faster than batteries, as only the electrical resistance of conductors limits their charge/discharge currents. Supercapacitors have a consistent performance over time, can be safely left completely discharged for indefinitely long time, can operate in very low temperature environments and can withstand temperature changes, mechanical shocks and vibrations. Furthermore, supercapacitors can be recharged thousands of times and their chemical constituents are less toxic than those of batteries [82].

REFERENCES

- [1] S. A. P. Haddad, R. P. M. Houben, and W. A. Serdijn, "The Evolution of Pacemakers", *IEEE Engineering in Medicine and Biology Magazine*, Vol. 25, No. 3, pp. 38-48, May-June 2006.
- [2] M. Forde, P. Ridgely, "Implantable Cardiac Pacemakers", in *The Biomedical Engineering Handbook* Second Edition, Ed. Joseph D. Bronzino, Boca Raton: CRC Press LLC, 2000, Chapter 77, pp. 1-13.
- [3] J. R. Bernardy, Y. Comas, J. Esquilin and A. A. Hodge, "Biomechanics of a Pacemaker In the Human Body," *Proceedings of Applications of Engineering Mechanics in Medicine*, December 8, 2003, University of Puerto Rico, Mayagüez, December 2003, pp. E1-18.
- [4] V. S. Mallela, V. Ilankumaran, and N.S. Rao, "Trends in Cardiac Pacemaker Batteries", *Indian Pacing and Electrophysiology Journal*, vol. 4, no. 4, pp. 201-212, 2004.
- [5] J. Gagliardo; P. Hensel; K. Gleason, "A Review of Energy Conversion Technologies, and Trends in Development of Micro-Power Production Systems for Stand-alone Distributed Sensor Applications", *Proceedings of the International Green Energy Conference 2005*, 12-16 June 2005, Waterloo, Ontario, Canada, pp. 1-10.
- [6] J. B. Bates, G. R. Gruzalski, C. F. Luck, 1993. "Rechargeable Solid State Lithium Microbatteries". in *Proceedings of the IEEE Micro Electro Mechanical Systems (MEMS93)*, 1993, pp. 82-86.
- [7] J. Blanchard, D. Henderson, A. Lal, 2002. "A Nuclear Microbattery for MEMS Devices". *Technical Report, DE2002-799209*, Board of Regents of the University of Wisconsin System (US) 2002, pp. 1-10.
- [8] P. Perlo, G. Innocenti, G. Bollito, B. Pairetti, A. Zanella, C. Carvignese, "Microgenerator of Electrical Energy", *US Patent 6,932,030*, August 23, 2005.
- [9] A. S. Holmes, G. Hong, K. R. Pullen, "Axial-Flux Permanent Magnet Machines for Micropower Generation", *Journal of Microelectromechanical Systems*, Vol. 14, No. 1, pp. 54-62, February 2005.

- [10] S. Das, D. P. Arnold, I. Zana, J. W. Park, M. G. Allen, J. H. Lang, "Microfabricated High-Speed Axial-Flux Multiwatt Permanent-Magnet Generators—Part I: Modeling", *Journal of Microelectromechanical Systems*, Vol. 15, No. 5, pp. 1330-1350, October 2006.
- [11] S. Das, D. P. Arnold, J. W. Park, I. Zana, J. H. Lang, M. G. Allen, "Microfabricated High-Speed Axial-Flux Multiwatt Permanent-Magnet Generators—Part II: Design, Fabrication, and Testing", *Journal of Microelectromechanical Systems*, Vol. 15, No. 5, pp. 1351-1363, October 2006.
- [12] W. J. Li, T. C. H. Ho, G. M. H. Chan, P. H. W. Leong, H. Y. Wong, "Infrared Signal Transmission by a Laser-Micromachined Vibration-Induced Power Generator", *Proceedings of the 43rd IEEE Midwest Symposium on Circuits and Systems*, Vol. 1, pp. 236-239, August 8-11, 2000.
- [13] C. T. Pan, Y. M. Hwang, H. L. Hu, H. C. Liu, "Fabrication and Analysis of a Magnetic Self-Power Microgenerator", *Journal of Magnetism and Magnetic Materials*, Vol. 304, No. 1, pp. e394-e396, September 2006.
- [14] H. Kulah, K. Najafi, "An Electromagnetic Micro Power Generator for Low-frequency Environmental Vibrations", *17th IEEE International Conference on Micro Electro Mechanical Systems (MEMS)*, Maastricht, 2004. Vol. 1, pp. 237-240.
- [15] T. H. Ng, W. H. Liao, "Sensitivity Analysis and Energy Harvesting for a Self-Powered Piezoelectric Sensor", *Journal of Intelligent Material Systems and Structures*, Vol. 16, No. 10, pp. 785-797, October 2005.
- [16] S. P. Beeby, M. J. Tudor and N. M. White, "Energy Harvesting Vibration Sources for Microsystems Applications", *Measurement Science and Technology*, Vol. 17, pp. R175-R195, October 2006.
- [17] D. P. Arnold, "Review of Microscale Magnetic Power Generation", *IEEE Transactions on Magnetics*, Vol. 43, No. 11, pp. 3940-3951, November 2007.
- [18] K. Sasaki, Y. Osaki, J. Okazaki, H. Hosaka, K. Itao, "Vibration-Based Automatic Power-Generation System" *Microsystem Technologies*, Vol. 11, No. 8-10, pp. 965-969, August 2005.
- [19] Seiko AGS Quartz Watch product literature. Available online at URL: http://www.epson.co.jp/e/company/milestones/19_ag.pdf

- [20] Seiko Kinetic watch data sheet. Available from the Seiko Watch Corporation at URL: <http://www.seikowatches.com>
- [21] M. Kayakawa, "Electronic Wristwatch with Generator," *US Patent No. 5,001,685*, March 19, 1991.
- [22] J. A. Paradiso, T. Starner, "Energy Scavenging for Mobile and Wireless Electronics", *Pervasive Computing*, Vol. 4, No. 1, pp. 18–27, January-March 2005.
- [23] Kinetron MGS Watch data sheet. Available online at URL: <http://www.kinetron.nl>
- [24] D. Spreemann, Y. Manoli, B. Folkmer, D. Mintenback, "Non-Resonant Vibration Conversion", *Journal of Micromechanics and Microengineering*, Vol. 16, No. 9, pp. S169–S173, September 2006.
- [25] R. Tashiro, N. Kabei, K. Katayama, E. Tsuboi, K. Tsuchiya, "Development of an electrostatic generator for a cardiac pacemaker that harnesses the ventricular wall motion", *Journal of Artificial Organs*, Vol. 5, No. 4, December 2002.
- [26] S. G. MacDonald, "Biothermal Power Source for Implantable Devices", *US Patent No. 6,640,137*, October 28, 2003.
- [27] M. Weiner and S. Cooper, "Nanotechnology-Based Biothermal Materials for Implantable Devices and Other Applications," *Industrial Biotechnology*, Vol. 1, No. 3, pp. 194-195. September 2005.
- [28] M. Chiao, K. B. Lam and L. Lin, "Micromachined Microbial and Photosynthetic Fuel Cells", *Journal of Micromechanics and Microengineering*, Vol. 16, No. 12, pp. 2547-2553, December 2006.
- [29] M. Chiao, L. Lin, K.B. Lam, "Implantable, Miniaturized Microbial Fuel Cell", *US Patent No. 7,160,637*, January 2007. Available online at URL: <http://www.freepatentsonline.com/7160637.html>
- [30] The SweetPower™ company, URL: <http://www.sweetpower.com>
- [31] J. W. Judy, N. Myung, "Magnetic Materials for MEMS", *Proceedings of the MRS Workshop on MEMS Materials*, San Francisco, California, April 5-6, 2002, pp. 23-26.
- [32] T. Araki, and M. Okabe, "(Nd,Tb)-Fe-B Thin Film Magnets Prepared by Magnetron Sputtering", *Proceedings of the IEEE Ninth Annual International*

Workshop on Micro Electro Mechanical Systems (MEMS '96), 11-15 February 1996, pp. 244–249.

- [33] M. Nakano, S. Tutumi, H. Fukunaga, J. M. Song, “Preparation of Nd–Fe–B Thin Film Magnets with High Coercivity using Laser Ablation Technique”, *IEEE Transactions On Magnetics*, Vol. 37, No. 4, pp. 2573-2575, July 2001.
- [34] M. Nakano, R. Katoh, H. Fukunaga, S. Tutumi, F. Yamashita, “Fabrication of Nd–Fe–B Thick-Film Magnets by High-Speed PLD Method”, *IEEE Transactions on Magnetics*, Vol. 39, No. 5, pp. 2863-2865, September 2003.
- [35] H. Lemke, T. Lang, T. Goddenhenrich, C. Heiden , “Micro Patterning of Thin Nd-Fe-B Films”, *Journal of Magnetism and Magnetic Materials*, Vol. 148, No. 3, pp. 426-432, July 1995.
- [36] I. Zana and G. Zangari, “CoPt Micromagnets by Electrodeposition”, *Presentation 2001 MINT Fall Review*, November 7, 2001, pp. 1-17.
- [37] S. Jhy-Chau, H. Hsin-Hsin, T. Jai-Lin, C. Tsung-Shune, “Low-Temperature In-Situ Growth of High-Coercivity Fe-Pt Films”, *IEEE Transactions on Magnetics*, Vol. 37, No. 4, Part 1, pp. 1280 – 1282, July 2001.
- [38] T. Budde, H. H. Gatzel, “Magnetic Properties of Thick Sputter Deposited SmCo Films for MEMS Applications”, *Digest of Technical Papers of 2002 IEEE International Magnetics Conference. INTERMAG Europe 2002*. 28 April - 2 May 2002, pp. GD05.
- [39] M. Nakano, R. Katoh, H. Fukunaga, S. Tutumi, F. Yamashita, “Fabrication of Nd-Fe-B Thick-Film Magnets by High-Speed PLD Method”, *IEEE Transactions on Magnetics*, Vol. 39, No. 5, Part 2, pp. 2863 – 2865. September 2003.
- [40] J. Topfer, V. Christoph, "Multi-Pole Magnetization of NdFeB Sintered Magnets and Thick Films for Magnetic Micro-actuators", *Sensors and Actuators A*, Vol. 113, pp. 257–263, July 2004.
- [41] J. Topfer; B. Pawlowski; H. Beer, K. Plötner, P. Hofmann, and J. Herrfurth, "Multi-pole Magnetization of NdFeB Magnets for Magnetic Micro-Actuators and its Characterization with a Magnetic Field Mapping Device", *Journal of Magnetism and Magnetic Materials*, Vol. 270, No.1-2, pp. 124-129, March 2004.

- [42] B. Pawlowski, J. Topfer, "Permanent Magnetic NdFeB Thick Films", *Journal of Materials Science*, Vol. 39, No. 4, pp. 1321-1324, February 2004.
- [43] E. P. Furlani, S. K. Ghosh, W. J. Grande, "Apparatus for the Formation and Polarization of Micromagnets", *US Patent No. 179,767*, March 7, 2000.
- [44] K. Strawhecker, D. B. Asay, J. McKinney, S. H. Kim, "Reduction of Adhesion and Friction of Silicon Oxide Surface in the Presence of N-Propanol Vapor in the Gas Phase", *Tribology Letters*, Vol. 19, No. 1, pp. 17-21, May 2005.
- [45] I. Etsion, "Improving Tribological Performance of Mechanical Components by Laser Surface Texturing", *Tribology Letters*, Vol. 17, No 4, pp. 733-737, November 2004.
- [46] G. Sheng, B. Liu, W. Hua, Y. Miao, B. Xu, L. Yan, U. Sridhar, "Design and Analysis of MEMS-Based Slider Suspensions for a High-Performance Magnetic Recording System", *Journal of Micromechanics and Microengineering*, Vol. 10, pp. 64-71, March 2000.
- [47] B. Bhushan, "*Springer Handbook of Nanotechnology*", 2004 Springer-Verlag, Chapter 22, pp. 631- 660, ISBN 354029855X.
- [48] W. X. Chen, J. P. Tu, Z. D. Xu, R. Tenne, R. Rosenstveig, W. L. Chen, H.i Y. Gan, "Wear and Friction of Ni-P Electroless Composite Coating Including Inorganic Fullerene WS₂ Nanoparticles", *Advanced Engineering Materials*, Vol. 4, No. 9, pp. 686-690, September 2002.
- [49] L. Rapoport, N. Fleischer, R. Tenne, "Applications of WS₂ (MoS₂) inorganic Nanotubes and Fullerene-Like Nanoparticles for Solid Lubrication and for Structural Nanocomposites", *Journal of Materials Chemistry*, Vol. 15, No. 18, pp. 1782-1788, 2005.
- [50] A. Castro-Neto, F. Guinea, N. Miguel-Peres, "Drawing Conclusions from Graphene", *Physics World*, pp. 1-5, November 2006.
- [51] M. Dienwiebel, G. S. Verhoeven, N. Pradeep, Joost W. M. Frenken†, J. A. Heimberg, H. W. Zandbergen, "Superlubricity of Graphite", *Physical Review Letters*, Vol. 92, No.12, pp. 126101-1 to 126101- 4, March 2004.
- [52] V. Leshchynsky Ph.D. Materials Science, NSERC Industrial Research Chair, Research Associate at the University of Windsor, Department of Physics. URL:

www.uwindsor.ca/ciramc , E-mail: leshynsk@uwindsor.ca, Phone: (519) 253-3000
ext 2672, fax: (519) 971-3611.

- [53] A. Partridge, A. E. Rice, T. W. Kenny, "New Thin Film Epitaxial Polysilicon Encapsulation For Piezoresistive Accelerometers", *Proceedings of The 14th IEEE International Conference on Micro Electro Mechanical Systems, 2001. MEMS 2001.*, 21-25 January 2001, Vol. 1, pp. 54-59.
- [54] N.V. Myung, D. Y. Park, B. Y. Yoo, P. T. A. Sumodjo, "Development of Electroplated Magnetic Materials for MEMS", *Journal of Magnetism and Magnetic Materials*, Vol. 265, No. 2, pp. 189–198, September 2003.
- [55] P. C. Andricacos, C. Uzoh, J. O. Dukovic, J. Horkans, H. Deligianni, "Damascene Copper Electroplating for Chip Interconnections", *IBM Journal of Research and Development*, Vol. 42, No. 5, pp. 567-574. September 1998.
- [56] D. C. Edelstein, G. A. Sai-Halasz, Y.-J. Mii, "VLSI On-Chip Interconnection Performance Simulations and Measurements," *IBM Journal of Research and Development*. Vol. 39, No. 4, pp. 383-401, July 1995.
- [57] D. C. Edelstein, "Advantages of Copper Interconnects," *Proceedings of the 12th International IEEE VLSI Multilevel Interconnection Conference*, 1995, pp. 301-307.
- [58] M. M. Chow, J. E. Cronin, W. L. Guthrie, W. Kaanta, B. Luther, W. J. Patrick, K. A. Perry, C. L. Standley, "Method for Producing Coplanar Multi-Level Metal/Insulator Films on a Substrate and for Forming Patterned Conductive Lines Simultaneously with Stud Vias," *US Patent 4,789,648*, December 6, 1988.
- [59] J. O. Dukovic, "Feature-Scale Simulation of Resist-Patterned Electrodeposition," *IBM Journal of Research and Development*, Vol. 37, No. 2, pp. 125-141, March 1993.
- [60] Q. Y. Tong, Q. Gan, G. Fountain, G. Hudson and P. Enquist, "Low-Temperature Bonding of Silicon-Oxide-Covered Wafers Using Diluted HF Etching", *Applied Physics Letters*, Vol. 85, No. 14, pp. 2762-2764, October 2004.
- [61] Q. Y. Tong, Q. Gan, G. Fountain, P. Enquist, R. Scholz, U. Gösele, "Fluorine-Enhanced Low-Temperature Wafer Bonding of Native-Oxide Covered Si Wafers", *Applied Physics Letters*, Vol. 85, No. 17, pp. 3731-3733. October 2004.

- [62] H. Takagi, R. Maeda, T.R. Chung, T. Suga, "Low Temperature Direct Bonding of Silicon and Silicon Dioxide by the Surface Activation Method", *Proceedings of Transducers '97, IEEE 1997 International Conference on Solid-State Sensors and Actuators*, June 16-19, 1997. pp. 657-660.
- [63] N. G. Koulouris, I. Dimitroulis, "Structure and Function of the Respiratory Muscles", *PNEUMON*, No. 2, Vol. 14, pp. 91-108, May-August 2001.
- [64] P. T. Macklem, "The Act of Breathing", *News in Physiological Sciences*, Vol. 5, No. 6, pp. 233-237, December 1990.
- [65] P. T. Macklem, L. Zocchi, E. Agostoni, "Pleural Pressure Between Diaphragm and Rib Cage During Inspiratory Muscle Activity", *Journal of Applied Physiology*, Vol. 65, no. 3, pp. 1286-1295, September 1988.
- [66] M. Ward, P. T. Macklem, "The Act of Breathing and How It Fails", *Chest*, Vol. 97, No. 3, pp. 36-39, March 1990.
- [67] H. Rahn, A. B. Otis, L. E. Chadwick, W. O. Fenn, "The Pressure-Volume Diagram of the Thorax and Lung", *The American Journal Of Physiology*, Vol. 146, No. 6, pp. 161-178, May 1946.
- [68] C. M. Kenyon, S. J. Cala, S. Yan, A. Aliverti, G. Scano, R. Duranti, A. Pedotti, P. T. Macklem, "Rib Cage Mechanics During Quiet Breathing and Exercise in Humans", *Journal of Applied Physiology*, Vol. 83, No. 4, pp. 1242-1255. October 1997.
- [69] P. Cong, D. J. Young, W. H. Ko, "Novel long-term implantable blood pressure monitoring system", *Proceedings of 2004 IEEE Sensors*, 24-27 October 2004, Vol. 3, pp. 1359 - 1362.
- [70] P. Cong, D.J. Young, B. Hoit, W. H. Ko, "Novel Long-Term Implantable Blood Pressure Monitoring System with Reduced Baseline Drift", *Proceedings of the 28th Annual Conference of the IEEE Engineering in Medicine and Biology Society, 2006. EMBS '06*, August 2006, pp. 1854-1857.
- [71] EndoSure® Wireless AAA Pressure Measurement System by CardioMEMS Inc. product literature available online at URL: <http://www.cardiomems.com>
- [72] R. Lo, K. Kuwahara, P. Y. Li, R. Agrawal, M.S. Humayun, E. Meng, "A Passive Refillable Intraocular MEMS Drug Delivery Device", *Proceedings of 2006*

International Conference on Microtechnologies in Medicine and Biology, Okinawa, Japan 9-12 May 2006, pp. 74-77.

- [73] A. C. Richards Grayson, R. Scheidt Shawgo, Y. Li, M.J. Cima, "Electronic MEMS for triggered delivery", *Advanced Drug Delivery Reviews*, Vol. 56, No. 2, pp. 173-184, February 2004.
- [74] A. T. Evans, J. M. Park, G. F. Nellis, S. A. Klein, J. R. Feller, L. Salerno, Y. B. Gianchandani, "A Low Power, Microvalve-Regulated Drug Delivery System Using a SI Micro-Spring Pressurized Balloon Reservoir", *Proceedings of the 2007 Solid-State Sensors, Actuators and Microsystems Conference. TRANSDUCERS 2007*, Lyon, France, 10-14 June 2007, pp. 359-362.
- [75] S.U. Ay, Z. Fan-Gang, B.J. Sheu, "Hearing with bionic ears [cochlear implant devices]", *IEEE Circuits and Devices Magazine*, Vol. 13, No. 3, pp. 18 - 23, May 1997.
- [76] K.D. Wise, K. Najafi, "Fully-Implantable Auditory Prostheses: Restoring Hearing to the Profoundly Deaf", *2002 Electron Devices Meeting Digest. IEDM '02*, 8-11 December 2002, pp. 499 - 502.
- [77] S. Chowdhury, M. Ahmadi, W.C. Miller, "The Concept of a 3-D Cubic Acoustical Sensor Microarray Cluster for Use in a Hearing Instrument", *Proceedings of the 2004 International Conference on MEMS, NANO and Smart Systems. ICMENS 2004*, 25-27 August 2004, pp. 160-164.
- [78] T. Aida, I. Murayama, K. Yamada, M. Morita, "High-energy-density hybrid electrochemical capacitor using graphitizable carbon activated with KOH for positive electrode", *Journal of Power Sources*, Vol. 166, No. 2, pp. 462-470, April 2007.
- [79] D. H. Lewis, J. J. Waypa, E. K. Antonsson, C. D. E. Lakeman, "Micro-supercapacitor", *US Patent No. 6,621,687*, September 2003.
- [80] J.H. Sunga, S.J. Kima, S.H. Jeongb, E.H. Kima, K. H. Leea, "Flexible micro-supercapacitors", *Journal of Power Sources*, Vol. 162, No. 2, pp. 1467-1470, November 2006.

- [81] J. E. Jang, S. N. Cha, Y. Choi, G. A. J. Amaratunga, D. J. Kang, D. G. Hasko, "Nanoscale Capacitors Based on Metal-Insulator-Carbon Nanotube-Metal Structures", *Applied Physics Letters*, December 2005.
- [82] J. Schindall, "The Charge of the Ultracapacitors", *IEEE Spectrum*, Vol. 44, No. 11, pp. 42-46, November 2007.

VITA AUCTORIS

Jose Martinez-Quijada was born in 1971 in Toluca, Estado de Mexico, MEXICO. He obtained the Licentiate's degree in Electronics and Communications Engineering from Universidad Iberoamericana Plantel Santa Fe in Mexico City, where he graduated in 1995 and defended his thesis in 1998. He is currently a candidate for the degree of Master of Applied Science in Electrical and Computer Engineering in the field of Microelectromechanical Systems (MEMS) at the University of Windsor, Windsor, Ontario, CANADA.